Modeling the carbon dioxide electrocatalysis system

Bohra, D.

DOI
10.4233/uuid:000612a5-fbda-4394-b36f-45bf44ef9e21

Publication date
2020

Document Version
Final published version

Citation (APA)
Bohra, D. (2020). *Modeling the carbon dioxide electrocatalysis system*. [Dissertation (TU Delft), Delft University of Technology]. https://doi.org/10.4233/uuid:000612a5-fbda-4394-b36f-45bf44ef9e21

Modeling the Carbon Dioxide Electrocatalysis System

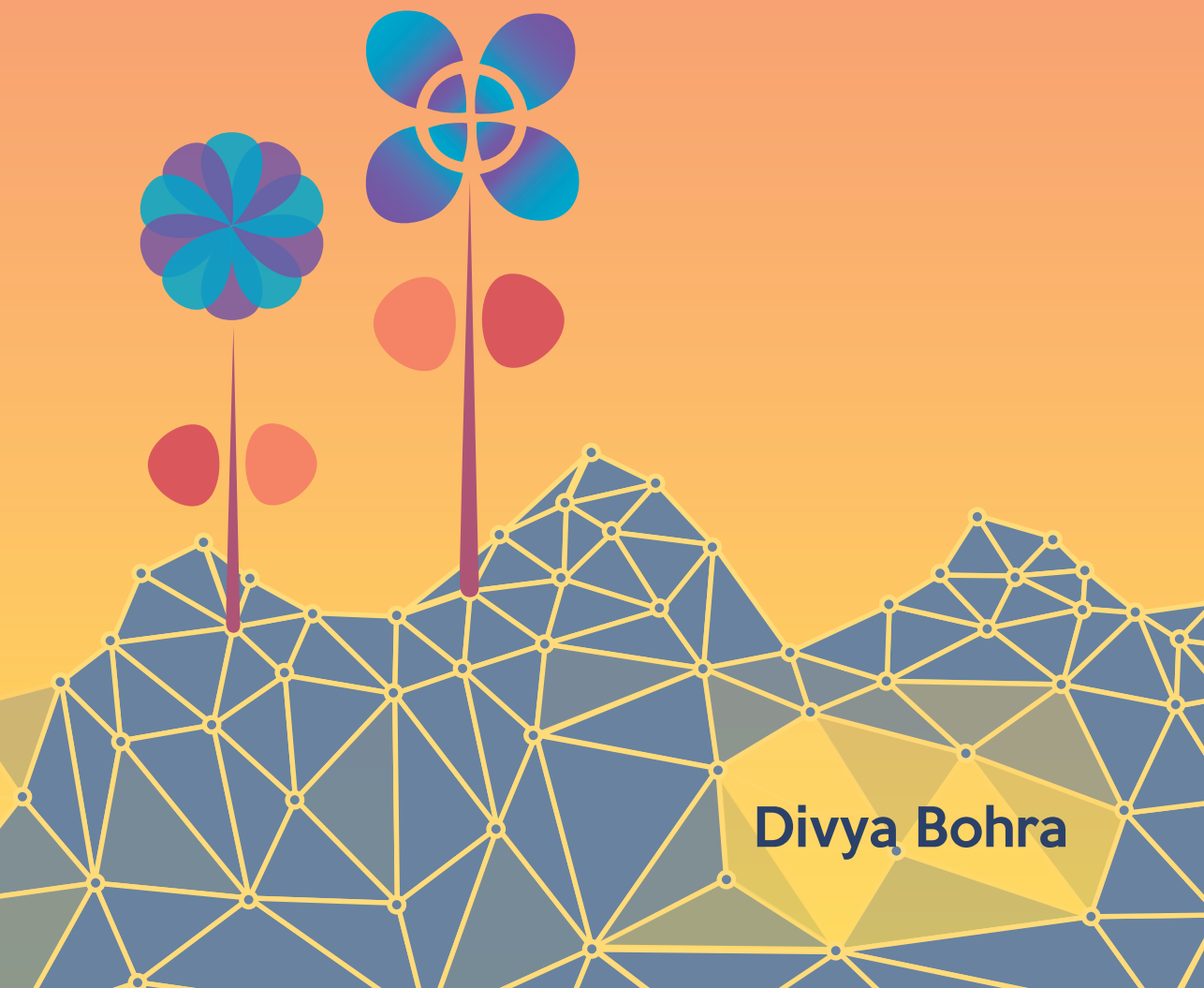

Divya Bohra

Modeling the Carbon Dioxide Electrocatalysis System

Divya Bohra

Modeling the Carbon Dioxide Electrocatalysis System

Dissertation

for the purpose of obtaining the degree of doctor
at Delft University of Technology,
by the authority of the Rector Magnificus
prof. dr. ir. T.H.J.J. van der Hagen,
chair of the Board of Doctorates,
to be defended publicly on
Monday 18, January 2021 at 15:00 o'clock

by

Divya BOHRA

Master of Science in Chemical Engineering,
Delft University of Technology, The Netherlands,
born in Ratlam, India.

This dissertation has been approved by

promotor: Dr. W. A. Smith
promotor: Prof. dr. E. A. Pidko

Composition of the doctoral committee:

Rector Magnificus	chairperson
Dr. W. A. Smith	Delft University of Technology, promotor
Prof. dr. E. A. Pidko	Delft University of Technology, promotor
Independent members:	
Prof. dr. ir. P. M. Herder	Delft University of Technology
Dr. S. Haussener	École Polytechnique Fédérale de Lausanne, Switzerland
Dr. K. Chan	Technical University of Denmark
Dr. M. C. Figueiredo	Eindhoven University of Technology
Prof. dr. A. Urakawa	Delft University of Technology, reserve member

The work described in this thesis has been carried out in the Materials for Energy Conversion and Storage (MECS) group, Department of Chemical Engineering, Faculty of Applied Sciences, Delft University of Technology. It was supported by the Netherlands Organisation for Scientific Research (NWO) through the VIDI grant (Dr. W. A. Smith). This work was carried out on the Dutch national e-infrastructure with the support of SURF Cooperative.

Printed by: Ipskamp Printing B.V.

Cover artwork: Divya Bohra

ISBN 978-94-6421-162-7

An electronic version of this dissertation is available at
http://repository.tudelft.nl/.

Contents

Summary

Increasing level of atmospheric carbon dioxide (CO_2) because of human activities is a serious threat to ecosystems on Earth due to global warming. A transition to net-zero CO_2 emissions before 2050 is necessary to limit the global mean surface temperature rise to 1.5°C-2°C above pre-industrial levels. Carbon capture and utilization technologies are an important piece of the decarbonisation puzzle. Electrochemical conversion of CO_2 (eCO_2R) using renewable electricity can contribute to an integrated low-carbon energy and materials system by providing grid flexibility and means to produce essential hydrocarbon molecules. Considerable progress has been made in the past decade in developing eCO_2R systems towards practical feasibility. However, major challenges remain to realize efficient and cost-competitive eCO_2R devices at industrial scale.

Computational simulations have played an important role in building the understanding of CO_2 electrocatalysis processes. Simulating eCO_2R is a multi-scale challenge due to several coupled physical phenomena operating over vastly different length and time scales. In this thesis, we use computational techniques at multiple scales to understand the mechanistic and environmental driving forces for performance. We focus on systems with carbon monoxide (CO) producing transition metal catalysts and aqueous electrolytes due to their practical significance. Several aspects of our conclusions, however, are broadly applicable to other eCO_2R systems.

Silver (Ag) electrocatalysts show promising performance for CO production with high selectivity. However, thermodynamic predictions using *ab-initio* density functional theory (DFT) calculations predict formate ($HCOO^-$) to be the more energetically favorable reaction pathway on Ag. We address this apparent discrepancy between theoretical and experimental findings using DFT simulations and *in-situ* surface-enhanced Raman spectroscopy (SERS) experiments. We find that surface adsorbed hydrogen ($*H$) plays a decisive role in determining selectivity amongst reaction pathways during eCO_2R. Factors such as solvation, water-shuttling of pro-

tons and lateral adsorbate interactions, together help explain how the CO, $HCOO^-$ and H_2 reaction pathways interact in complex ways on the Ag surface resulting in high selectivity for CO.

It is evident through our DFT studies on Ag, as well as experimental results in literature, that the performance of eCO_2R depends on the properties of the reaction interface rather than simply the catalyst surface. The reaction interface is composed of a charged catalyst surface at a constant potential facing an aqueous electrolyte. In order to understand the reaction environment for the eCO_2R catalytic processes, we use a continuum approach to model the transport processes in the electrolyte facing the catalyst surface. We use the generalized modified Poisson-Nernst-Planck (GMPNP) model to solve for the electrostatic migration, diffusion and buffer reaction kinetics self-consistently with appropriate boundary conditions while accounting for volume exclusion due to size of solution species. The results from the GMPNP model demonstrate how steric effects and electrostatic migration play a crucial role in determining the CO_2 concentration and pH close to the catalyst surface. Our approach establishes the significance of accounting for the electrical double layer (EDL) for accurately studying eCO_2R.

CO_2 conversion rates > 200 mA/cm^2 are required for the eCO_2R technology to become practically feasible. We therefore move our attention to gas diffusion electrode (GDE)-based flow-cell setups that can achieve significantly higher current density due to better mass transport. We extend the GMPNP model to study the reaction conditions within an effective three-dimensional catalyst pore in a flow-cell as a function of the catalyst structure properties and operating conditions. Our analysis finds the catalyst layer depth and the boundary conditions at the gas-electrolyte and electrolyte-electrolyte interfaces highly influential for pH and ion concentrations within the catalyst pore. We highlight the importance of mass transport in GDE-based eCO_2R setups as an important means to control catalyst performance.

In this thesis, we simulate different aspects of the eCO_2R system, ranging from reaction pathways at the atomic level, to reaction conditions at the practical device level. We show that the selectivity of the electrocatalysis processes can be influenced significantly by phenomena at the catalyst surface, the EDL and within the catalyst layer as a whole. A

hierarchical approach to system design accounting for the influential parameters at each scale can therefore be fruitful to achieve optimal performance. The complex multiscale nature of the eCO_2R process necessitates the development of simulation frameworks that integrate the phenomena at different scales for predictability over experimental observations. Additionally, benchmarking and systematic data collection of both, simulation results and experimental observations, will greatly help the convergence towards rationally-designed high-performing eCO_2R systems. Electrochemical conversion of CO_2 to low-carbon hydrocarbons at the industrial level can be a potential game-changer on the path to climate change mitigation. There is some distance to go and computational simulations will remain a valuable enabler on this journey.

Samenvatting

Het stijgende niveau van atmosferische koolstof dioxide (CO_2) door menselijke activiteiten is een serieuze bedreiging voor de ecosystemen op Aarde door de klimaatopwarming. Een transitie naar netto nul CO_2 uitstoot voor 2050 is nodig om het wereldwijde gemiddelde oppervlakte temperatuurstijging te beperken tot 1.5°C-2°C boven pre-industriële niveaus. Koolstof opslag en gebruik technologieën zijn een belangrijk deel van de decarbonisatie puzzel. Electrochemische conversie van CO_2 (eCO_2R) gebruik makend van hernieuwbare elektriciteit kan bijdragen tot een geïntegreerde lage koolstof energie en materialen systeem door het voorzien van net flexibiliteit en manieren om essentiële koolwaterstof moleculen te produceren. Opmerkelijke vooruitgang is geboekt in het voorbije decennium in het ontwikkelen van praktisch haalbare eCO_2R systemen. Desondanks, het blijft een grote uitdaging om efficiënte en kost-competitieve eCO_2R toestellen te maken op industriële schaal.

Computationele simulaties hebben een belangrijke rol gespeeld in het opbouwen van kennis rond CO_2 electrokatalyse processen. Het simuleren van eCO_2R is een multi-schaal uitdaging vanwege de verschillende gekoppelde fysische fenomenen gaande over zeer grote lengte- en tijdsschalen. In deze thesis gebruiken we computationele technieken op meerdere schalen om de mechanistische en omgevings drijvende krachten te begrijpen op de prestatie van het systeem. We focussen op systemen met metallische katalysators die koolstof monoxide (CO) produceren en met waterige elektrolyten vanwege hun praktische belangrijkheid. Maar, verschillende aspecten van onze conclusies zijn breed toepasbaar op andere eCO_2R systemen.

Zilver (Ag) electrokatalysatoren tonen veelbelovende prestaties voor CO productie met hoge selectiviteit. Echter, thermodynamische voorspellingen die gebruik maken van *ab-initio* densiteit functionele theorie (density functional theory, DFT) berekeningen voorspellen dat formaat ($HCOO^-$) het meer energetische interessante reactiepad is voor Ag. We bespreken dit schijnbaar verschil tussen theoretische en experimentele be-

vindingen gebruik makend van DFT simulaties en *in-situ* oppervlakte-versterkend Raman spectroscopie (surface-enhanced Raman spectroscopy, SERS) experimenten. We vinden dat oppervlakte geadsorbeerd waterstof ($*$H) een bepalende rol speelt in het bepalen van de selectiviteit tussen reactiepaden tijdens eCO_2R. Factoren zoals als solvatie, water-shuttling van protonen en laterale adsorptie interacties, helpen samen te verklaren hoe de CO, $HCOO^-$ en H_2 reactie paden interageren in complexe manieren op het Ag oppervlak resulterende in hoge selectiviteit voor CO.

Het is duidelijk door onze DFT studies op Ag, alsook de experimentele resultaten in de literatuur, dat de performantie van de eCO_2R afhangt van de eigenschappen van de reactie grensvlak eerder dan simpelweg het katalysator oppervlak. De reactie grensvlak is samengesteld uit een geladen katalysator oppervlak aan een constant potentiaal naast een waterig elektrolyt. Om de reactie omgeving te begrijpen voor eCO_2R katalytische processen, gebruiken we een continue benadering om de transport processen te modelleren in het elektrolyt naast het katalysator oppervlakte. We gebruiken het veralgemeende gemodificeerde Poisson-Nernst-Planck (generalized modified Poisson-Nernst-Planck, GMPNP) model om elektrostatische migratie, diffusie en buffer reactie kinetieken op te lossen met passende grenscondities terwijl volume exclusie vanwege de grootte van de deeltjes in de oplossing in rekening gebracht wordt. De resultaten van het GMPNP model demonstreert hoe sterische effecten en elektrostatische migratie een cruciale rol speelt in het bepalen van de CO_2 concentratie en pH dichtbij de katalysator oppervlakte. Onze aanpak toont de significantie van het in rekening brengen van de elektrische dubbellaag (electrical double layer, EDL) om de eCO_2R accuraat te bestuderen.

CO_2 conversie stromen > 200 mA/cm^2 zijn nodig voor de eCO_2R technologie om praktisch haalbaar te worden. Daarom verschuiven we onze aandacht naar gas diffusie electrode (gas diffusion electrode, GDE) gebaseerde flowcell setups die opmerkbare hogere stroomdensiteiten kan behalen vanwege een betere massa transport. We verruimen het GMPNP model om de reactie condities te bestuderen binnen een effectieve drie dimensionele katalysator porie in een flowcell als een functie van de katalysator structuur eigenschappen en operatie condities. Onze analyse geeft aan dat de katalysator laag diepte en de grenscondities aan de gas-elektrolyt en elektrolyt-elektrolyt grensvlakken zeer veel invloed hebben voor de pH en ion concentratie in een katalysator porie. We duiden de

massa transport in een GDE-gebaseerde eCO_2R setup als een belangrijke parameter om de prestatie van de katalysator te controleren.

In deze thesis simuleren we verschillende aspecten van het eCO_2R systeem, gaande van reactiepaden op atomisch niveau, tot reactie condities op het praktische niveau van het toestel. We tonen aan dat de selectiviteit van de electrokatalytische processen kunnen significant beïnvloed worden door fenomenen op het katalysator oppervlak, de EDL en binnen de katalysator laag als een geheel. Een hiërarchische aanpak tot systeem ontwerp, rekening houdend met invloedrijke parameters op elke schaal, kan daarom nuttig zijn om optimale prestaties te bereiken. De complexe multischaal natuur van het eCO_2R proces heeft nood aan het ontwikkelen van een simulatie omkadering dat de fenomenen op verschillende schalen kan integreren om beter experimentele observaties te voorspellen. Daarboven, benchmarken en systematische data collectie van beide, simulatie resultaten en experimentele observaties, zullen een grote meerwaarde bieden voor de convergentie naar rationeel ontworpen hoge prestaties leverende eCO_2R systemen. Elektrochemische conversie van CO_2 naar laag-koolstof koolwaterstoffen op industrieel niveau kan een potentiele gamechanger worden op het pad naar klimaatsverandering mitigatie. Er blijft nog wel een eindje te gaan en computationele simulaties zullen waardevol blijven om dit mogelijk te maken op dit pad.

1

Outline

Electrochemical reduction of carbon dioxide (CO_2) is a promising technological solution for the realization of an integrated low-carbon energy and materials system. There are currently numerous outstanding challenges for the practical and large-scale application of CO_2 electrocatalysis (eCO_2R). Computational simulations have an important role to play in developing the physical understanding to inform the design of optimized catalysts, interfaces and the overall process configuration. This thesis aims to address some of the critical research questions in eCO_2R through computational models at multiple scales.

1.1. Research Questions

The results reported in this dissertation pertain to following research questions.

1. *Catalyst selectivity*: What determines the competition between two-electron CO_2 reduction pathways on silver (Ag) electrocatalysts? To what extent do solvation and lateral adsorbate interactions influence the reaction energetics? Why do Ag catalysts produce carbon monoxide and not formate as a reduction product?

2. *Reaction interface*: What is the nature of the reaction environment at the catalyst-electrolyte interface at practically relevant potentials

during eCO_2R? How can the properties of the interface influence the access of CO_2 to the catalyst and the local pH? How important are electrostatic effects in defining the catalytic interface?

3. *Mass transport in practical systems*: To what extent do the structural and operational parameters of gas diffusion electrode (GDE)-based flow cells influence the reaction environment within the catalyst pores? What are the most important parameters determining the pH and concentration of ions and CO_2 within the porous catalyst layer at practical current densities?

1.2. Chapter Outline

The chapter-wise organization of the dissertation is given below.

- Chapter 2 provides the context for electrochemical CO_2 reduction and where the technology fits within the transition towards sustainable energy and materials. It provides an overview of the current status of the eCO_2R technology, the outstanding bottlenecks and the role of computational research within this scope.

- Chapter 3 provides a view of the eCO_2R modeling problem from three scales. Firstly, a surface catalysis view with atomic scale simulations used to model catalyst reactivity (section 3.1). Secondly, a catalyst-electrolyte interface view where the properties of the interface, as opposed to just the catalyst surface, are taken into account within the modeling approach (section 3.2). Thirdly, a device-scale view where mass transport becomes a decisive factor for catalytic performance with continuum models as tools for device engineering (section 3.3).

- Chapter 4 uses density functional theory (DFT)-based atomistic simulations to calculate the thermodynamic and kinetic energy barriers for 2-electron reduction products on high symmetry Ag surfaces. By using Bader charge analysis, implicit solvation, and accounting for lateral adsorbate interactions, we attempt to elucidate why Ag is selective towards carbon monoxide as opposed to formate.

- Chapter 5 uses a continuum one-dimensional generalized modified Poisson-Nernst-Planck (GMPNP) model to resolve the electrical double layer (EDL) in an eCO_2R system at steady state. The results of the GMPNP model are used to establish the importance of electrostatic forces and steric effects for the transport of CO_2 to the catalyst surface, pH and the accumulation of cations at the interface.

- Chapter 6 extends the GMPNP model from chapter 5 to a three-dimensional catalytic pore within a GDE-based flow-cell setup. The model is used to study the influence of operating conditions and structural parameters of the catalyst layer on the median reaction conditions within the pore. The chapter emphasizes the significance of the gas-electrolyte and electrolyte-electrolyte interfaces for determining reaction conditions in practical systems, in addition to the catalyst-electrolyte interface studied in the previous chapter.

- Chapter 7 offers future perspective in the context of the results presented in this thesis.

Chapters 4 and 5 are based on peer-reviewed journal articles whereas chapter 6 is based on the results currently under preparation for publication.

2

Electrochemical reduction of CO_2

2.1. Climate change and CO_2

The element carbon (C) is fundamental for the existence of all life on Earth. Its flow through our planet's landmass, geology, oceans, and atmosphere forms a closed loop known as the *carbon cycle*. *Greenhouse gases* (GHG) such as carbon dioxide (CO_2), methane (CH_4), water vapour, nitrous oxide (N_2O), and ozone, absorb the thermal radiation which is reflected from the earth's surface and reflect it back into the atmosphere. Without the warming effect of GHGs, life on Earth would not be possible. The carbon cycle helps control the planet's temperature by regulating the quantities of CO_2 and CH_4 in the atmosphere.

Burning of fossil fuels in the past century has disrupted the balance of the carbon cycle by moving large quantities of C from the ground (fossils) into the atmosphere in the form of CO_2 [1]. Since the removal of CO_2 from the atmosphere via the carbon cycle is a very slow process, the CO_2 released in the atmosphere through the burning of fossil fuels can stay there for tens of thousands of years [2]. Due to the combination of a very high emission rate, very long atmospheric life-time, and its greenhouse effects, the focus of much of the global warming mitigation effort and discussion has centered around the CO_2 molecule.

A shift in the carbon cycle because of the higher atmospheric levels of CO_2 results in several cascading effects that go beyond just increasing

temperatures (Figure 2.1). These include: rising sea levels, ecosystem collapse, species extinction due to changing environmental conditions, threat to health, food, and water security of society, increased occurrence of extreme weather events and unpredictable weather patterns [1].

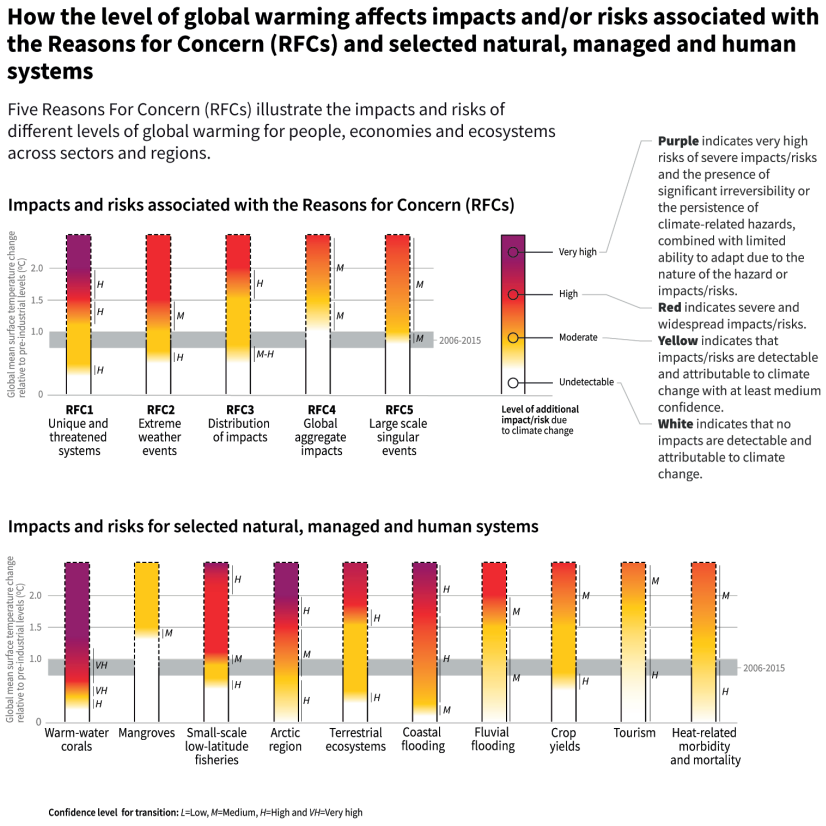

Figure 2.1: Level of risk for natural and human systems for different levels of global warming. Figure reproduced from reference Masson-Delmottea *et al.* [3, Figure SPM.2].

2.2. Mitigation options against climate change

Since the industrial revolution, emissions of CO_2 due to human activities have already resulted in a warming of around 1°C in the global average surface temperature [3]. The *Intergovernmental Panel on Climate Change* (IPCC) has described ways for limiting warming to 1.5°C and the associated risks of climate change [3]. Figure 2.2 shows forecasts of the global average surface temperature under multiple scenarios; the shaded portions in the graph show the forecast uncertainty. It is clear that a rapid decline of CO_2 emissions over the next two to three decades to reach net-zero is necessary to prevent a catastrophic rise in the average global surface temperature. Additionally, emissions of other GHGs such as CH_4, N_2O, and aerosols also need to be curtailed significantly in this period.

All proposed and projected routes to a 1.5°C warmer world involve a higher share of electricity as the energy source for end use, with the majority of the electricity generation through renewable sources such as wind and solar [1]. The increasing share of renewable electricity reduces the intensity of both, CO_2, and methane emissions of the energy supply. Adoption of renewable energy is expected to be driven by favorable economics and other system-wide benefits in several parts of the world [4–7]. A higher share of wind and solar energy brings with it challenges of intermittency, and it needs simultaneous development of electricity storage technologies to improve the flexibility of electrical grids [8–10]. A lack of suitable and competitive electricity storage options can become a major bottleneck for the large-scale adoption of renewable electricity generation.

Industrial processes and transportation combined contribute ~45% of the global GHG emissions [1]. Transitioning these sectors to reach net-zero emissions by 2040-2050 is a technologically and economically challenging task requiring major improvements in efficiency, electrification of manufacturing processes and substitution of current fossil fuel raw materials with sustainable ones [3, 11, 12]. Industry, in particular chemicals, cement, iron and steel manufacturing, aviation, shipping, and transportation sectors pose some of the hardest challenges towards decarbonisation as well as reduced non-CO_2 emissions [10, 13]. The difficulty in reducing CO_2 emissions in these sectors arises from factors such as requirement of high energy intensity, C-based building blocks for materials and processes which are hard to replace, and a growing demand for these industries

2

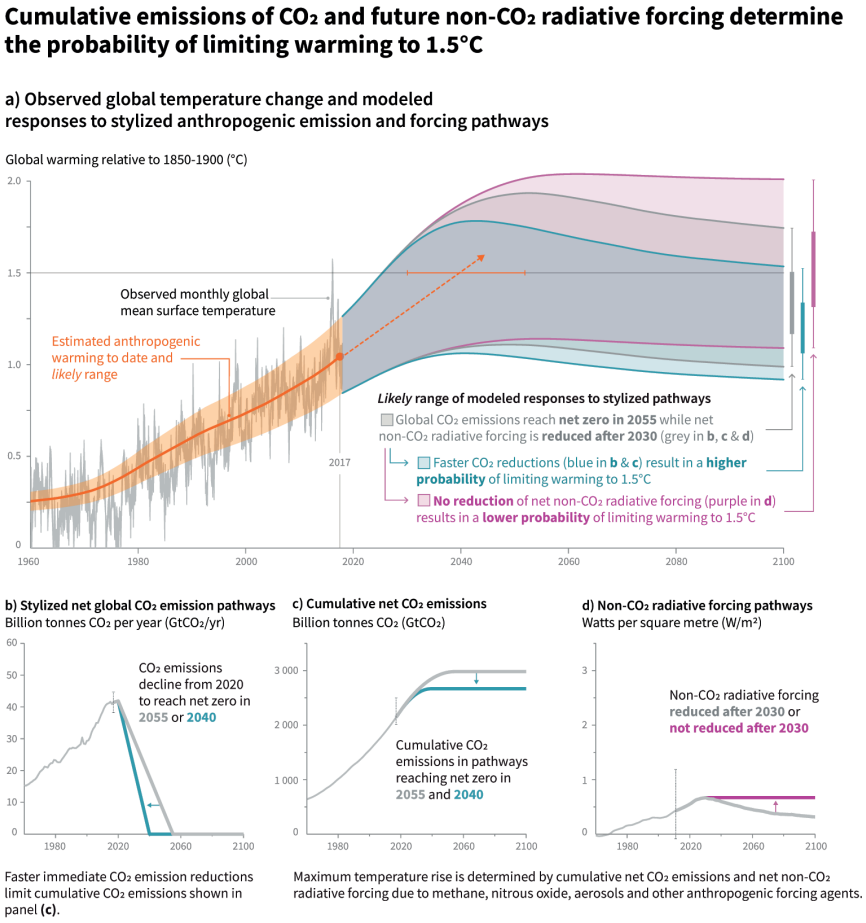

Figure 2.2: Evolution of mean global surface temperature over time for multiple emission scenarios. Figure reproduced from reference Masson-Delmottea *et al.* [3, Figure SPM.1].

for growth-driven economic activity [13]. *Carbon dioxide removal* (CDR) in the order of 100-1000 $GtCO_2$ is considered as a potentially important mitigation measure to constrain atmospheric CO_2 emissions from these sectors in order to meet the requirements for the 1.5°C-2°C warming scenario [3, 14].

Figure 2.3 shows the estimated stocks of C on earth, the various CDR and *carbon capture and utilization* (CCU) pathways, and the current flow of CO_2 to and from the atmosphere. There is currently significant uncertainty in the large-scale and wide-spread deployment of CDR/CCU technologies due to the lack of policy incentives, challenges of upscaling, and potential trade-offs [3, 15, 16]. Additionally, although reversing the average surface temperature rise in case of an overshoot beyond the 1.5°C-2°C warming scenarios might be possible, the effects of the warming such as sea-level rise and ecological damage are not considered reversible [17]. Therefore, even though CDR will play an important role in complimenting other efforts to reach the net-zero CO_2 emission target over the next three decades, extensive reliance on CDR as a mitigation mechanism for climate change is not desirable.

2.3. The case for electrochemical conversion of CO_2

Utilizing CO_2 as a feedstock for fuels, chemicals and building materials is becoming an increasingly competitive technology that can contribute to decarbonizing industrial and transportation sectors to meet emission reduction targets [18, 19]. Conversion of CO_2 using renewable energy can displace fossil-based feedstocks as a source of C to produce materials and chemicals [20]. Life-cycle analysis (LCA) studies have shown that not only can CO_2 conversion act as a sink to curtail emissions through long-lasting C-based products, production routes using CO_2 as the source of C can diminish the footprint of certain manufacturing processes relative to the existing fossil-based routes [16, 21]. Another important conclusion from these studies is that CCU does not always imply CDR. LCA studies with the appropriate methodology for CCU pathways within their specific context are essential to establish their respective CDR potential.

The largest gains in emission reduction over the life-cycle of CCU processes can be made for the so-called Power-to-X (PtX) routes [21]. In a typical PtX scheme, renewable electricity is used to generate hydrogen

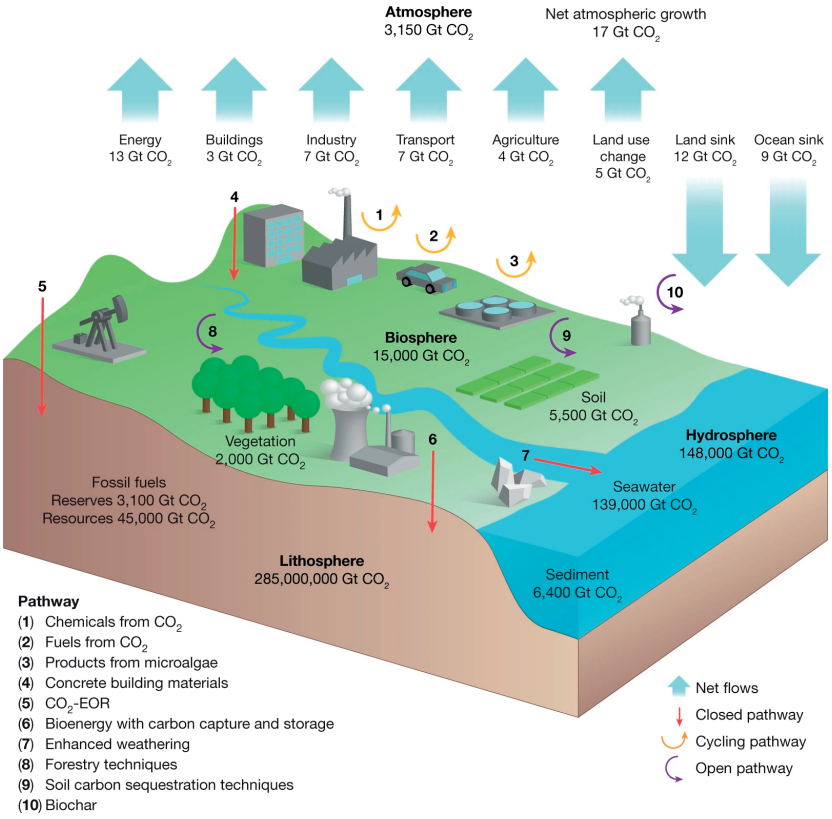

Figure 2.3: Carbon dioxide removal and utilization pathways and net flows through the atmosphere. Red arrows are closed pathways signifying near-permanent removal of CO_2; yellow arrows are cycling pathways in which CO_2 moves through industrial systems in time scales of days to months; purple arrows are open pathways signifying large CO_2 removal potential but in potentially leaky systems. Blue block arrows represent annual fluxes of CO_2 to and from the atmosphere averaged over the period of 2007-2018. The CO_2 equivalent C stocks on earth are shown for atmosphere, biosphere, hydrosphere and lithosphere. Figure reproduced from reference [15] with permission. Copyright 2019, Nature publishing.

(H_2) through electrochemical water-splitting, which is already a commercial technology and continues to become economically competitive [22]. This renewable or so-called "green" H_2 can be used directly in fuel cells or can be used in chemical processes where it reacts with captured CO_2 to generate hydrocarbon molecules such as syngas, methane, methanol, Fischer-Tropsch (FT) liquids, dimethyl ether (DME), ethanol, etc., which can be fed directly into the existing fuels and chemicals value chain. Converting renewable electricity to chemical energy through PtX can help manage the intermittency of renewable electricity and can provide the necessary grid flexibility for high adaption of renewable electricity [23, 24]. PtX therefore interacts with both, the electricity grid management, and the chemicals and fuels supply chain, to contribute to an integrated low-C energy and materials system.

The integration of renewable energy and CO_2 conversion can be done through multiple routes [25, 26] namely, photosynthesis [27, 28], photocatalysis [29–31], thermal catalysis [21, 32–34] or electrocatalysis [35–37]. The electrochemical conversion route directly uses renewable electricity to reduce CO_2 to products such as carbon monoxide, formate, methanol, methane, ethanol and ethylene [38]. The process of electrochemical reduction of CO_2 (eCO_2R) is therefore in-line with the PtX scheme, delivering system integration benefits of grid management and production of low-C hydrocarbon (LCHC) molecules. PtX using eCO_2R is sometimes termed as the direct route to LCHCs whereas electrochemically producing H_2 to further react with CO_2 to form LCHCs is termed as the indirect route. Figure 2.4 shows the pathways for the direct and indirect conversion of CO_2 to industrially relevant hydrocarbon feedstocks. Considerable improvements have been realized in the performance of eCO_2R systems over the past few decades through accelerated academic and commercial R&D efforts in the area. The following sections will briefly provide a state-of-the-art of the performance of current eCO_2R systems and the outlook for future developments in the field.

2.4. Current status of CO_2 electrocatalysis technology

The reduction of CO_2 takes place at the cathode surface which is kept at a negative potential using renewable electricity as the energy input. The cathode catalyst can be a d-block metal, a p-block metal or ox-

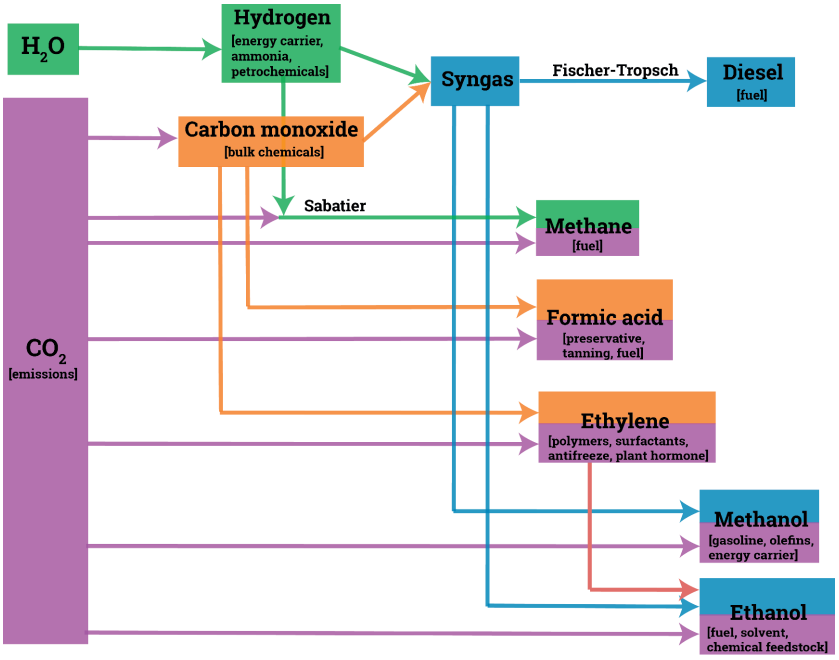

Figure 2.4: Pathways to convert CO_2 directly (in purple), or indirectly, via carbon monoxide (CO, in orange) and syngas (in blue) to chemical feedstocks. Pathways involving hydrogen (H_2) derived through water electrolysis are shown in green. Boxes with multiple colours imply a possibility of both a direct route and indirect route to production. The use cases for the reduction products are given in square brackets.

ide, doped carbon-based materials, homogeneous molecular redox couple, chalcogenide or an enzyme [39]. The equation 2.1 shows a general reaction for the reduction of CO_2 in the presence of H_2O to form a product and hydroxide ions (OH^-) as a by-product, and using electrons for the thermodynamic driving force.

$$xCO_2(aq) + yH_2O(aq) + ze^- \rightleftharpoons \text{Product} + qOH^-(aq) \tag{2.1}$$

Figure 2.5 shows general schemes for an eCO_2R system. Research in eCO_2R systems has progressively moved from setups such as in Figure 2.5a where the electrolyte is saturated with CO_2, to setups like Figure

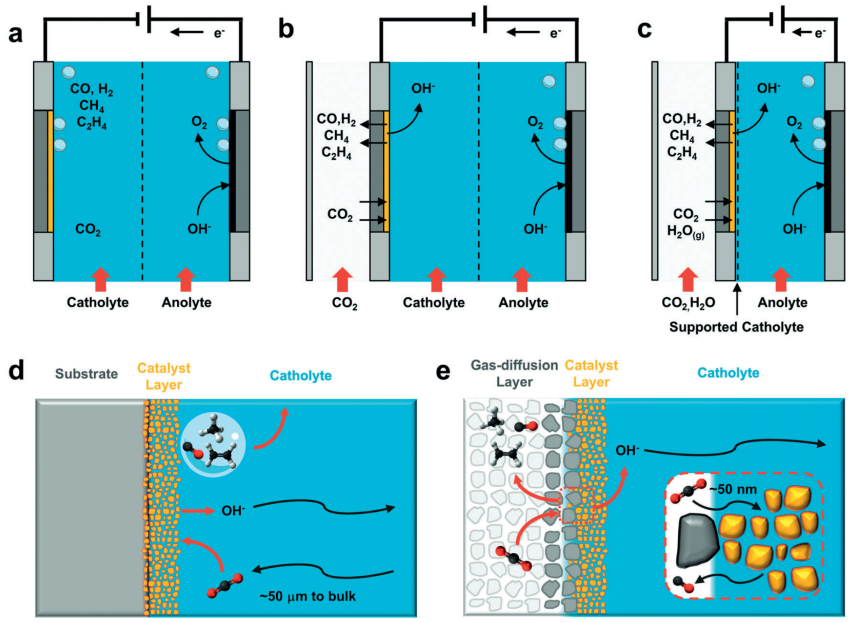

Figure 2.5: Illustration of cell configurations for CO_2 electrocatalysis. a) H-cell type configuration, b) GDE-based configuration with CO_2 fed in gas phase with aqueous catholyte, c) GDE-based configuration with humidified CO_2 fed in gas phase with solid supported catholyte, d) mass transport of CO_2 from bulk of catholyte to the catalyst surface in a H-cell system configuration, e) mass transport of CO_2 through the gas diffusion media to the catalyst surface in a GDE-based configuration. The anode reaction for all configurations a), b) and c) is shown as water (H_2O) oxidation to form O_2 as an example. Figure reproduced from reference [40].

2.5b and 2.5c where the CO_2 is fed to the system in vapour phase. The former is typically referred to as an H-cell type setup whereas the later is a gas diffusion electrode (GDE)-based system. GDE-based systems can achieve a significantly higher mass transport rate of CO_2 to the catalyst surface by shortening the diffusion path of CO_2 (Figure 2.5d *vs.* 2.5e) and consequently show a considerably superior performance relative to H-cells [40–44].

Techno-economic studies for eCO_2R systems have shown that a threshold current density, signifying the rate of CO_2 reduction per catalyst surface area, in the range of 200 - 400 mA/cm^2 is needed to be reached for a

commercially viable process [45–48]. This is in addition to requirements of high product selectivity, energy efficiency and a minimum catalyst stability in the order of thousands of hours. GDE-based setups have shown promising performance for reduction of CO_2 to products such as carbon monoxide [49–52], formate [53–55], methanol [56, 57], ethanol [58–62] and ethylene [63, 64]. Products involving 2 electron transfers in the reduction reaction (z=2 in equation (2.1)), namely carbon monoxide (CO), and formic acid (HCOOH) are the closest to achieving economic feasibility based on current performance of lab setups [45, 48, 65]. Electrochemical production of syngas (CO + H_2) coupled with the FT process to produce low-C diesel as aviation fuel or coupled with fermentation processes to produce high value chemicals are some of the promising directions for commercialization of eCO_2R [36, 47]. Producing formic acid using eCO_2R has a small climate change mitigation potential due to a relatively small global market, but the process can nonetheless act as a platform for the commercial development of the technology. Figure 2.4 shows a schematic of some of the possible routes to go from CO_2 and H_2O to chemical feedstocks. Since eCO_2R systems typically employ aqueous electrolytes, reduction of H_2O (HER) competes with eCO_2R to form H_2, thereby reducing the selectivity of the desired products. Controlling the competition and interaction between the eCO_2R and HER reaction pathways is one of the challenges for designing high performing systems. Higher electron transfer eCO_2R reactions are accompanied with diminishing selectivity due to branching out of the reaction mechanisms and lower energy efficiency. However, significant progress has been made in the production of C_2 products ethylene (C_2H_4) and ethanol (C_2H_5OH) via eCO_2R over the past decade [42, 66]. eCO_2R to ethylene either directly or indirectly via carbon monoxide (Figure 2.4) is an attractive avenue to pursue owing to a relatively large market size as well as CO_2 emissions reduction potential [36].

CO_2 utilization rates in the order of gigatons per annum need to be realized for a meaningful contribution to climate change mitigation targets (Figure 2.3). Some of the biggest outstanding challenges in the path to commercial feasibility of eCO_2R have to do with the scaling-up of the electrolyzers in a cost-competitive manner. Current single-pass conversion yields are low and need to be increased for efficient implementation of downstream separation processes. Process conditions such as pressure and temperature used for studying and optimizing the performance of

lab-scale eCO_2R systems need to approach the expected operating conditions at industrial scale based on integration schemes with upstream and downstream process units [37]. In the same vein, eCO_2R systems need to be tested for flexible on-demand operation if providing grid flexibility is one of the required functions. Catalyst stability has been identified as an important current bottleneck for long-term operation. In addition to developments in novel catalytic materials, improved cell architectures are expected to play an important role in achieving target performance thresholds of current density and energy efficiency [41, 67]. Development of standardized protocols for experimental data acquisition and analysis will help compare the performance of various systems under investigation and will shorten the development cycle [68, 69]. Lastly, external factors like the unit price for low-C electricity and carbon pricing schemes will ultimately play a decisive role in determining the industrial applicability of the eCO_2R process.

2.5. Role of computational simulations

eCO_2R is highly complex due to several coupled physical phenomena operating over vastly different length and time scales. Experimental analysis alone is often insufficient in isolating the influence of individual parameters on the observed performance of the system. Accessing the relevant time and length scales of the catalytic processes is also often not possible experimentally or requires extremely specialized and resource intensive infrastructure. Computational research has therefore become an important tool to address the gaps outlined in the previous section and is used widely to compliment and inform experimental studies.

Simulations at the atomistic scale have been used extensively to derive the thermodynamic and kinetic energy barriers for reaction pathways as a means to understand the activity and selectivity of electrocatalysts towards desired products [46, 70, 71]. Density functional theory (DFT)-based simulations have contributed tremendously in building the mechanistic understanding of the formation of C_1 products such as CO and formate ($HCOO^-$), as well as C_2 and higher reduction products through C−C coupling [72, 73]. At the system scale, continuum mass transport models have proven very useful in understanding the reaction environment and engineering high performing device architectures for better yields [44].

Studying the long-term stability of catalysts using simulations is a relatively under-developed area of research but is expected to become important considering its relevance for scale-up. Chapter 3 will go deeper into the physical phenomena relevant for eCO_2R and how simulations at multiple scales can be used to study and optimize these processes.

References

[1] O. Edenhofer, R. Pichs-Madruga, Y. Sokona, E. Farahani, S. Kadner, K. Seyboth, A. Adler, I. Baum, S. Brunner, P. Eickemeier, B. Kriemann, J. Savolainen, S. Schlömer, C. von Stechow, T. Zwickel, and J. Minx (eds.), *Cambridge University Press, Cambridge, United Kingdom and New York, NY, USA*, Tech. Rep. (Intergovernmental Panel on Climate Change, 2014).

[2] D. Archer, M. Eby, V. Brovkin, A. Ridgwell, L. Cao, U. Mikolajewicz, K. Caldeira, K. Matsumoto, G. Munhoven, A. Montenegro, and K. Tokos, *Atmospheric lifetime of fossil fuel carbon dioxide,* Annual Review of Earth and Planetary Sciences **37**, 117 (2009).

[3] V. Masson-Delmottea, P. Zhai, H. O. Pörtner, D. Roberts, J. Skea, P. Shukla, A. Pirani, W. Moufouma-Okia, C. Péan, R. Pidcock, S. Connors, J. B. R. Matthews, Y. Chen, X. Zhou, M. I. Gomis, E. Lonnoy, T. Maycock, M. Tignor, and T. W. (eds.), *IPCC, 2018: Global warming of 1.5° C. An IPCC Special Report on the impacts of global warming of 1.5° C above pre-industrial levels and related global greenhouse gas emission pathways, in the context of strengthening the global response to the threat of climate change, sustainable development, and efforts to eradicate poverty* (2018).

[4] A. Grubler, C. Wilson, N. Bento, B. Boza-Kiss, V. Krey, D. L. McCollum, N. D. Rao, K. Riahi, J. Rogelj, S. De Stercke, J. Cullen, S. Frank, O. Fricko, F. Guo, M. Gidden, P. Havlík, D. Huppmann, G. Kiesewetter, P. Rafaj, W. Schoepp, and H. Valin, *A low energy demand scenario for meeting the* $1.5^\circ C$ *target and sustainable development goals without negative emission technologies,* Nature Energy **3**, 515 (2018).

[5] V. Krey, G. Luderer, L. Clarke, and E. Kriegler, *Getting from here*

to there – energy technology transformation pathways in the EMF27 scenarios, Climatic Change **123**, 369 (2014).

[6] D. Gielen, F. Boshell, D. Saygin, M. D. Bazilian, N. Wagner, and R. Gorini, *The role of renewable energy in the global energy transformation,* Energy Strategy Reviews **24**, 38 (2019).

[7] J. Rogelj, A. Popp, K. V. Calvin, G. Luderer, J. Emmerling, D. Gernaat, S. Fujimori, J. Strefler, T. Hasegawa, G. Marangoni, V. Krey, E. Kriegler, K. Riahi, D. P. van Vuuren, J. Doelman, L. Drouet, J. Edmonds, O. Fricko, M. Harmsen, P. Havlík, F. Humpenöder, E. Stehfest, and M. Tavoni, *Scenarios towards limiting global mean temperature increase below* $1.5°C$*,* Nature Climate Change **8**, 325 (2018).

[8] P. Denholm and M. Hand, *Grid flexibility and storage required to achieve very high penetration of variable renewable electricity,* Energy Policy **39**, 1817 (2011).

[9] B. Dunn, H. Kamath, and J.-M. Tarascon, *Electrical energy storage for the grid: A battery of choices,* Science **334**, 928 (2011).

[10] IRENA, *Global Renewables Outlook: Energy transformation 2050*, Tech. Rep. (International Renewable Energy Agency, Abu Dhabi, 2020).

[11] M. Åhman, L. J. Nilsson, and B. Johansson, *Global climate policy and deep decarbonization of energy-intensive industries,* Climate Policy **17**, 634 (2017).

[12] C. Bataille, M. Åhman, K. Neuhoff, L. J. Nilsson, M. Fischedick, S. Lechtenböhmer, B. Solano-Rodriquez, A. Denis-Ryan, S. Stiebert, H. Waisman, O. Sartor, and S. Rahbar, *A review of technology and policy deep decarbonization pathway options for making energy-intensive industry production consistent with the Paris Agreement,* Journal of Cleaner Production **187**, 960 (2018).

[13] I. E. Agency, *Transforming Industry through CCUS*, Tech. Rep. (IEA, Paris, 2019).

[14] *Negative emissions-Part 1: Research landscape and synthesis,* Environmental Research Letters **13**, 63001 (2018).

[15] C. Hepburn, E. Adlen, J. Beddington, E. A. Carter, S. Fuss, N. Mac Dowell, J. C. Minx, P. Smith, and C. K. Williams, *The technological and economic prospects for CO_2 utilization and removal,* Nature **575**, 87 (2019).

[16] N. von der Assen, J. Jung, and A. Bardow, *Life-cycle assessment of carbon dioxide capture and utilization: avoiding the pitfalls,* Energy Environ. Sci. **6**, 2721 (2013).

[17] K. B. Tokarska and K. Zickfeld, *The effectiveness of net negative carbon dioxide emissions in reversing anthropogenic climate change,* Environmental Research Letters **10**, 94013 (2015).

[18] I. E. Agency, *Putting CO_2 to Use*, Tech. Rep. (IEA, Paris, 2019).

[19] R. Chauvy, N. Meunier, D. Thomas, and G. D. Weireld], *Selecting emerging CO_2 utilization products for short- to mid-term deployment,* Applied Energy **236**, 662 (2019).

[20] R. Schlögl, *The role of chemistry in the energy challenge,* ChemSusChem **3**, 209 (2010).

[21] J. Artz, T. E. Müller, K. Thenert, J. Kleinekorte, R. Meys, A. Sternberg, A. Bardow, and W. Leitner, *Sustainable conversion of carbon dioxide: An integrated review of catalysis and life cycle assessment,* Chemical Reviews **118**, 434 (2018).

[22] IRENA, *Hydrogen: A renewable energy perspective*, Tech. Rep. (International Renewable Energy Agency, Abu Dhabi, 2019).

[23] B. Zakeri and S. Syri, *Electrical energy storage systems: A comparative life cycle cost analysis,* Renewable and Sustainable Energy Reviews **42**, 569 (2015).

[24] X. Zhang, S. H. Chan, H. K. Ho, S.-C. Tan, M. Li, G. Li, J. Li, and Z. Feng, *Towards a smart energy network: The roles of fuel/electrolysis cells and technological perspectives,* International Journal of Hydrogen Energy **40**, 6866 (2015).

[25] M. Bailera, P. Lisbona, L. M. Romeo, and S. Espatolero, *Power to gas projects review: Lab, pilot and demo plants for storing renewable*

energy and CO_2, Renewable and Sustainable Energy Reviews **69**, 292 (2017).

[26] E. V. Kondratenko, G. Mul, J. Baltrusaitis, G. O. Larrazábal, and J. Pérez-Ramírez, *Status and perspectives of CO_2 conversion into fuels and chemicals by catalytic, photocatalytic and electrocatalytic processes,* Energy Environ. Sci. **6**, 3112 (2013).

[27] S. A. Razzak, M. M. Hossain, R. A. Lucky, A. S. Bassi, and H. d. Lasa], *Integrated CO_2 capture, wastewater treatment and biofuel production by microalgae culturing—A review,* Renewable and Sustainable Energy Reviews **27**, 622 (2013).

[28] W. Y. Cheah, P. L. Show, J.-S. Chang, T. C. Ling, and J. C. Juan, *Biosequestration of atmospheric CO_2 and flue gas-containing co2 by microalgae,* Bioresource Technology **184**, 190 (2015).

[29] W. Tu, Y. Zhou, and Z. Zou, *Photocatalytic conversion of CO_2 into renewable hydrocarbon fuels: State-of-the-art accomplishment, challenges, and prospects,* Advanced Materials **26**, 4607 (2014), https://onlinelibrary.wiley.com/doi/pdf/10.1002/adma.201400087 .

[30] K. Li, B. Peng, and T. Peng, *Recent advances in heterogeneous photocatalytic CO_2 conversion to solar fuels,* ACS Catalysis **6**, 7485 (2016).

[31] X. Chang, T. Wang, and J. Gong, *CO_2 photo-reduction: insights into CO_2 activation and reaction on surfaces of photocatalysts,* Energy Environ. Sci. , 2177.

[32] M. Götz, J. Lefebvre, F. Mörs, A. M. Koch], F. Graf, S. Bajohr, R. Reimert, and T. Kolb, *Renewable Power-to-Gas: A technological and economic review,* Renewable Energy **85**, 1371 (2016).

[33] S. R. Foit, I. C. Vinke, L. G. J. de Haart, and R.-A. Eichel, *Power-to-syngas: An enabling technology for the transition of the energy system?* Angewandte Chemie International Edition **56**, 5402 (2017).

[34] S. Brynolf, M. Taljegard, M. Grahn, and J. Hansson, *Electrofuels for the transport sector: A review of production costs,* Renewable and Sustainable Energy Reviews **81**, 1887 (2018).

[35] D. T. Whipple and P. J. A. Kenis, *Prospects of CO_2 utilization via direct heterogeneous electrochemical reduction,* The Journal of Physical Chemistry Letters **1**, 3451 (2010).

[36] P. De Luna, C. Hahn, D. Higgins, S. A. Jaffer, T. F. Jaramillo, and E. H. Sargent, *What would it take for renewably powered electrosynthesis to displace petrochemical processes?* Science **364**, eaav3506 (2019).

[37] W. A. Smith, T. Burdyny, D. A. Vermaas, and H. Geerlings, *Pathways to industrial-scale fuel out of thin air from CO_2 electrolysis,* Joule **3**, 1822 (2019).

[38] R. Kortlever, J. Shen, K. J. P. Schouten, F. Calle-Vallejo, and M. T. Koper, *Catalysts and reaction pathways for the electrochemical reduction of carbon dioxide,* Journal of Physical Chemistry Letters **6**, 4073 (2015).

[39] G. O. Larrazábal, A. J. Martín, and J. Pérez-Ramírez, *Building blocks for high performance in electrocatalytic CO_2 reduction: Materials, optimization strategies, and device engineering,* The Journal of Physical Chemistry Letters **8**, 3933 (2017).

[40] T. Burdyny and W. A. Smith, *CO_2 reduction on gas-diffusion electrodes and why catalytic performance must be assessed at commercially-relevant conditions,* Energy Environ. Sci. **12**, 1442 (2019).

[41] D. Higgins, C. Hahn, C. Xiang, T. F. Jaramillo, and A. Z. Weber, *Gas-diffusion electrodes for carbon dioxide reduction: A new paradigm,* ACS Energy Letters **4**, 317 (2019).

[42] L. Fan, C. Xia, F. Yang, J. Wang, H. Wang, and Y. Lu, *Strategies in catalysts and electrolyzer design for electrochemical CO_2 reduction toward C_{2+} products,* Science Advances **6** (2020), 10.1126/sciadv.aay3111.

[43] B. Endrődi, G. Bencsik, F. Darvas, R. Jones, K. Rajeshwar, and C. Janáky, *Continuous-flow electroreduction of carbon dioxide,* Progress in Energy and Combustion Science **62**, 133 (2017).

[44] S. Garg, M. Li, A. Z. Weber, L. Ge, L. Li, V. Rudolph, G. Wang, and T. E. Rufford, *Advances and challenges in electrochemical CO_2 reduction processes: an engineering and design perspective looking beyond new catalyst materials,* J. Mater. Chem. A **8**, 1511 (2020).

[45] M. Jouny, W. Luc, and F. Jiao, *General techno-economic analysis of CO_2 electrolysis systems,* Industrial & Engineering Chemistry Research **57**, 2165 (2018).

[46] M. G. Kibria, J. P. Edwards, C. M. Gabardo, C.-T. Dinh, A. Seifitokaldani, D. Sinton, and E. H. Sargent, *Electrochemical CO_2 reduction into chemical feedstocks: from mechanistic electrocatalysis models to system design,* Advanced Materials **31**, 1807166 (2019).

[47] J. M. Spurgeon and B. Kumar, *A comparative technoeconomic analysis of pathways for commercial electrochemical CO_2 reduction to liquid products,* Energy Environ. Sci. **11**, 1536 (2018).

[48] S. Verma, B. Kim, H.-R. Jhong, S. Ma, and P. J. A. Kenis, *A gross-margin model for defining technoeconomic benchmarks in the electroreduction of CO_2,* ChemSusChem **9**, 1972 (2016).

[49] T. Haas, R. Krause, R. Weber, M. Demler, and G. Schmid, *Technical photosynthesis involving CO_2 electrolysis and fermentation,* Nature Catalysis **1**, 32 (2018).

[50] S. Verma, Y. Hamasaki, C. Kim, W. Huang, S. Lu, H.-R. M. Jhong, A. A. Gewirth, T. Fujigaya, N. Nakashima, and P. J. Kenis, *Insights into the low overpotential electroreduction of CO_2 to CO on a supported gold catalyst in an alkaline flow electrolyzer,* ACS Energy Letters **3**, 193 (2017).

[51] S. Ma, R. Luo, J. I. Gold, Z. Y. Aaron, B. Kim, and P. J. Kenis, *Carbon nanotube containing ag catalyst layers for efficient and selective reduction of carbon dioxide,* Journal of Materials Chemistry A **4**, 8573 (2016).

[52] E. J. Dufek, T. E. Lister, S. G. Stone, and M. E. McIlwain, *Operation of a pressurized system for continuous reduction of co2,* Journal of The Electrochemical Society **159**, F514 (2012).

[53] D. T. Whipple, E. C. Finke, and P. J. Kenis, *Microfluidic reactor for the electrochemical reduction of carbon dioxide: the effect of pH,* Electrochemical and Solid-State Letters **13**, B109 (2010).

[54] X. Lu, D. Y. Leung, H. Wang, and J. Xuan, *A high performance dual electrolyte microfluidic reactor for the utilization of CO_2,* Applied Energy **194**, 549 (2017).

[55] H. Li and C. Oloman, *Development of a continuous reactor for the electro-reduction of carbon dioxide to formate - Part 1: Process variables,* Journal of Applied Electrochemistry **36**, 1105 (2006).

[56] X. Sun, Q. Zhu, X. Kang, H. Liu, Q. Qian, Z. Zhang, and B. Han, *Molybdenum–bismuth bimetallic chalcogenide nanosheets for highly efficient electrocatalytic reduction of carbon dioxide to methanol,* Angewandte Chemie International Edition **55**, 6771 (2016).

[57] W. Zhang, Q. Qin, L. Dai, R. Qin, X. Zhao, X. Chen, D. Ou, J. Chen, T. T. Chuong, B. Wu, *et al.*, *Electrochemical reduction of carbon dioxide to methanol on hierarchical Pd/SnO_2 nanosheets with abundant Pd-O-Sn interfaces,* Angewandte Chemie International Edition **57**, 9475 (2018).

[58] C. W. Li, J. Ciston, and M. W. Kanan, *Electroreduction of carbon monoxide to liquid fuel on oxide-derived nanocrystalline copper,* Nature **508**, 504 (2014).

[59] Y. Song, R. Peng, D. K. Hensley, P. V. Bonnesen, L. Liang, Z. Wu, H. M. Meyer III, M. Chi, C. Ma, B. G. Sumpter, *et al.*, *High-selectivity electrochemical conversion of CO_2 to ethanol using a copper nanoparticle/n-doped graphene electrode,* ChemistrySelect **1**, 6055 (2016).

[60] Y. Liu, Y. Zhang, K. Cheng, X. Quan, X. Fan, Y. Su, S. Chen, H. Zhao, Y. Zhang, H. Yu, *et al.*, *Selective electrochemical reduction of carbon dioxide to ethanol on a boron-and nitrogen-co-doped nanodiamond,* Angewandte Chemie International Edition **56**, 15607 (2017).

[61] T. T. Hoang, S. Verma, S. Ma, T. T. Fister, J. Timoshenko, A. I. Frenkel, P. J. Kenis, and A. A. Gewirth, *Nanoporous copper-silver*

alloys by additive-controlled electrodeposition for the selective electroreduction of CO_2 to ethylene and ethanol, Journal of the American Chemical Society **140**, 5791 (2018).

[62] T.-T. Zhuang, Z.-Q. Liang, A. Seifitokaldani, Y. Li, P. De Luna, T. Burdyny, F. Che, F. Meng, Y. Min, R. Quintero-Bermudez, *et al.*, *Steering post-C-C coupling selectivity enables high efficiency electroreduction of carbon dioxide to multi-carbon alcohols,* Nature Catalysis **1**, 421 (2018).

[63] T. T. H. Hoang, S. Ma, J. I. Gold, P. J. A. Kenis, and A. A. Gewirth, *Nanoporous copper films by additive-controlled electrodeposition: CO_2 reduction catalysis,* ACS Catalysis **7**, 3313 (2017).

[64] C.-T. Dinh, T. Burdyny, M. G. Kibria, A. Seifitokaldani, C. M. Gabardo, F. P. G. De Arquer, A. Kiani, J. P. Edwards, P. De Luna, O. S. Bushuyev, *et al.*, *CO_2 electroreduction to ethylene via hydroxide-mediated copper catalysis at an abrupt interface,* Science **360**, 783 (2018).

[65] A. Sternberg, C. M. Jens, and A. Bardow, *Life cycle assessment of CO_2-based C1-chemicals,* Green Chem. **19**, 2244 (2017).

[66] S. Nitopi, E. Bertheussen, S. B. Scott, X. Liu, A. K. Engstfeld, S. Horch, B. Seger, I. E. L. Stephens, K. Chan, C. Hahn, J. K. NÃžrskov, T. F. Jaramillo, and I. Chorkendorff, *Progress and perspectives of electrochemical CO_2 reduction on copper in aqueous electrolyte,* Chemical Reviews **119**, 7610 (2019).

[67] D. M. Weekes, D. A. Salvatore, A. Reyes, A. Huang, and C. P. Berlinguette, *Electrolytic CO_2 reduction in a flow cell,* Accounts of Chemical Research **51**, 910 (2018).

[68] E. L. Clark, J. Resasco, A. Landers, J. Lin, L.-T. Chung, A. Walton, C. Hahn, T. F. Jaramillo, and A. T. Bell, *Standards and protocols for data acquisition and reporting for studies of the electrochemical reduction of carbon dioxide,* ACS Catalysis **8**, 6560 (2018).

[69] R. Kas, K. Yang, D. Bohra, R. Kortlever, T. Burdyny, and W. A. Smith, *Electrochemical CO_2 reduction on nanostructured metal electrodes: fact or defect?* Chem. Sci. **11**, 1738 (2020).

[70] F. Calle-Vallejo and M. T. M. Koper, *First-principles computational electrochemistry: Achievements and challenges,* Electrochimica Acta **84**, 3 (2012).

[71] Y. Y. Birdja, E. Pérez-Gallent, M. C. Figueiredo, A. J. Göttle, F. Calle-Vallejo, and M. T. Koper, *Advances and challenges in understanding the electrocatalytic conversion of carbon dioxide to fuels,* Nature Energy **4**, 732 (2019).

[72] A. Rendón-Calle, S. Builes, and F. Calle-Vallejo, *A brief review of the computational modeling of CO_2 electroreduction on Cu electrodes,* Current Opinion in Electrochemistry **9**, 158 (2018).

[73] A. A. Peterson, F. Abild-Pedersen, F. Studt, J. Rossmeisl, and J. K. Nørskov, *How copper catalyzes the electroreduction of carbon dioxide into hydrocarbon fuels,* Energy Environ. Sci. **3**, 1311 (2010).

3

Simulating CO_2 electrocatalysis systems

This chapter will introduce the relevant physical and chemical phenomena at the different scales in eCO_2R systems along with the respective computational modeling approaches. Section 3.1 will discuss the atomic scale phenomena that determine the catalytic reactivity and how density functional theory (DFT)-based simulations have been used to study the different aspects of catalyst performance. Section 3.2 will describe the role of the reaction environment and the state-of-the-art of computational simulations to model the electrochemical interface in eCO_2R. Lastly, section 3.3 will discuss the mass transport aspects and the role of continuum models for system design.

3.1. Catalytic reactivity

The reduction reaction of the CO_2 molecules occurs on active sites on the catalytic surface, which provide a kinetically favorable reaction pathway to form the product molecules. The thermodynamic driving force for the reaction comes from the chemical potential of the electrons, which is a result of the externally applied potential to the cathode. The catalyst surface on the cathode provides adsorption sites for reaction intermediates and a typical catalytic process goes through several surface intermediates *via* a series of elementary steps. This implies that the nature of the catalyst

is very influential for the energetic cost of the conversion process. The stabilization of the reaction intermediates by the catalyst surface depends not only on the composition of the catalyst used, but also on its structure at the atomic level. Under-coordinated sites tend to have a stronger interaction with the adsorbed species and factors such as nanoparticle size, presence of catalyst support, surface promoters, alloying, confinement and surface defects play a role in determining the activity of a chosen catalyst [1–3].

3.1.1. Simulations at the atomic scale

A range of catalyst types have been investigated for eCO_2R as mentioned previously in section 2.4 of chapter 2. In this thesis, we will focus our attention on heterogeneous metal electrocatalysts for CO_2 reduction as they have so-far been the most widely studied and show the most promise performance for large-scale practical application [17, 18]. Figure 3.1 shows the proposed reaction networks for CO_2 reduction to various products on a polycrystalline copper (Cu) electrocatalyst. Cu has been widely studied for eCO_2R because of its ability to perform $>$ 2-electron transfers to form a variety of reduction products. Unlike Cu, the reaction network on other extensively studied catalysts such as silver (Ag) and gold (Au) terminates after two electron transfer steps resulting in only C_1 products carbon monoxide (CO) and formate ($HCOO^-$) [9, 17]. The competition between the various possible catalytic pathways through thermodynamic and kinetic energy barriers determines the selectivity of the catalyst and therefore the conversion efficiency towards a particular desired product.

Atomistic simulations based on DFT have played an indispensable role in establishing the reaction pathways for eCO_2R on the various catalyst surfaces. Some of the most important contested aspects of the mechanism of CO_2 reduction on electrocatalysts have been the initial activation step of CO_2 [17, 19], the coupling of C−C to form C_{2+} products [16, 19], and the transfer of H through a surface bound $*$H or water-shuttling as an important determinant for selectivity [20, 21].

The atomic structure and composition of the catalyst surface and near-surface layers influences the reaction energetics through the binding energy of surface intermediates [1]. The *coordination number* (CN) of the surface atoms is one of the important factors determining the adsorption energy

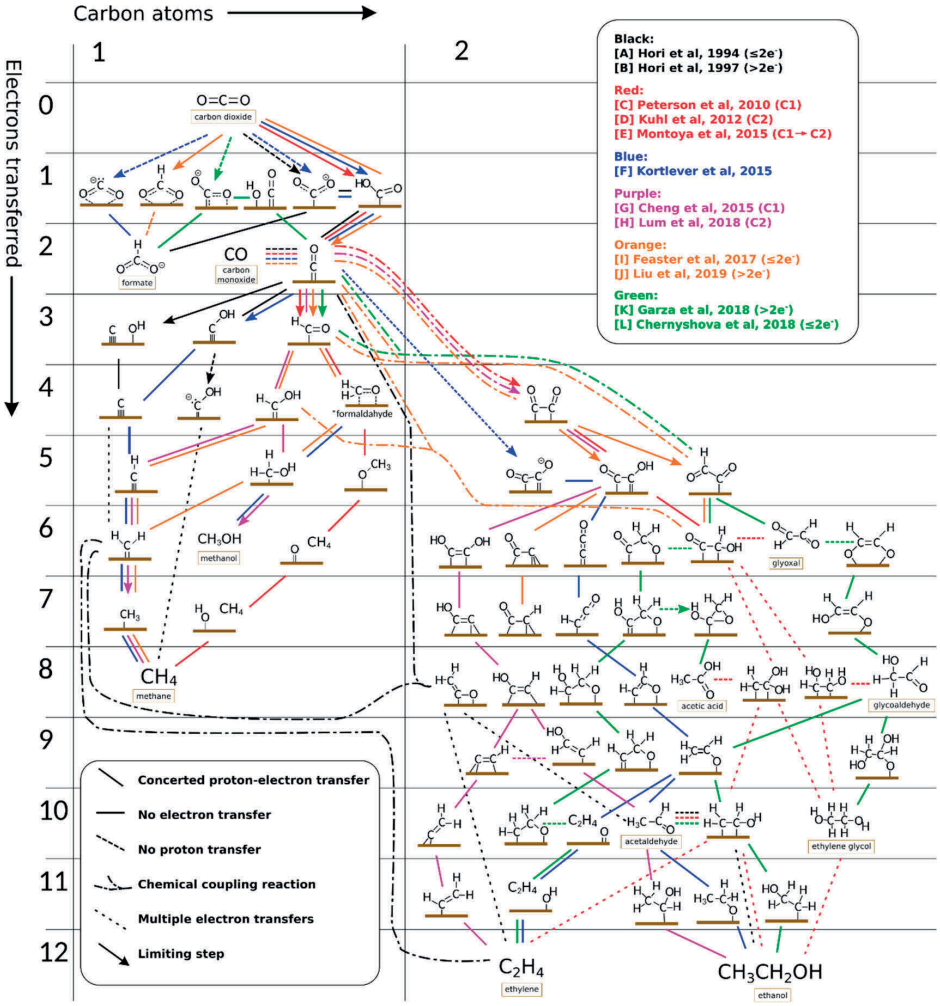

Figure 3.1: Reaction pathways reported in literature for CO_2 electroreduction on polycrystalline Cu. References mentioned in legend on top right: in black [4, 5], in red [6–8], in blue [9], in purple [10, 11], in orange [12, 13] and in green [14, 15]. The legend on the left bottom indicates the nature of the elementary reaction step. Figure reproduced from reference [16] with permission. Copyright 2019, American Chemical Society.

of binding atoms (ΔE_x) to the catalytic sites [22]. The CN follows an inverse relationship with ΔE_x and implies that under-coordinated surface sites bind reactive species more strongly. Following the Sabatier principle, ideal catalysts bind the reactive adsorbates neither too strongly nor too weakly [23]. As a result, the nature of surface facets, presence of steps, kinks and defects as well as the nanostructure shape and size are important for catalyst reactivity [1, 3]. Alloying of metal catalysts is a common approach for influencing the catalyst performance [16]. Alloying can affect the electronic structure of the binding sites on the surface through the composition, as well as by the way the atoms of different metallic identity are distributed on the surface and the sub-surface layers. Alloying can also lead to higher strain in the lattice structure of the catalyst and the various geometric and electronic effects combine to determine the overall activity [24]. Lastly, catalyst surfaces are dynamic in nature and change due to the interactions with adsorbed species and reaction environment while in operation [25, 26]. This influences the stability of the catalyst surfaces in addition to their energetic performance. Studying the dynamics of electrocatalyst surface restructuring and poisoning is computationally challenging and are a subject of relatively few reports in literature. *In-situ/operando* experimental techniques play an essential role in elucidating the state of the catalyst surface during operation to further guide computational investigation.

The interaction energy of adsorbates with transition metal surfaces is a function of some electronic property of the catalytic surface, or the so-called *descriptor* (D). As shown in Figure 3.2, conditional on the convexity of the energy curve as a function of D and the alignment of the unique minima that exists in the convex functions for multiple adsorbing species, a linear relationship will exist between the adsorption energy of the species [27, 28]. These linear scaling relationships have been used extensively in DFT-based computationally studies as a predictive and heuristic tool to derive catalysts with optimal thermodynamic energy profiles based on the so-called volcano plots [23, 29, 30]. The *computational hydrogen electrode* (CHE) technique has enabled the DFT-based analysis of reaction pathways in electrocatalysis by providing a reference potential to the calculated free energies and circumventing the explicit treatment of solvated protons [31, 32]. However, the applicability of the CHE model is limited to modeling *concerted proton-electron transfer* (CPET) steps and cannot account for

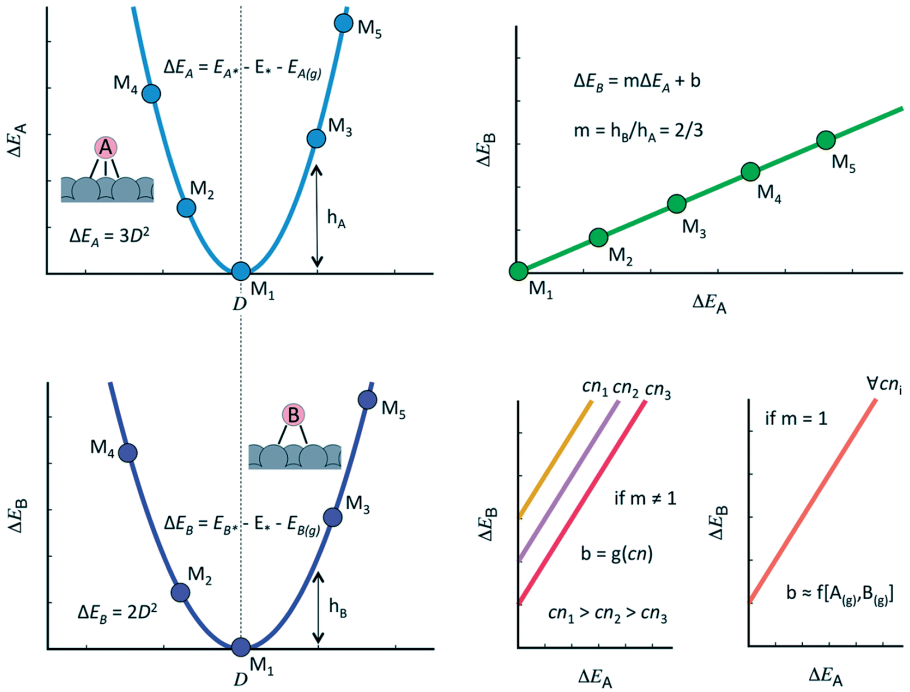

Figure 3.2: Illustration of adsorption energy scaling relationships. A and B are adsorbates and M_1 to M_5 are transition metal surfaces. ΔE_x stands for binding energy of the adsorbate x on the surface and is determined by the formulae indicated. D is a hypothetical electronic structure descriptor for the binding energy. The quadratic relationship between D and ΔE_x has been assumed for the sake of illustration. The slope of the scaling relationship (m) is given by the ratio of bonds made by the adsorbates with the surface. b is the intercept on the y-axis and is a function of the coordination number of the surface (cn) if m≠1. Figure reproduced from reference [1]. Published by The Royal Society of Chemistry.

decoupled transfer of electron and protons. Such decoupled elementary steps can be relevant for the eCO_2R mechanism and recent developments in computational methodologies aim to alleviate this shortcoming of the CHE model [33, 34].

Yet another aspect of the complexity of studying reaction processes on catalytic surfaces is the coverage of adsorbed species. Typical computational studies are performed with the assumption of low coverage (or

infinite dilution) and the derived energy values do not account for the population of surface bound species at steady-state. The coverage of the catalyst surface is a function of the catalyst properties, the applied potential and the reaction conditions. A high coverage can result in surface restructuring, inhibition or promotion of certain reaction steps and lateral adsorbate interactions. Taking surface coverage into consideration can, in some cases, become important for accurately modeling catalyst performance [35, 36].

Calculation of kinetic barriers of elementary electrocatalytic reaction steps in a physically consistent manner with the electrochemical interface can be challenging. The electrocatalyst is at a constant potential in a practical system and the reaction interface is characterized by the *electrical double layer* (EDL) and the presence of polarized water molecules that can participate in the reaction. Multiple methods have been developed to account for these factors in barrier calculations [14, 37–40]. The values of the kinetic barriers can be important to study the competition between the various possible reaction pathways that are thermodynamically feasible on a catalyst surface, especially for catalysts such as Cu with extended reaction schemes that can branch significantly (Figure 3.1). The kinetic barriers, if estimated accurately, can be fed into microkinetic models that take a mean-field approach to the catalyst surface. The estimated rate of production and consumption of reactive species in this manner can be compared with experimentally derived current densities to validate mechanistic studies [13, 41, 42]. Microkinetic models are also used within the scheme of multiscale modeling of electrocatalytic systems where they are integrated with atomistic electronic structure calculations and mass transport models [43]. However, like with any multiscale or multi-model approach, it becomes important to quantify the uncertainty in each model within the scheme to understand how the errors propagate over the entire scheme.

The chapter 4 attempts to answer some important open questions regarding the selectivity of Ag eCO_2R catalysts using *ab-initio* thermodynamic and kinetic barrier calculations. We include the effects of surface structure, solvation, water-shuttling of protons and lateral adsorbate interactions to understand why Ag catalysts produce CO and not $HCOO^-$ as a result of eCO_2R.

3.2. Reaction environment

Rather than simply a catalyst surface, the reaction in an electrocatalytic system such as eCO_2R occurs at the electrochemical interface. This interface is composed of the catalyst, which acts as the electron conductor, and an electrolyte solution, which acts as the ionic conductor as well as the medium of transport for the reactant molecules. The transfer of charge across this catalyst-electrolyte interface is the fundamental process of interest for eCO_2R. The electrolyte is typically an aqueous solution of alkali metal salts such as potassium bicarbonate ($KHCO_3$) [44, 45] and will be assumed to be the case in this thesis.

The applied potential on the cathode results in an accumulation of negative charge on the catalyst surface. The presence of the aqueous electrolyte facing the negatively charged catalyst surface results in the formation of an EDL composed of solvated ions that screen the surface charge. Additionally, the electric field at the interface results in a polarization of water molecules close to the catalyst surface. The reaction interface is a complex region with several coupled physical processes determining the catalyst reactivity. The water molecules, ions and the electric field at the interface influence the binding energy of reaction intermediates on the catalyst surface, the kinetic activation barriers for the elementary reaction steps and the transport of species towards and away from the surface [2, 41, 46–49]. In addition, the activity (concentration) of species at the interface will influence the rate of reactions and thus, the selectivity of the catalyst [49–52]. It is therefore essential to account for the interface and the resulting reaction environment in models for studying the catalytic reactivity, in addition to the catalyst surface itself.

3.2.1. Modeling the catalyst-electrolyte interface

Modeling the electrocatalytic interface accurately is the most challenging aspect of simulating eCO_2R. It requires the inclusion of the electrolyte, the electric field and the catalyst surface at a constant potential within the atomistic simulations for studying the thermodynamic and kinetic barriers for the reaction elementary steps. The EDL can be several nanometers thick and is composed of polarized water molecules and a high concentration of solvated ionic species. A complete atomistic model of such an interface can be prohibitively expensive computationally. For this rea-

son, *ab-initio* models have been used to simulate the effect of the different individual aspects of the catalyst-electrolyte interface such as the constant potential [14, 53], electric field [41, 46], solvent [10, 13, 20, 54], ions [41, 46, 55, 56] and pH [13, 57, 58].

There have also been attempts to model the interface using hybrid approaches in which the electrolyte is modeled using continuum models and solved self consistently with an *ab-initio* description of the catalysis [42, 43, 59, 60]. This has the advantage of reduced computational costs relative to models treating the electrolyte explicitly. However, coupling the continuum and atomistic models requires careful examination of the whether the continuum description is physically consistent with the nature of the interface at operating conditions [39]. The EDL can be a non-ideal region during eCO_2R with a high concentration of ionic species and a strong electric field such that coulombic forces, steric effects, van der Waals forces and ion specificity can become important factors. Additionally, inclusion of explicit water molecules can be important for accurate estimation of reaction barriers [39]. Development of accurate and computationally inexpensive models for the EDL will therefore play an important role in building better models for studying reactivity of catalyst-electrolyte interfaces.

In chapter 5, we use the continuum *generalized modified Poisson-Nernst-Planck* (GMPNP) system to model the reaction interface and study its influence on important parameters such as pH and CO_2 concentration. The GMPNP model includes the influence of electrostatic migration, buffer reaction kinetics, diffusion, heterogeneous reaction rates and volume exclusion to define the reaction environment at the catalyst electrolyte interface. We use our results to discuss the strengths as well as the weaknesses of such a continuum model and the essential role of the EDL in determining catalytic performance. The GMPNP model has been used recently in an atomistic-continuum multiscale scheme by Ringe *et al.* [60] to simulate eCO_2R on Au catalysts.

3.3. Mass transport

In addition to an optimal catalytic material and reaction interface, the rate of transport of CO_2 to the catalyst surface has been an important parameter for the design of a practically viable eCO_2R system. The need

to enhance CO_2 mass transport has led to development of *gas diffusion electrode* (GDE)-based systems as mentioned previously in section 2.4 and Figure 2.5 of chapter 2. GDE-based systems are typically characterized by gas-electrolyte interfaces where the gas phase is composed of concentrated CO_2. The catalyst layer is highly porous, with the gas-electrolyte interface in close proximity (order of ~100 nm) to the reaction interface. This implies that the CO_2 molecule has to travel orders of magnitude shorter distance in the electrolyte to reach the catalytic site relative to a case when solvated CO_2 is transported from the bulk saturated electrolyte in H-cells (diffusion length in the order of ~100 μm). Through better mass transport, GDE-based systems have achieved an order of magnitude higher rate of CO_2 conversion as well as higher product selectivity by manipulating the reaction environment [45, 61].

CO_2 reduction at practically relevant rates is accompanied by significant production and consumption rates of solution species due to the catalysis. These high concentration fluxes perturb the homogeneous buffer reactions and can lead to buffer break-down, bubble formation and heat generation within the electrolyte. Consequently, electrolyte flow, gas pressure and composition, flow patterns and associated pressure drops, and catalyst layer morphology are often important design aspects of eCO_2R systems with high conversion rates. Simulation of mass transport is thus yet another scale very relevant to engineer eCO_2R performance.

3.3.1. System-scale continuum models

Reaction-diffusion (RD) or, the *Nernst-Planck* (NP) model assuming electroneutrality, have been used extensively to simulate the transport of solution species in H-cell configurations [62–64]. The results from these simulations have been used to establish concentration overpotentials and transport limitations to the achievable current density. RD models have been adapted to account for features such as catalyst morphology [65, 66], bubble formation [67] and have also been integrated in multiscale schemes with DFT-parametrized microkinetic models [43]. However, due to the importance of the EDL in accurately describing the reaction interface, RD models have been extended to include electrostatic migration through the *Poisson-Nernst-Planck* (PNP) equations [47].

As mentioned in the previous section, chapter 5 extends the state-

of-the-art continuum transport models to include volume-exclusion and electrostatic migration to solve for practically relevant applied potentials. By modeling the EDL as a part of the species transport to and from the catalyst surface, the generalized modified PNP (GMPNP) model in chapter 5 forms a bridge between mass transport and reaction events at the catalyst surface.

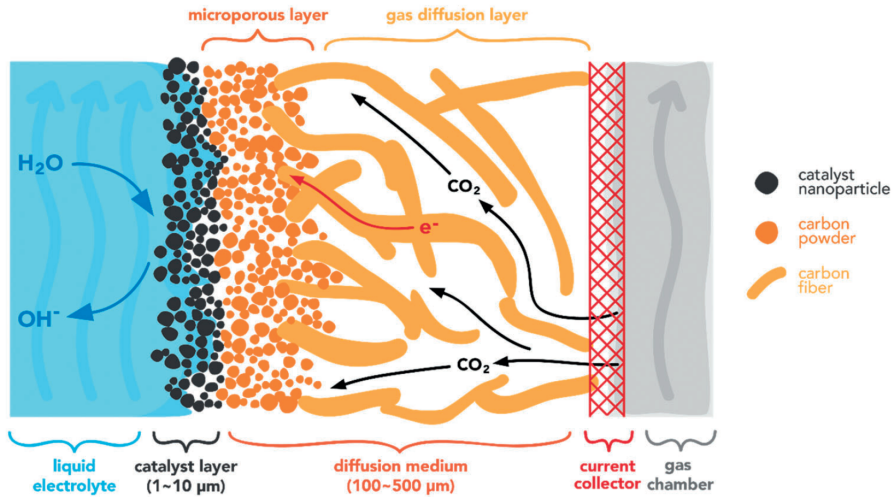

Figure 3.3: A schematic of a typical gas diffusion electrode-based flow cell configuration. Figure reproduced from reference [68] with permission from The Royal Society of Chemistry.

Modeling transport in GDE-based eCO_2R systems such as flow cells has become increasingly important due to the practical importance of these systems. Mass transport in flow cells is significantly more challenging relative to H-cell devices due to their complex system configuration (Figure 3.3). Recent attempts use one-dimensional models employing effective structural properties of the system to estimate mass transport profiles [68–70]. Chapter 6 uses the GMPNP equations to model the mass transport within a three-dimensional catalytic pore of a typical GDE flow cell. Our analysis demonstrates how the operating conditions and structural parameters of the device are highly influential in determining the mean reaction environment within the catalyst layer.

3.4. Concluding remarks

Simulations of eCO_2R span length and time scales ranging from the active catalytic site and molecular vibrations, to the macroscopic device and fluid flow rate. Simulating eCO_2R is therefore a major multiscale challenge and requires development of computational frameworks that accurately capture the system behavior at each scale in a computationally tractable manner. Although there has been extensive computational research done on the atomistic and continuum scale, molecular to mesoscale simulations are largely absent. Simulations at these intermediate scales can be fruitful to study the dynamics of the catalyst surface and the cooperative/competitive nature of reaction events. Molecular scale simulations can also be useful to study the structure and properties of the EDL. Modeling the EDL is an aspect of the electrocatalytic system which has received relatively less attention considering its importance.

Considering the variety of computational approaches deployed within the electrocatalysis community, benchmarking of simulation results and methodologies will be an essential step for a faster convergence towards predictive and accurate models in the future. Lastly, there are numerous system parameters that have been identified to potentially influence the overall system performance. However, there is little understanding still of the relative significance of these parameters for the observed experimental data. *Machine learning* (ML) and *uncertainty quantification* (UQ) techniques can play an important role in bridging the outputs of physical simulators with experimental data. This approach has the potential to systematically identify model deficiencies and improve predictability of physics-based simulators over practical systems.

References

[1] B. Garlyyev, J. Fichtner, O. Piqué, O. Schneider, A. S. Bandarenka, and F. Calle-Vallejo, *Revealing the nature of active sites in electrocatalysis,* Chem. Sci. **10**, 8060 (2019).

[2] J. K. Nørskov, F. Studt, F. Abild-Pedersen, and T. Bligaard, *Fundamental Concepts in Heterogeneous Catalysis* (John Wiley & Sons, Inc, Hoboken, NJ, USA, 2014) p. 208.

[3] M. T. M. Koper, *Structure sensitivity and nanoscale effects in electrocatalysis,* Nanoscale **3**, 2054 (2011).

[4] Y. Hori, H. Wakebe, T. Tsukamoto, and O. Koga, *Electrocatalytic process of CO selectivity in electrochemical reduction of CO_2 at metal electrodes in aqueous media,* Electrochimica Acta **39**, 1833 (1994).

[5] Y. Hori, R. Takahashi, Y. Yoshinami, and A. Murata, *Electrochemical reduction of CO at a copper electrode,* The Journal of Physical Chemistry B **101**, 7075 (1997).

[6] K. P. Kuhl, E. R. Cave, D. N. Abram, and T. F. Jaramillo, *New insights into the electrochemical reduction of carbon dioxide on metallic copper surfaces,* Energy & Environmental Science **5**, 7050 (2012).

[7] J. H. Montoya, C. Shi, K. Chan, and J. K. Nørskov, *Theoretical insights into a CO dimerization mechanism in CO_2 electroreduction,* The journal of physical chemistry letters **6**, 2032 (2015).

[8] A. A. Peterson, F. Abild-Pedersen, F. Studt, J. Rossmeisl, and J. K. Nørskov, *How copper catalyzes the electroreduction of carbon dioxide into hydrocarbon fuels,* Energy Environ. Sci. **3**, 1311 (2010).

[9] R. Kortlever, J. Shen, K. J. P. Schouten, F. Calle-Vallejo, and M. T. Koper, *Catalysts and reaction pathways for the electrochemical reduction of carbon dioxide,* Journal of Physical Chemistry Letters **6**, 4073 (2015).

[10] T. Cheng, H. Xiao, and W. A. Goddard III, *Free-energy barriers and reaction mechanisms for the electrochemical reduction of CO on the Cu (100) surface, including multiple layers of explicit solvent at pH 0,* The journal of physical chemistry letters **6**, 4767 (2015).

[11] Y. Lum, T. Cheng, W. A. Goddard III, and J. W. Ager, *Electrochemical CO reduction builds solvent water into oxygenate products,* Journal of the American Chemical Society **140**, 9337 (2018).

[12] J. T. Feaster, C. Shi, E. R. Cave, T. Hatsukade, D. N. Abram, K. P. Kuhl, C. Hahn, J. K. Nørskov, and T. F. Jaramillo, *Understanding selectivity for the electrochemical reduction of carbon dioxide to formic acid and carbon monoxide on metal electrodes,* Acs Catalysis **7**, 4822 (2017).

[13] X. Liu, P. Schlexer, J. Xiao, Y. Ji, L. Wang, R. B. Sandberg, M. Tang, K. S. Brown, H. Peng, S. Ringe, *et al.*, *pH effects on the electrochemical reduction of CO_2 towards C_2 products on stepped copper,* Nature communications **10**, 1 (2019).

[14] A. J. Garza, A. T. Bell, and M. Head-Gordon, *Mechanism of CO_2 reduction at copper surfaces: pathways to C_2 products,* ACS Catalysis **8**, 1490 (2018).

[15] I. V. Chernyshova, P. Somasundaran, and S. Ponnurangam, *On the origin of the elusive first intermediate of CO_2 electroreduction,* Proceedings of the National Academy of Sciences **115**, E9261 (2018).

[16] S. Nitopi, E. Bertheussen, S. B. Scott, X. Liu, A. K. Engstfeld, S. Horch, B. Seger, I. E. L. Stephens, K. Chan, C. Hahn, J. K. NÃžrskov, T. F. Jaramillo, and I. Chorkendorff, *Progress and perspectives of electrochemical CO_2 reduction on copper in aqueous electrolyte,* Chemical Reviews **119**, 7610 (2019).

[17] Y. Hori, *Electrochemical CO_2 reduction on metal electrodes,* in *Modern Aspects of Electrochemistry*, edited by C. G. Vayenas, R. E. White, and M. E. Gamboa-Aldeco (Springer New York, New York, NY, 2008) pp. 89–189.

[18] G. O. Larrazábal, A. J. Martín, and J. Pérez-Ramírez, *Building blocks for high performance in electrocatalytic CO_2 reduction: Materials, optimization strategies, and device engineering,* The Journal of Physical Chemistry Letters **8**, 3933 (2017).

[19] Y. Y. Birdja, E. Pérez-Gallent, M. C. Figueiredo, A. J. Göttle, F. Calle-Vallejo, and M. T. Koper, *Advances and challenges in understanding the electrocatalytic conversion of carbon dioxide to fuels,* Nature Energy **4**, 732 (2019).

[20] T. Cheng, H. Xiao, and W. A. Goddard, *Full atomistic reaction mechanism with kinetics for CO reduction on Cu(100) from ab initio molecular dynamics free-energy calculations at 298 K,* Proceedings of the National Academy of Sciences **114**, 1795 (2017).

[21] W. Luo, X. Nie, M. J. Janik, and A. Asthagiri, *Facet dependence of co2 reduction paths on cu electrodes,* ACS Catalysis **6**, 219 (2016).

[22] F. Calle-Vallejo, J. I. Martínez, J. M. García-Lastra, P. Sautet, and D. Loffreda, *Fast prediction of adsorption properties for platinum nanocatalysts with generalized coordination numbers,* Angewandte Chemie International Edition **53**, 8316 (2014).

[23] J. K. Nørskov, T. Bligaard, J. Rossmeisl, and C. H. Christensen, *Towards the computational design of solid catalysts, Nature Chemistry*, **1**, 37 (2009).

[24] F. Calle-Vallejo and M. T. M. Koper, *First-principles computational electrochemistry: Achievements and challenges,* Electrochimica Acta **84**, 3 (2012).

[25] M. T. Tang, Z. W. Ulissi, and K. Chan, *Theoretical investigations of transition metal surface energies under lattice strain and CO environment,* The Journal of Physical Chemistry C **122**, 14481 (2018).

[26] H. Matsushima, A. Taranovskyy, C. Haak, Y. Grunder, and O. M. Magnussen, *Reconstruction of Cu (100) electrode surfaces during hydrogen evolution,* Journal of the American Chemical Society **131**, 10362 (2009).

[27] F. Abild-Pedersen, J. Greeley, F. Studt, J. Rossmeisl, T. R. Munter, P. G. Moses, E. Skúlason, T. Bligaard, and J. K. Nørskov, *Scaling properties of adsorption energies for hydrogen-containing molecules on transition-metal surfaces,* Phys. Rev. Lett. **99**, 016105 (2007).

[28] F. Calle-Vallejo, D. Loffreda, M. T. Koper, and P. Sautet, *Introducing structural sensitivity into adsorption-energy scaling relations by means of coordination numbers,* Nature chemistry **7**, 403 (2015).

[29] N. Govindarajan, M. T. M. Koper, E. J. Meijer, and F. Calle-Vallejo, *Outlining the scaling-based and scaling-free optimization of electrocatalysts,* ACS Catalysis **9**, 4218 (2019).

[30] A. A. Peterson and J. K. Nørskov, *Activity descriptors for CO_2 electroreduction to methane on transition-metal catalysts,* The Journal of Physical Chemistry Letters **3**, 251 (2012).

[31] A. A. Peterson, F. Abild-Pedersen, F. Studt, J. Rossmeisl, and J. K. Nørskov, *How copper catalyzes the electroreduction of carbon diox-*

ide into hydrocarbon fuels, Energy & Environmental Science **3**, 1311 (2010).

[32] J. K. Nørskov, J. Rossmeisl, A. Logadottir, L. Lindqvist, J. R. Kitchin, T. Bligaard, and H. Jonsson, *Origin of the overpotential for oxygen reduction at a fuel-cell cathode,* The Journal of Physical Chemistry B **108**, 17886 (2004).

[33] M. T. M. Koper, *Theory of multiple proton-electron transfer reactions and its implications for electrocatalysis,* Chem. Sci. **4**, 2710 (2013).

[34] A. J. Göttle and M. T. Koper, *Proton-coupled electron transfer in the electrocatalysis of CO_2 reduction: prediction of sequential vs. concerted pathways using DFT,* Chemical science **8**, 458 (2017).

[35] A. C. Lausche, A. J. Medford, T. S. Khan, Y. Xu, T. Bligaard, F. Abild-Pedersen, J. K. Nørskov, and F. Studt, *On the effect of coverage-dependent adsorbate–adsorbate interactions for CO methanation on transition metal surfaces,* Journal of catalysis **307**, 275 (2013).

[36] Y. Hori, A. Murata, and Y. Yoshinami, *Adsorption of CO, intermediately formed in electrochemical reduction of CO_2, at a copper electrode,* Journal of the Chemical Society, Faraday Transactions **87**, 125 (1991).

[37] K. Chan and J. K. Nørskov, *Electrochemical barriers made simple,* The journal of physical chemistry letters **6**, 2663 (2015).

[38] J. Hussain, H. Jonsson, and E. Skulason, *Calculations of product selectivity in electrochemical CO_2 reduction,* ACS Catalysis **8**, 5240 (2018).

[39] J. A. Gauthier, S. Ringe, C. F. Dickens, A. J. Garza, A. T. Bell, M. Head-Gordon, J. K. Nørskov, and K. Chan, *Challenges in modeling electrochemical reaction energetics with polarizable continuum models,* Acs Catalysis **9**, 920 (2018).

[40] S. A. Akhade, N. J. Bernstein, M. R. Esopi, M. J. Regula, and M. J. Janik, *A simple method to approximate electrode potential-dependent activation energies using density functional theory,* Catalysis Today **288**, 63 (2017).

[41] L. D. Chen, M. Urushihara, K. Chan, and J. K. Nørskov, *Electric field effects in electrochemical CO_2 reduction,* ACS Catalysis **6**, 7133 (2016).

[42] J. D. Goodpaster, A. T. Bell, and M. Head-Gordon, *Identification of possible pathways for C−C bond formation during electrochemical reduction of CO_2: new theoretical insights from an improved electrochemical model,* The journal of physical chemistry letters **7**, 1471 (2016).

[43] M. R. Singh, J. D. Goodpaster, A. Z. Weber, M. Head-Gordon, and A. T. Bell, *Mechanistic insights into electrochemical reduction of CO_2 over Ag using density functional theory and transport models,* Proceedings of the National Academy of Sciences **114**, E8812 (2017).

[44] J.-P. Jones, G. K. S. Prakash, and G. A. Olah, *Electrochemical CO_2 reduction: Recent advances and current trends,* Israel Journal of Chemistry **54**, 1451 (2014), https://onlinelibrary.wiley.com/doi/pdf/10.1002/ijch.201400081 .

[45] S. Garg, M. Li, A. Z. Weber, L. Ge, L. Li, V. Rudolph, G. Wang, and T. E. Rufford, *Advances and challenges in electrochemical CO_2 reduction processes: an engineering and design perspective looking beyond new catalyst materials,* J. Mater. Chem. A **8**, 1511 (2020).

[46] J. Resasco, L. D. Chen, E. Clark, C. Tsai, C. Hahn, T. F. Jaramillo, K. Chan, and A. T. Bell, *Promoter effects of alkali metal cations on the electrochemical reduction of carbon dioxide,* Journal of the American Chemical Society **139**, 11277 (2017), pMID: 28738673.

[47] M. Liu, Y. Pang, B. Zhang, P. De Luna, O. Voznyy, J. Xu, X. Zheng, C. T. Dinh, F. Fan, C. Cao, F. P. G. de Arquer, T. S. Safaei, A. Mepham, A. Klinkova, E. Kumacheva, T. Filleter, D. Sinton, S. O. Kelley, and E. H. Sargent, *Enhanced electrocatalytic CO_2 reduction via field-induced reagent concentration,* Nature **537**, 382 EP (2016).

[48] C. M. Gunathunge, V. J. Ovalle, and M. M. Waegele, *Probing promoting effects of alkali cations on the reduction of CO at the aqueous electrolyte/copper interface,* Phys. Chem. Chem. Phys. **19**, 30166 (2017).

[49] Y. Hori, A. Murata, and R. Takahashi, *Formation of hydrocarbons in the electrochemical reduction of carbon dioxide at a copper electrode in aqueous solution,* J. Chem. Soc., Faraday Trans. 1 **85**, 2309 (1989).

[50] A. S. Varela, M. Kroschel, T. Reier, and P. Strasser, *Controlling the selectivity of CO_2 electroreduction on copper: The effect of the electrolyte concentration and the importance of the local pH,* Catalysis Today **260**, 8 (2016), surface Analysis and Dynamics (SAND).

[51] R. Kas, R. Kortlever, H. Yilmaz, M. T. M. Koper, and G. Mul, *Manipulating the hydrocarbon selectivity of copper nanoparticles in CO_2 electroreduction by process conditions,* ChemElectroChem **2**, 354 (2015).

[52] M. Ma, K. Djanashvili, and W. A. Smith, *Controllable hydrocarbon formation from the electrochemical reduction of CO_2 over Cu nanowire arrays,* Angewandte Chemie International Edition **55**, 6680 (2016).

[53] K. Chan and J. K. Nørskov, *Potential dependence of electrochemical barriers from ab initio calculations,* The Journal of Physical Chemistry Letters **7**, 1686 (2016).

[54] X. Nie, M. R. Esopi, M. J. Janik, and A. Asthagiri, *Selectivity of CO_2 reduction on copper electrodes: the role of the kinetics of elementary steps,* Angewandte Chemie **125**, 2519 (2013).

[55] E. Perez-Gallent, G. Marcandalli, M. C. Figueiredo, F. Calle-Vallejo, and M. T. Koper, *Structure-and potential-dependent cation effects on CO reduction at copper single-crystal electrodes,* Journal of the American Chemical Society **139**, 16412 (2017).

[56] S. A. Akhade, I. T. McCrum, and M. J. Janik, *The impact of specifically adsorbed ions on the copper-catalyzed electroreduction of CO_2,* Journal of The Electrochemical Society **163**, F477 (2016).

[57] M. R. Singh, E. L. Clark, and A. T. Bell, *Effects of electrolyte, catalyst, and membrane composition and operating conditions on the performance of solar-driven electrochemical reduction of carbon dioxide,* Physical Chemistry Chemical Physics **17**, 18924 (2015).

[58] H. Xiao, T. Cheng, W. A. Goddard III, and R. Sundararaman, *Mechanistic explanation of the pH dependence and onset potentials for hydrocarbon products from electrochemical reduction of CO on Cu (111),* Journal of the American Chemical Society **138**, 483 (2016).

[59] S. E. Weitzner, S. A. Akhade, J. B. Varley, B. C. Wood, M. Otani, S. E. Baker, and E. B. Duoss, *Toward engineering of solution microenvironments for the CO_2 reduction reaction: Unraveling pH and voltage effects from a combined density-functional-continuum theory,* The Journal of Physical Chemistry Letters **11**, 4113 (2020).

[60] S. Ringe, C. G. Morales-Guio, L. D. Chen, M. Fields, T. F. Jaramillo, C. Hahn, and K. Chan, *Double layer charging driven carbon dioxide adsorption limits the rate of electrochemical carbon dioxide reduction on gold,* Nature Communications **11**, 1 (2020).

[61] D. Higgins, C. Hahn, C. Xiang, T. F. Jaramillo, and A. Z. Weber, *Gas-diffusion electrodes for carbon dioxide reduction: A new paradigm,* ACS Energy Letters **4**, 317 (2019).

[62] N. Gupta, M. Gattrell, and B. MacDougall, *Calculation for the cathode surface concentrations in the electrochemical reduction of CO_2 in $KHCO_3$ solutions,* Journal of Applied Electrochemistry **36**, 161 (2006).

[63] C. Delacourt, P. L. Ridgway, and J. Newman, *Mathematical modeling of CO_2 reduction to CO in aqueous electrolytes i. Kinetic study on planar silver and gold electrodes,* J. Electrochem. Soc. **157**, B1902 (2010).

[64] H. Hashiba, L.-C. Weng, Y. Chen, H. K. Sato, S. Yotsuhashi, C. Xiang, and A. Z. Weber, *Effects of electrolyte buffer capacity on surface reactant species and the reaction rate of CO_2 in electrochemical CO_2 reduction,* The Journal of Physical Chemistry C **122**, 3719 (2018).

[65] D. Raciti, M. Mao, and C. Wang, *Mass transport modelling for the electroreduction of CO_2 on Cu nanowires,* Nanotechnology **29**, 044001 (2018).

[66] S. Suter and S. Haussener, *Optimizing mesostructured silver catalysts for selective carbon dioxide conversion into fuels,* Energy Environ. Sci. **12**, 1668 (2019).

[67] T. Burdyny, P. J. Graham, Y. Pang, C.-T. Dinh, M. Liu, E. H. Sargent, and D. Sinton, *Nanomorphology-enhanced gas-evolution intensifies CO_2 reduction electrochemistry,* ACS Sustainable Chemistry & Engineering **5**, 4031 (2017).

[68] L.-C. Weng, A. T. Bell, and A. Z. Weber, *Modeling gas-diffusion electrodes for CO_2 reduction,* Phys. Chem. Chem. Phys. **20**, 16973 (2018).

[69] K. Wu, E. Birgersson, B. Kim, P. J. Kenis, and I. A. Karimi, *Modeling and experimental validation of electrochemical reduction of CO_2 to CO in a microfluidic cell,* Journal of The Electrochemical Society **162**, F23 (2015).

[70] C.-T. Dinh, T. Burdyny, M. G. Kibria, A. Seifitokaldani, C. M. Gabardo, F. P. G. De Arquer, A. Kiani, J. P. Edwards, P. De Luna, O. S. Bushuyev, *et al.*, *CO_2 electroreduction to ethylene via hydroxide-mediated copper catalysis at an abrupt interface,* Science **360**, 783 (2018).

4

The competition between two-electron reduction products

Elucidating the pathways involved in the electrochemical reduction of carbon dioxide (eCO_2R) is crucial for the advancement of sustainable chemical and fuel manufacturing processes. Ag is an appealing eCO_2R catalyst due to its promising performance for carbon monoxide (CO) production and relatively low cost. In this chapter, we study the role of the formate ($HCOO^-$) intermediate $*OCHO$, aiming to resolve the discrepancy between the current theoretical understanding and experimental performance of Ag catalysts. We demonstrate that the first coupled proton-electron transfer (CPET) step in the pathway for CO production to form $*COOH$ competes with the Volmer step for formation of $*H$, whereas this Volmer step is a prerequisite for the formation of the $*OCHO$ species. We show that $*OCHO$ should form readily on the Ag surface owing to substantial stabilization of the transition state due to solvation and favorable binding strength. In addition, we use in-situ surface-enhanced Raman spectroscopy (SERS) experiments to provide preliminary evidence of the presence of O-bound bidentate species on polycrystalline Ag catalyst during eCO_2R at low overpotentials which we attribute to $*OCHO$. Lateral adsorbate-adsorbate interactions in the presence of $*OCHO$ have a significant influence on the surface coverage of $*H$, resulting in the inhibition of $HCOO^-$ and H_2 production and a higher selectivity towards CO. We argue that the species $*OCHO$ plays an important role in determining the activity and selectivity for not only formate-producing catalysts but also

for catalysts such as Ag that predominantly produce CO.

This chapter has been published in Angew. Chem. Int. Ed. **58**, 1345 (2019) [1].

Computational research work led by Divya Bohra and supervised by Guanna Li and Evgeny A. Pidko; Experimental research work led by Isis Ledezma-Yanez and supervised by Wiebren de Jong; Wilson A. Smith supervised the project as the principal investigator.

4.1. Introduction

The electrochemical reduction of CO_2 is a very promising approach providing a means to manage intermittent renewable electricity production by converting it to a chemically valuable form, while recycling climate change-inducing CO_2 [2–6]. Understanding the pathways for the (electro)chemical transformations involved in eCO_2R is critical to advance its technological utilization. The 2 proton-electron transfer products of eCO_2R, namely CO and $HCOO^-$ are highly attractive due to relatively low overpotentials needed to drive their production, and high achievable Faradaic efficiencies [7–12]. The need to balance the performance with low cost electrodes has led to an increased interest in using Ag as a CO_2 reduction catalyst, which has a high selectivity to CO while being 100 times cheaper than the alternative Au. [12–19].

It is widely accepted that the formation of CO from CO_2 on transition metal catalysts with an aqueous electrolyte proceeds via the $*$COOH species, whereas the formation of $HCOO^-$ proceeds via the bidentate O-bound $*$OCHO species, both forming after a single CPET step [13, 20–24]. Figure A.12 in the Appendix shows a comparison between the adsorption energy of intermediates for CO and $HCOO^-$ formation pathways for (111), (211) and (110) Ag surfaces. Limiting potentials (U_L) in all free energy plots are given vs. RHE and are defined as the minimum potential at which all reaction steps of a pathway are exergonic. As found experimentally [25], (110) is the most active surface for formation of CO due to higher binding strength of $*$COOH leading to a lower U_L. The opposite is true for formation of $HCOO^-$ for which the (111) surface has the least U_L due to lower binding strength of $*$OCHO. This implies that as the surface becomes more open and uncoordinated such as for (110), the relative U_L for formation of CO and $HCOO^-$ are closer to each other whereas formation of $HCOO^-$ has a drastically lower U_L relative to CO for close-packed surfaces such as (111). The surface structure of the catalyst is therefore expected to play an important role in determining selectivity between the eCO_2R products on Ag.

Ag(110) is used as the model surface for this chapter due to its high activity for the selective production of CO. In addition to $*$COOH as a precursor to CO, we also consider the free energy of formation of $*$CO+$*$OH by the breaking of the C−O bond as an alternative. However, we find

that the limiting potential (U_L) for this step (green pathway in Figure 4.1) is significantly higher than for the pathway via ∗COOH (red pathway in Figure 4.1).

Consideration of the relative limiting potentials (U_L) alone dictates that the formation of H_2 is most thermodynamically feasible on Ag(110), followed by $HCOO^-$ and then CO as depicted in the free energy plot in Figure 4.1. Interestingly, this conclusion does not reconcile with the experimental observations of the formation of CO as the major product of eCO_2R on Ag, H_2 as a by-product (through the hydrogen evolution reaction, HER), with the detection of only trace amounts of $HCOO^-$ for intermediate applied potentials of ca. -0.9 V to -1.3 V [13]. For applied potentials more or less negative of this range, the Faradaic efficiency for H_2 dominates that for CO. However, irrespective of the applied potential, the experimentally observed Faradaic efficiency for the formation of $HCOO^-$ remains significantly lower (<10%) relative to CO and H_2. The reasons for this discrepancy and the role of the stable species ∗OCHO in the catalytic performance of Ag is not well understood.

Here we report our findings of the mechanistic differences in the formation of ∗OCHO and ∗COOH and their respective interactions with the H_2 production pathways on an Ag(110) surface. We show that there are two major bifurcations in the reaction mechanism before and after formation of ∗H that control the selectivity between CO, $HCOO^-$ and H_2. We present reaction barrier calculations to show that the formation of ∗OCHO has a significantly lower kinetic barrier relative to ∗COOH on Ag(110) and that solvation of the transition state by the surrounding water molecules plays an important role in determining this barrier. Finally, we demonstrate that the influence of lateral adsorbate-adsorbate interactions resulting from the presence of ∗OCHO on the surface promotes CO production while inhibiting itself and the formation of $HCOO^-$ as a consequence.

4.2. Computational Details

A 3x3x4 slab size was used for Ag(111) and Ag(211) and a 2x3x6 slab size was used for Ag(110). Intermediate adsorption energies were calculated for all high symmetry binding sites on each surface and the binding energy found to be most favorable was used in the final plots. The Ag

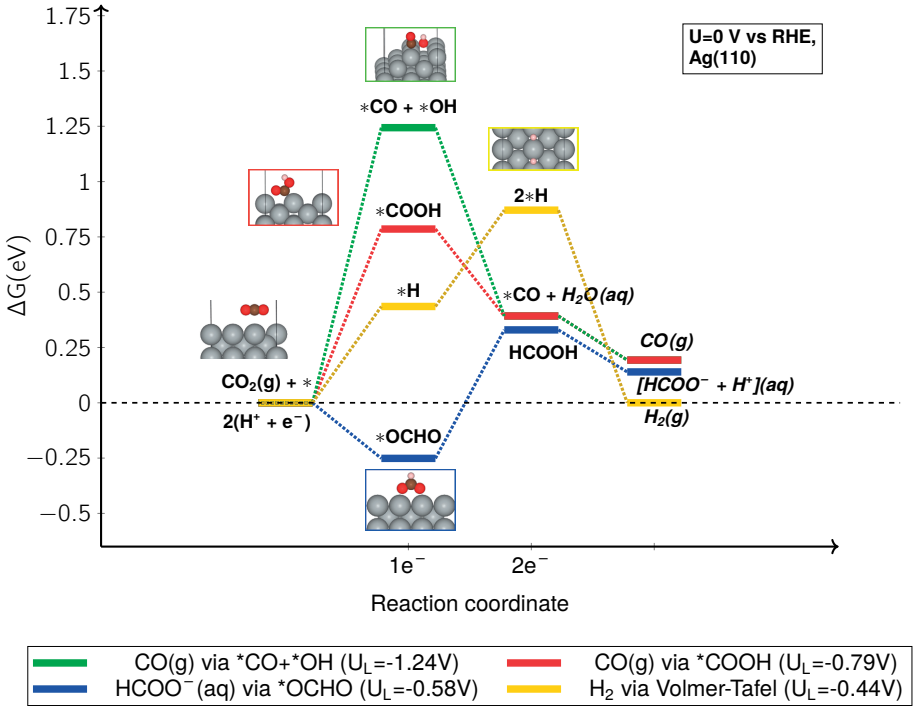

Figure 4.1: Free energy diagram after correcting for solvation of 2 electron transfer reactions on an Ag(110) surface at 0 V vs. the reversible hydrogen electrode (RHE). Limiting potentials (U_L) in the legend are given vs. RHE.

metal slab and surfaces with and without adsorbed intermediates were created using the Atomic Simulation Environment (ASE) [26]. All density functional theory (DFT) calculations were carried out with the projector augmented wave (PAW) method as implemented in the GPAW software [27, 28]. BEEF-vdW exchange correlation (xc) functional was used to perform all the energy calculations [29, 30] with plane-wave (PW) cutoff energy value of 450 eV. Lattice constant for the bulk FCC metal were calculated using the same xc functional and PW cutoff for a residual force on all atoms of less than 0.005 eV $Å^{-1}$. The resulting lattice constant for Ag, 4.1384 Å, was used for all other energy calculations.

For the geometry optimization of the bare and intermediate adsorbed Ag slab, the top two metal layers as well as the adsorbed atoms were allowed to relax until a residual force of less than 0.01 eV $Å^{-1}$ is reached. The self-consistent field (SCF) convergence criterion was set to 5 x 10^{-4} eV for adsorption energy calculations. A 12 Å vacuum layer was placed above the periodically repeating slabs. The Fermi-Dirac method was used to smear the Fermi level with an electronic temperature of 0.1 eV and a Pulay mixing of the resulting electronic density was applied. A (3x3x1) k-point sampling was used and a grid spacing between 0.16 Å and 0.2 Å was used for all calculations. Barrier energy calculations were performed using climbing image nudged elastic band (CI-NEB) method [31] for which the SCF criterion of 1 x 10^{-5} eV and a maximum residual force of 0.05 eV $Å^{-1}$ was used. Bader charge analysis has been performed using the code developed by the Henkelman group [32–35].

Vibrational analysis was performed at room temperature (298.15 K) using the harmonic approximation followed by a statistical mechanical treatment to calculate ensemble energies from single molecule energies [36]. The equation (4.1) provides the expression for obtaining free energy of a slab with adsorbed molecule X (denoted as $*X$). The energies obtained using DFT (E^{DFT}) are corrected in this way for zero point vibrational energy (E^{ZPVE}), enthalpy ($\int_{T=0}^{T} C_p dT$) and vibrational entropy (TS^{vib}). E_{xc} signifies the systematic errors associated with the xc functional BEEF-vdW [37] and E_{solv} indicates the solvation correction due to presence of water. The general expression (4.2) gives the free energies of adsorption (ΔG_{ads}) of intermediate $*X$. E_{xc} for BEEF-vdW was taken as 0.33 eV for the CO_2 and HCOOH molecules and 0.09 eV for the H_2 molecule [38]. Fugacities of the non-adsorbed species have been adapted from Chan *et al.*

[37]. The free energy of deprotonation of HCOOH(aq) is calculated as -0.19 eV according to the equation (4.3) assuming a formate concentration of 0.01 M, pK_a of 3.79 and a pH of 6.8 [39].

$$* + X(g) \rightarrow *X$$

$$G_{*X} = E_{*X}^{DFT} + E_{*X}^{ZPVE} + \int_{T=0}^{T} C_{p*X} dT - TS_{*X}^{vib} - E_{solv} + E_{xc} \quad (4.1)$$

$$\Delta G_{*X}^{ads} = G_{*X} - G_{slab} - G_{X(g)} \quad (4.2)$$

$$\Delta G_{HCOOH}^{deprot} = k_B T\{ln(10) * (pK_a - pH) + ln[HCOO^-]\} \quad (4.3)$$

E_{solv} for adsorbed species has been calculated using implicit solvation model VASPSol [40, 41] implemented in Vienna Ab Initio Simulation Package (VASP) [42, 43] with a dielectric constant of 80 for water. These corrections have been performed for intermediate as well transition state species. The table A.1 in the Appendix provides the solvation energy correction for all the species considered in this study. The free energies used for all Figures in this chapter have been corrected for solvation unless stated otherwise. Vibrational and solvation corrections have been calculated for initial, final and transition states including the participating 2 explicit water molecules in order to plot the reaction free energy barriers where applicable.

Vibrational analysis is also essential to confirm whether the structure obtained as a result of a geometry optimization is a minima (intermediate state (IS)) or a first-order saddle point (transition state (TS)). This can be concluded by diagonalizing the Hessian matrix whose eigen values give the force constants for all vibrational modes of the molecule. All positive eigen values confirm an IS whereas a single negative eigen value along the reaction coordinate signifies a TS. This check was done for all intermediates as well as transition state species obtained using CI-NEB calculations.

All proton and electron transfers were assumed to be coupled (CPET) and the computational hydrogen electrode (CHE) model was used to obtain free energy change for an elementary step involving CPET [44]. The CHE model takes advantage of the equivalence of free energy of an electron and proton pair and hydrogen gas at standard conditions (equation (4.5)). 0 V is defined vs RHE at which the reaction (4.4) is at equilibrium (at all pH, all temperatures and $H_2(g)$ pressure of 101325 Pa). The ΔG as a function of electrode potential U for a CPET step is then given by an expression such as (4.6).

$$\mathrm{H^+_{bulk}} + \mathrm{e^-_{catalyst}} \rightleftharpoons \mathrm{H_2(g)} \tag{4.4}$$

$$\mu(H^+) + \mu(e^-) = \frac{1}{2}\mu(H_{2(g)}) - eU \tag{4.5}$$

$$*X + H^+_{(aq)} + e^- \rightarrow *XH$$

$$\Delta G(U) = G_{*XH} - G_{*X} - (\frac{1}{2}G_{H_2} - eU) \tag{4.6}$$

Analogous to the CHE model for calculation of adsorption free energies, the CI-NEB calculations have been performed assuming equilibrium between the bulk protons and surface adsorbed H (reaction (4.7)). This approach proposed recently by Akhade *et al.* [45] has the advantage of using the bulk electrolyte as a reference state against which the reaction barriers are estimated instead of an arbitrary chemical potential of protons in a simulation cell. Also, the initial state of $*$H is a stable local minima on the potential energy surface leading to a well defined reaction path. The activation barrier calculated is thus at the potential U^o at which reaction (4.7) is at equilibrium, which in our case is -0.435 V vs. RHE as can be inferred from Figure 4.1. For the reaction steps considered in this study, the change in work function of catalyst surface between the reactant, transition and final state can be considered negligible [45].

$$\mathrm{H^+_{bulk}} + \mathrm{e^-_{catalyst}} + * \rightleftharpoons *\mathrm{H} \tag{4.7}$$

Since the initial states of all reaction steps consist of a surface bound $*$H ($\mathrm{H}^{\delta-}$), reactions requiring a $\mathrm{H}^{\delta+}$ have been modeled using two additional

water molecules close to the surface. The ∗H hops through the two water molecules via a Grotthuss type mechanism forming $H_5O_2^+$ to eventually interact with the other reacting species such as another ∗H or a CO_2 close to the surface. Additional solvation might affect the energy of the reacting species which is why the energies of the initial, transition and final states have been corrected using implicit solvation model as described previously. The structure of the transition states located using this approach were checked to insure that the saddle points correspond to the formation of the respective final states (FS) and not for oxidation of ∗H by water. This check is important for steps where the ∗H first gets solvated by water before participating in the reaction of interest such as in the case of ∗COOH and H_2 via Heyrovsky step implying that the saddle point can be reached without forming ∗H initially.

Adsorbate-adsorbate interactions have been calculated on a 2x3x6 Ag (110) surface with the initial configuration of all the species present on their most favorable surface sites respectively (short-bridge for ∗H, 2 on-top sites across long-bridge for ∗COOH with the C and one of the O atoms bound to the surface, and 2 on-top sites across the short-bridge for ∗OCHO with both the Os bound to the surface). This is followed by geometrical optimization with the same convergence criteria as described previously. Coverage value of a surface species corresponds to the fraction of the number of sites occupied and the total number of surface atoms. For e.g.: one ∗H on a short-bridge site has a coverage of $\frac{1}{6}$ whereas one ∗OCHO or COOH has a coverage of $\frac{1}{3}$.

The experimental methods used for the surface-enhanced Raman spectroscopy (SERS) results can be found in the Appendix in section A.1.

4.3. Results and discussion

4.3.1. Mechanistic differences in eCO$_2$R pathways

The lowest unoccupied molecular orbital (LUMO) of a bent CO_2 is highly localized at the C, whereas the highest occupied molecular orbital (HOMO) is highly localized at the O, making them strongly susceptible to interactions with nucleophiles and electrophiles respectively [20]. We use Bader charge analysis [35, 46] to quantify this susceptibility and to chart the reaction path for the first CPET step for CO_2 reduction, as depicted in

Figure 4.2. In order for the C−H bond of ∗OCHO to form, ∗H with a partial negative charge (δ^-) acts as a nucleophile for the $C^{\delta+}$ of CO_2 (top panel in Figure 4.2). Both Volmer-Tafel and Volmer-Heyrovsky mechanisms for the formation of H_2 also share the first CPET Volmer step of $*H^{\delta-}$ formation (bottom panel in Figure 4.2). This implies that the formation of ∗COOH competes with the Volmer step which is in-turn a prerequisite for the formation of ∗OCHO. Following the Volmer step, the ∗H can either participate in a Tafel or Heyrovsky step to form H_2, or react with the CO_2 to form ∗OCHO. According to our analysis, there are therefore two reaction bifurcations before and after formation of ∗H that generally control the selectivity for eCO_2R. An analogous finding has been recently reported for eCO_2R on Cu(100) surfaces [47] and as well as for the selectivity of eCO_2R on metalloporphyrins [48].

This approach can be further extended to the formation of higher CPET products from eCO_2R such as methanol (CH_3OH) and methane (CH_4). Figure A.13 in the Appendix shows the proposed general reaction network for CO_2 electro-reduction for formation of C1 species. C2 and higher species have been ignored in this network since the focus of this study is Ag electrodes, which show high selectivity for C1 products and hydrogen, and thus no appreciable amount of C2 products are expected to form [49, 50]. This scheme has been generated from the reaction networks reported in literature [24, 49] in addition to a general chemical intuition. Figures 4.3 and 4.4 show the free energy plots for the formation of CH_3OH and CH_4 in accordance with the reaction scheme of Figure A.13. The thermodynamically most feasible routes for the formation of CH_3OH and CH_4 go via ∗COOH followed by the ∗CHO species, as becomes clear from the U_L for the various reaction pathways shown in Figures 4.3 and 4.4. Extending the Bader charge analysis to these pathways, it is expected that the formation of ∗CHO from ∗CO forms through a surface bound ∗H interacting with the $C^{\delta+}$. θ_{*H} is therefore expected to play an important role in the formation of higher electron reduction products of eCO_2R and this analysis can potentially be useful for studying catalysts such as Cu where these reaction steps become prominent. Interestingly, very recent experimental findings for eCO_2R on Cu catalysts draw similar conclusions and indicate an important role of ∗H in the formation of CH_4 [51, 52].

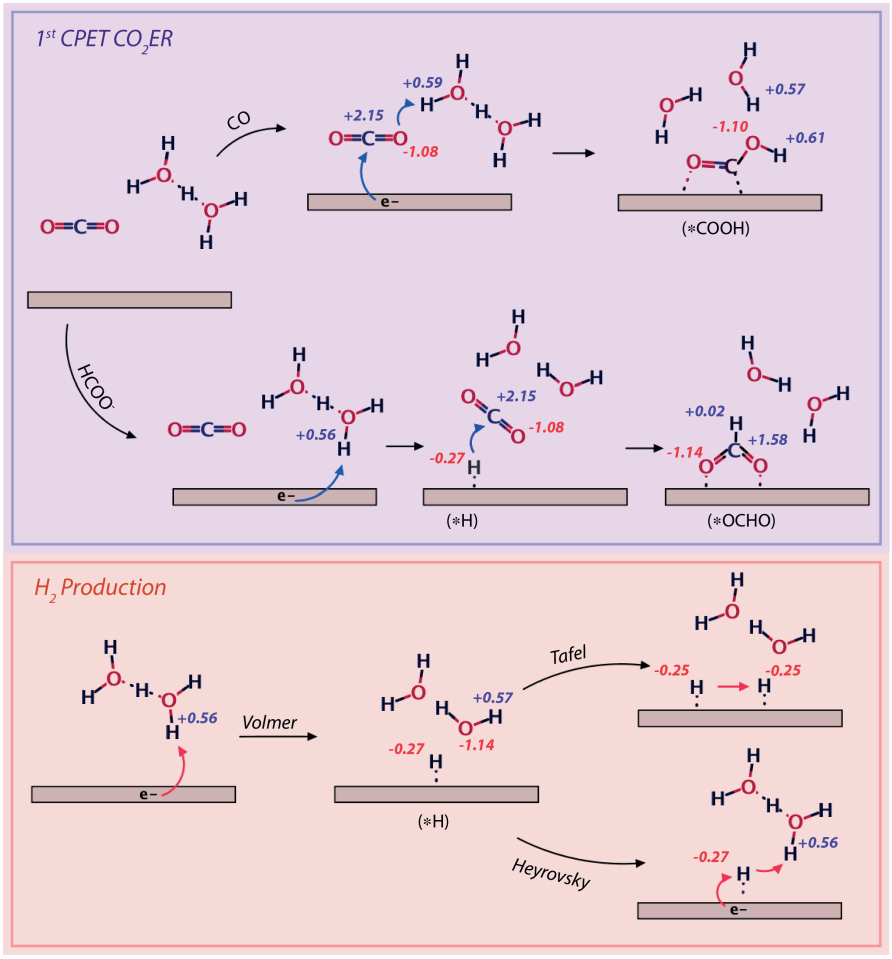

Figure 4.2: A cartoon depicting the first reduction step for eCO_2R pathways to form $*COOH$ (CO pathway) and $*OCHO$ ($HCOO^-$ pathway) on an Ag(110) surface (violet box above) along with the two H_2 formation pathways: Volmer-Tafel and Volmer-Heyrovsky (peach box below). The excess partial charges for the relevant chemical species is mentioned in blue for a excess positive charge and in red for excess negative charge.

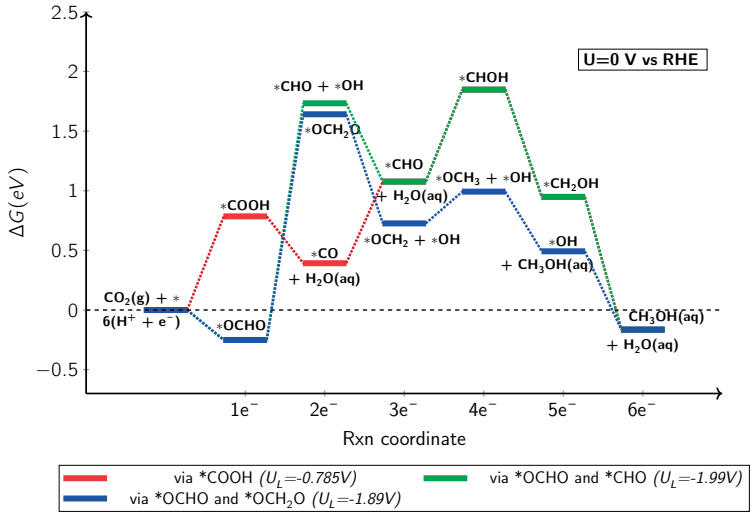

Figure 4.3: Free energy diagram showing pathways for formation of CH_3OH(aq) for Ag(110) surface. The limiting potentials (U_L) in the legend for all the pathways are vs. RHE.

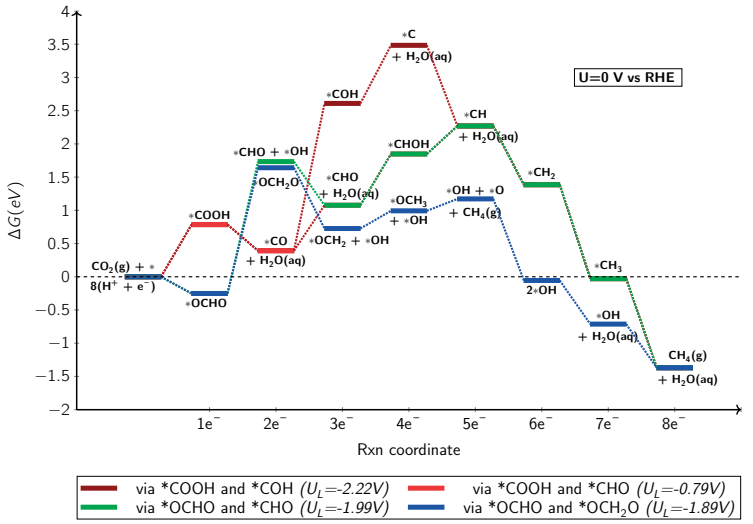

Figure 4.4: Free energy diagram showing pathways for formation of CH_4(g) for Ag(110) surface. The limiting potentials (U_L) in the legend for all the pathways are vs. RHE.

4.3.2. Quantification of reaction barriers

Climbing image nudged elastic band (CI-NEB) calculations were performed to estimate the height of the activation barriers based on the reaction path analysis presented in Figure 4.2. Figures 4.5 to 4.8 show the reaction paths and activation barriers as calculated using CI-NEB. The energy values in these plots represent E_{DFT} and are not corrected for vibrational entropy, enthalpy, zero point energy and solvation. The data points in blue represent the system images along the potential energy surface in the direction of the transition state. The Bader charge analysis tables at the bottom of each plot give the excess negative or positive charge on the atoms. Figure A.14 in the Appendix shows the influence of the various corrections to the activation barriers calculated using CI-NEB calculations.

As can be seen in Figure 4.9, the activation barriers after correction for solvation for formation of ∗COOH and H_2 via Heyrovsky and Tafel steps are 0.93 eV, 0.79 eV and 0.77 eV respectively, with H_2 as the most thermodynamically favorable product. Interestingly however, there is no kinetic barrier for the formation of ∗OCHO involving the direct nucleophilic attack by ∗H. The high solvation energy of the transition state relative to the initial state for ∗OCHO (Table A.1, Figure A.14) plays an important role in diminishing the activation barrier for its formation. This analysis highlights the importance of the consideration of solvation in theoretical mechanistic studies for eCO_2R; a conclusion which is in agreement with what has been shown for other (electro)catalytic systems [53–55].

The presence of cationic and anionic species in the electrolyte may also influence the binding energies and activation barriers for the formation of certain reaction intermediates and there are ongoing efforts to include these effects in computational studies pertaining to eCO_2R [56, 57]. Based on the results in Figure 4.9, we show that there is a significant energy barrier for the formation of the CO pathway intermediate ∗COOH, whereas ∗OCHO is expected to form readily on the Ag(110) surface in the presence of ∗H.

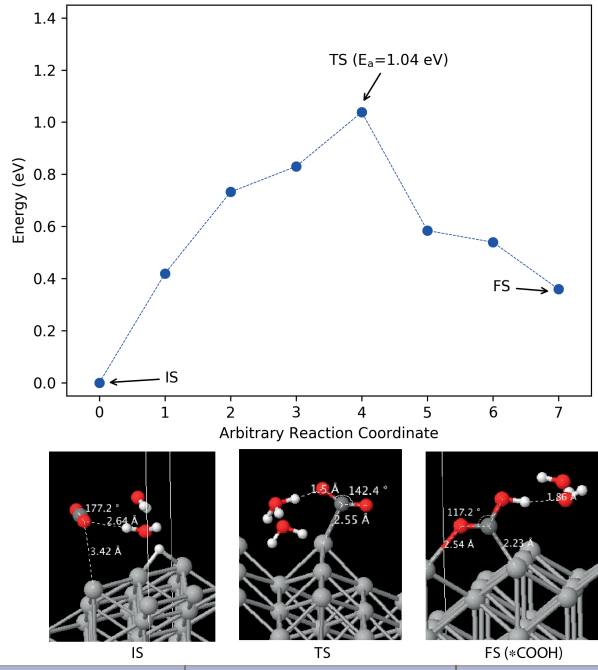

IS		TS		FS	
Atom	*Bader Charge*	*Atom*	*Bader Charge*	*Atom*	*Bader Charge*
O	-1.08	O	-1.12	∗O	-1.15
C	+2.16	C	+1.71	∗C	+1.19
O	-1.08	O	-1.09	O	-1.10
∗H	-0.27	H(solv.)	+0.65	H	+0.61

Figure 4.5: (top) Activation barrier for the formation of ∗COOH along with the geometrical configuration of the IS: initial state, TS: transition state and FS: final state. (bottom) Excess Bader charges on reacting atoms.

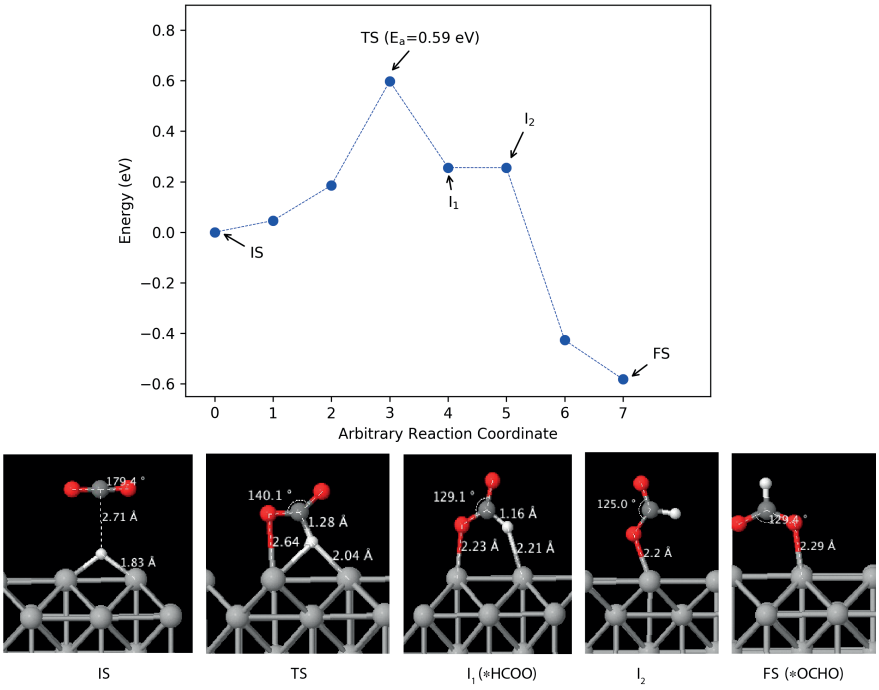

IS		TS		FS	
Atom	*Bader Charge*	*Atom*	*Bader Charge*	*Atom*	*Bader Charge*
O	-1.08	∗O	-1.12	∗O	-1.14
C	+2.16	C	+1.63	C	+1.58
O	-1.08	O	-1.07	∗O	-1.14
∗H	-0.27	∗H	-0.15	H	+0.02

Figure 4.6: (top) Activation barrier for the formation of ∗OCHO along with the geometrical configuration of the IS: initial state, TS: transition state and FS: final state. Images I_1 and I_2 have been shown for the sake of clarity of the reaction path. (bottom) Excess Bader charges on reacting atoms.

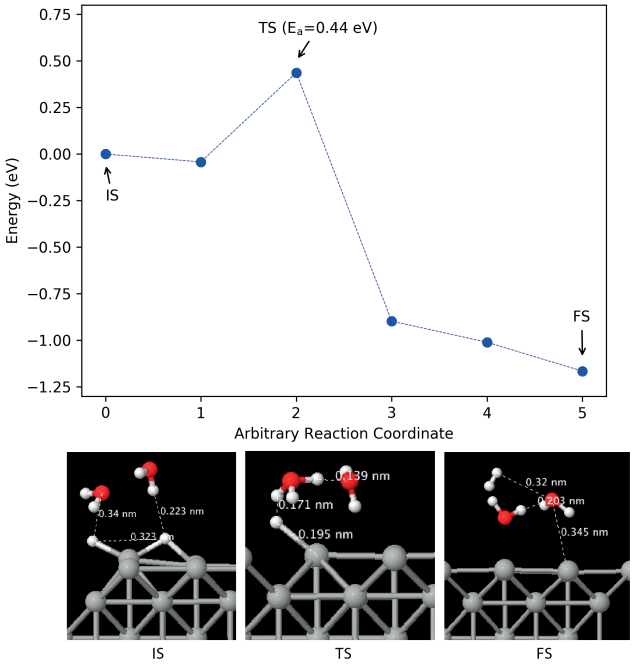

IS		TS		FS	
Atom	*Bader Charge*	*Atom*	*Bader Charge*	*Atom*	*Bader Charge*
∗H	-0.25	∗H	-0.36	H	0.00
∗H	-0.25	H(solv.)	+0.57	H	0.00

Figure 4.7: (top) Activation barrier for the formation of H_2 via a Heyrovsky mechanism along with the geometrical configuration of the IS: initial state, TS: transition state and FS: final state. (bottom) Excess Bader charges on reacting atoms.

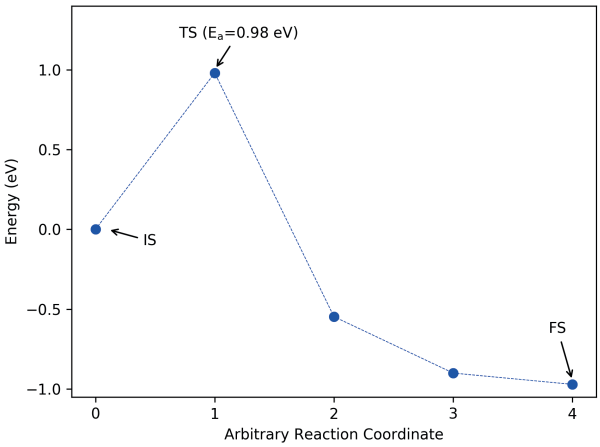

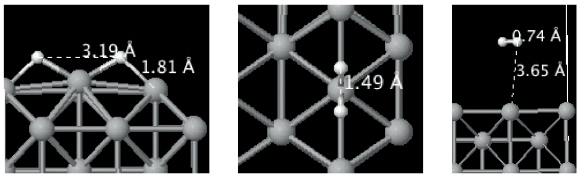

IS TS FS

IS		TS		FS	
Atom	*Bader Charge*	*Atom*	*Bader Charge*	*Atom*	*Bader Charge*
∗H	-0.25	∗H	-0.11	H	0.00

Figure 4.8: (top) Activation barrier for the formation of H_2 via a Tafel mechanism along with the geometrical configuration of the IS: initial state, TS: transition state and FS: final state. (bottom) Excess Bader charges on reacting atoms.

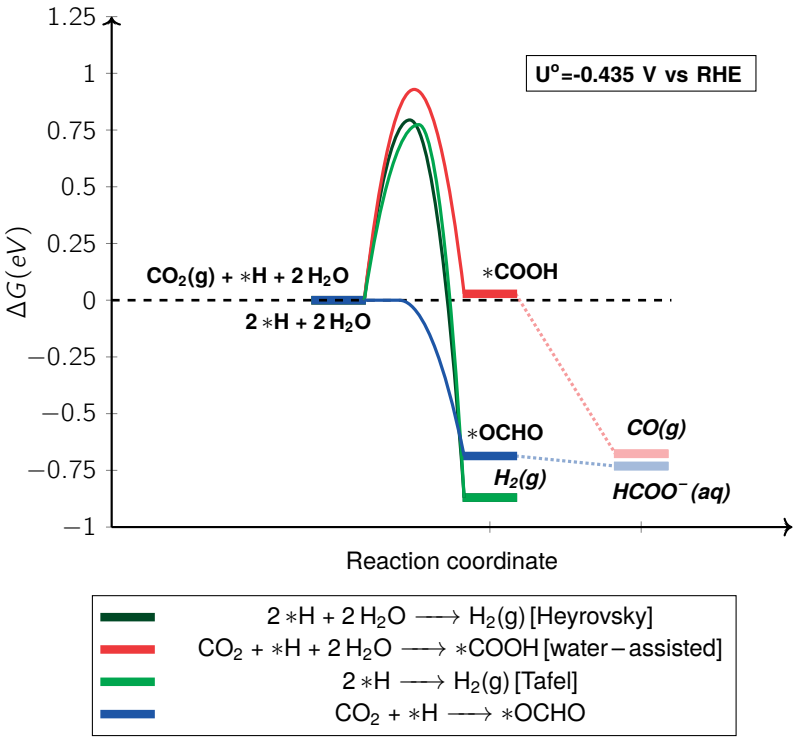

Figure 4.9: Free energy of activation for Ag(110) at a reference potential U^o=-0.435 V vs. RHE for the equilibrium between surface bound ∗H and the bulk proton and electron pair.

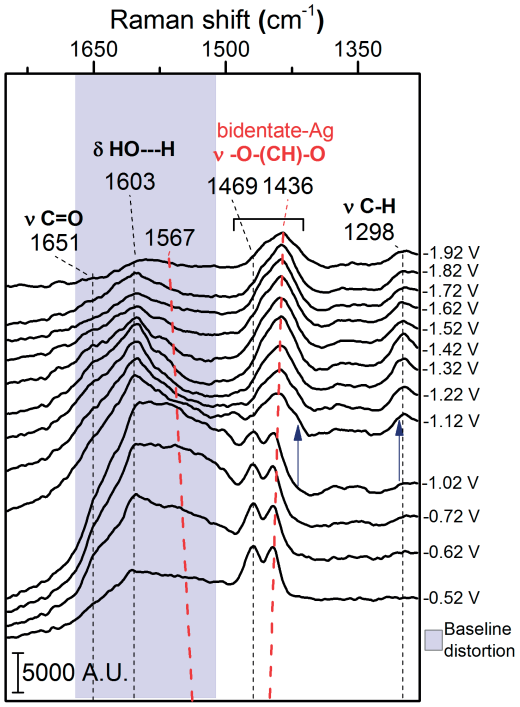

Figure 4.10: SERS spectra for eCO_2R on polycrystalline Ag in 0.05 M $Li_2B_4O_7$ saturated with CO_2 with a bulk pH of 6.1. The spectral region shows the O-bound bidentate species and the shift towards lower frequencies as we apply more cathodic potentials. The blue arrows indicate the formation of a new band at 1298 cm^{-1} related to the merging and shift of the bidentate bands. All potentials are given vs. RHE.

In order to validate our theoretical findings, preliminary *in-situ* electrochemical SERS measurements were performed to probe polycrystalline Ag catalyst surface during eCO_2R in 0.05 M $Li_2B_4O_7$ [58, 59] saturated with CO_2, with a bulk pH of 6.1 (see section A.1 for details). We observe a double-band shape at 1436 and 1469 cm^{-1} (Figure 4.10) corresponding to an O-bound bidentate intermediate on the Ag surface, which we believe to be the $*OCHO$ species based on similar evidence obtained in literature for carboxylate species on silver hydrosols [60]. The interactions of O-bound species with the Ag surface appear at relatively low overpotentials (-0.52 V vs RHE), in agreement with the obtained theoretical results. We also observe a correlation in the appearance of a $\delta C{-}H$ vibration band at

1298 cm^{-1} [61] with the bidentate signal merging into a broader band at more cathodic potentials of -1.12 V vs RHE as can be seen in Figure 4.10. The same correlation is observed using a lithium borate buffer solution with a bulk pH of 6.9 albeit at higher overpotentials (Figure A.11). These experiments suggest that pH plays an important role in eCO_2R at lower overpotentials due to its implications on the formation of ∗H on the Ag electrode.

4.3.3. Lateral adsorbate interactions

Adsorbate-adsorbate interactions are known to play an important role in determining the energetics of surface reactions including eCO_2R [62, 63]. Considering the high likelihood of the presence of ∗OCHO species on the Ag catalyst surface, we investigate its influence on the adsorption energies of reaction intermediates involved in the 2-electron reduction processes during eCO_2R. The free energy diagram for Ag(110) in Figure 4.11 shows that the presence of ∗OCHO weakens the ∗H binding significantly (green pathway in Figure 4.11 and Figure A.16) whereas the effect of its presence on the binding energies of the ∗COOH, *OCHO and ∗CO species is relatively smaller. As a result, the U_L for the formation of H_2 and $HCOO^-$ (both proceeding via the Volmer step), become much less favorable and comparable to the U_L for the formation of CO.

Figure A.15 shows the effect of the coverage of ∗H (θ_{*H}) on the binding energy of ∗COOH for Ag(110). It is clear that as θ_{*H} increases, the binding of ∗COOH on the catalyst surface becomes increasingly thermodynamically unfavorable. The presence of ∗OCHO therefore has two important consequences for the selectivity of Ag eCO_2R catalysts: firstly, ∗OCHO weakens the binding strength of ∗H with the catalyst surface, bringing the CO formation pathway to a level-playing field thermodynamically with the H_2 and $HCOO^-$ pathways. Secondly, the lower θ_{*H} as a consequence of the weaker ∗H binding enables the formation of ∗COOH, thereby improving the selectivity of the catalyst towards CO. The influence of lateral adsorbate interaction of ∗OCHO on the binding strength of ∗H diminishes as the activity of the catalytic surface reduces (see Figure A.17). The lower binding strength of ∗COOH in addition to the negligible effect on the binding strength of ∗H in the presence of ∗OCHO for Ag(111) (Figure A.18) is in line with the experimental observation that close-packed surfaces such

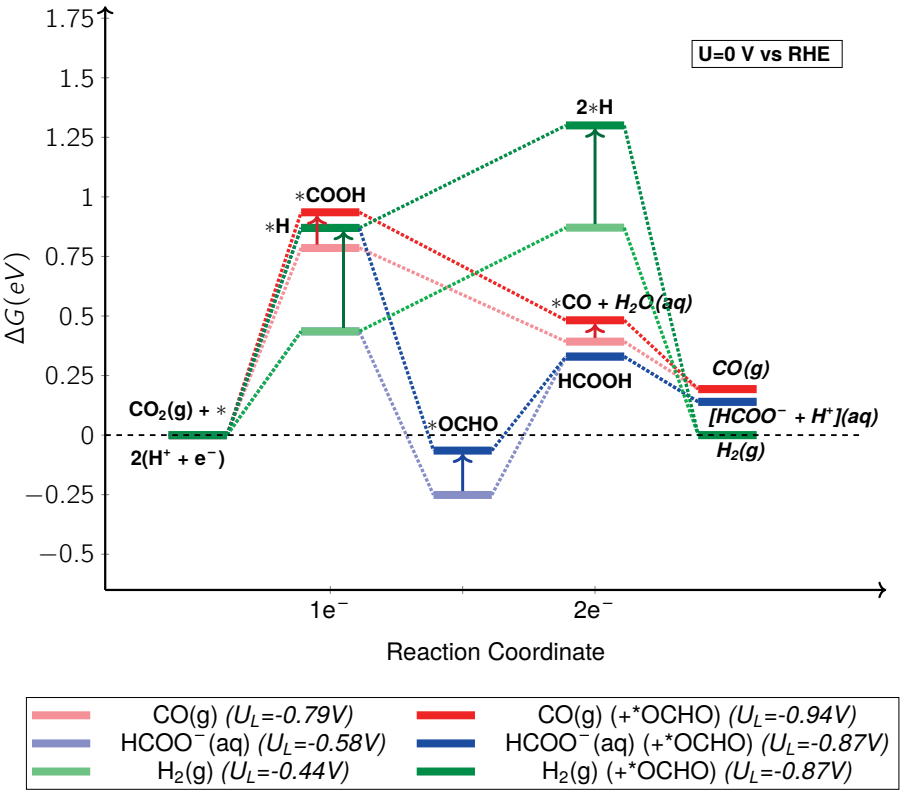

Figure 4.11: Free energy diagram for formation of CO(g), $HCOO^-$(aq) and H_2(g) on Ag(110) surface at 0 V vs. RHE. The adsorption energies shown in dark red, blue and green are in the presence of ∗OCHO (θ=1/3), whereas the energies in light red, blue and green are without ∗OCHO. The upward arrows denote the change in free energy of the respective intermediates due to the presence of ∗OCHO on the surface. Formation of ∗OCHO has been shown to occur following the formation of ∗H as per the proposed mechanism and is not an electron transfer step. Limiting potentials (U_L) are given vs. RHE.

as Ag(111) have drastically lower activity for eCO_2R to CO relative to Ag(110) [25]. This analysis highlights the importance of the consideration of lateral adsorbate-adsorbate interactions to bridge the discrepancy between theoretical predictions and the experimental observations for Ag as well as other eCO_2R catalysts.

4.4. Conclusions and Discussion

From our theoretical analysis, we come to the conclusion that the O-bound formate precursor species $*OCHO$, which is typically considered irrelevant for the CO producing catalyst Ag, should not only be present on the surface at low overpotentials during eCO_2R, but is also likely playing an active role in promoting the selectivity of Ag towards CO production. In addition, the results strongly indicate that factors such as θ_{*H} and solvation by surrounding water molecules will play an important role in controlling selectivity between the various eCO_2R products. Calculation of activation barriers at constant potential and adjusted for activities of reactant and electrolyte species in order to simulate the conditions during electrocatalysis remains a challenge and there is a need for further development of computational methodologies for this purpose. Our approach demonstrates a constructive interplay between theory and experiments to advance the understanding of a complex system of high practical significance. The results highlight the need to study the catalyst surface in its operational steady state, both theoretically and experimentally, to understand the synergistic and competitive effects between the reaction species that ultimately result in the observed performance.

References

[1] D. Bohra, I. Ledezma-Yanez, G. Li, W. de Jong, E. A. Pidko, and W. A. Smith, *Lateral adsorbate interactions inhibit $HCOO^-$ while promoting CO selectivity for CO_2 electrocatalysis on silver,* Angewandte Chemie International Edition **58**, 1345 (2019).

[2] Q. Lu and F. Jiao, *Electrochemical CO_2 reduction: Electrocatalyst, reaction mechanism, and process engineering,* Nano Energy **29**, 439 (2016).

[3] M. Gattrell, N. Gupta, and A. Co, *Electrochemical reduction of CO_2 to hydrocarbons to store renewable electrical energy and upgrade biogas,* Energy Conversion and Management **48**, 1255 (2007).

[4] D. A. Tryk and A. Fujishima, *Electrochemists enlisted in war: The carbon dioxide reduction battle,* The Electrochemical Society Interface , 32 (2001).

[5] D. T. Whipple and P. J. A. Kenis, *Prospects of CO_2 utilization via direct heterogeneous electrochemical reduction,* The Journal of Physical Chemistry Letters **1**, 3451 (2010).

[6] O. Edenhofer, R. Pichs-Madruga, Y. Sokona, E. Farahani, S. Kadner, K. Seyboth, A. Adler, I. Baum, S. Brunner, P. Eickemeier, B. Kriemann, J. Savolainen, S. Schlömer, C. von Stechow, T. Zwickel, and J. Minx (eds.), *Cambridge University Press, Cambridge, United Kingdom and New York, NY, USA*, Tech. Rep. (Intergovernmental Panel on Climate Change, 2014).

[7] M. T. Koper, *Thermodynamic theory of multi-electron transfer reactions: Implications for electrocatalysis,* Journal of Electroanalytical Chemistry **660**, 254 (2011), physics and Chemistry of Charge Transfer in Condensed Media.

[8] J. Durst, A. Rudnev, A. Dutta, Y. Fu, J. Herranz, V. Kaliginedi, A. Kuzume, A. A. Permyakova, Y. Paratcha, P. Broekmann, and T. J. Schmidt, *Electrochemical CO_2 reduction – A critical view on fundamentals, materials and applications,* CHIMIA International Journal for Chemistry **69**, 769 (2015).

[9] G. Centi and S. Perathoner, *Opportunities and prospects in the chemical recycling of carbon dioxide to fuels,* Catalysis Today **148**, 191 (2009).

[10] C. Oloman and H. Li, *Electrochemical processing of carbon dioxide,* ChemSusChem **1**, 385 (2008).

[11] C. Song, *Global challenges and strategies for control, conversion and utilization of CO_2 for sustainable development involving energy, catalysis, adsorption and chemical processing,* Catalysis Today **115**, 2 (2006).

[12] S. Verma, B. Kim, H.-R. Jhong, S. Ma, and P. J. A. Kenis, *A gross-margin model for defining technoeconomic benchmarks in the electroreduction of CO_2,* ChemSusChem **9**, 1972 (2016).

[13] T. Hatsukade, K. P. Kuhl, E. R. Cave, D. N. Abram, and T. F. Jaramillo, *Insights into the electrocatalytic reduction of CO_2 on metallic silver surfaces,* Phys. Chem. Chem. Phys. **16**, 13814 (2014).

[14] M. Ma, B. J. Trześniewski, J. Xie, and W. A. Smith, *Selective and efficient reduction of carbon dioxide to carbon monoxide on oxide-derived nanostructured silver electrocatalysts,* Angewandte Chemie International Edition **55**, 9748 (2016).

[15] A. Seifitokaldani, C. M. Gabardo, T. Burdyny, C.-T. Dinh, J. P. Edwards, M. G. Kibria, O. S. Bushuyev, S. O. Kelley, D. Sinton, and E. H. Sargent, *Hydronium-induced switching between CO_2 electroreduction pathways,* Journal of the American Chemical Society **140**, 3833 (2018).

[16] Y. Yoon, A. S. Hall, and Y. Surendranath, *Tuning of silver catalyst mesostructure promotes selective carbon dioxide conversion into fuels,* Angewandte Chemie International Edition **55**, 15282 (2016).

[17] Q. Lu, J. Rosen, and F. Jiao, *Nanostructured metallic electrocatalysts for carbon dioxide reduction,* ChemCatChem **7**, 38 (2015).

[18] C. Kim, H. S. Jeon, T. Eom, M. S. Jee, H. Kim, C. M. Friend, B. K. Min, and Y. J. Hwang, *Achieving selective and efficient electrocatalytic activity for CO_2 reduction using immobilized silver nanoparticles,* Journal of the American Chemical Society **137**, 13844 (2015).

[19] J. Rosen, G. S. Hutchings, Q. Lu, S. Rivera, Y. Zhou, D. G. Vlachos, and F. Jiao, *Mechanistic insights into the electrochemical reduction of CO_2 to CO on nanostructured Ag surfaces,* ACS Catalysis **5**, 4293 (2015).

[20] A. M. Appel, J. E. Bercaw, A. B. Bocarsly, H. Dobbek, D. L. DuBois, M. Dupuis, J. G. Ferry, E. Fujita, R. Hille, P. J. A. Kenis, C. A. Kerfeld, R. H. Morris, C. H. F. Peden, A. R. Portis, S. W. Ragsdale, T. B. Rauchfuss, J. N. H. Reek, L. C. Seefeldt, R. K. Thauer, and

G. L. Waldrop, *Frontiers, opportunities, and challenges in biochemical and chemical catalysis of CO_2 fixation,* Chemical Reviews **113**, 6621 (2013).

[21] J. S. Yoo, R. Christensen, T. Vegge, J. K. Nørskov, and F. Studt, *Theoretical insight into the trends that guide the electrochemical reduction of carbon dioxide to formic acid,* ChemSusChem **9**, 358 (2016).

[22] J. T. Feaster, C. Shi, E. R. Cave, T. Hatsukade, D. N. Abram, K. P. Kuhl, C. Hahn, J. K. Nørskov, and T. F. Jaramillo, *Understanding selectivity for the electrochemical reduction of carbon dioxide to formic acid and carbon monoxide on metal electrodes,* ACS Catalysis **7**, 4822 (2017).

[23] A. Bagger, W. Ju, A. S. Varela, P. Strasser, and J. Rossmeisl, *Electrochemical CO_2 reduction: A classification problem,* ChemPhysChem **18**, 3266.

[24] R. Kortlever, J. Shen, K. J. P. Schouten, F. Calle-Vallejo, and M. T. M. Koper, *Catalysts and reaction pathways for the electrochemical reduction of carbon dioxide,* Journal of Physical Chemistry Letters **6**, 4073 (2015).

[25] N. Hoshi, M. Kato, and Y. Hori, *Electrochemical reduction of CO_2 on single crystal electrodes of silver Ag(111), Ag(100) and Ag(110),* Journal of Electroanalytical Chemistry **440**, 283 (1997).

[26] S. Bahn and K. Jacobsen, *An object-oriented scripting interface to a legacy electronic structure code,* Computing in Science & Engineering **4**, 56 (2002).

[27] J. Enkovaara, C. Rostgaard, J. J. Mortensen, J. Chen, M. Dułak, L. Ferrighi, J. Gavnholt, C. Glinsvad, V. Haikola, H. A. Hansen, H. H. Kristoffersen, M. Kuisma, A. H. Larsen, L. Lehtovaara, M. Ljungberg, O. Lopez-Acevedo, P. G. Moses, J. Ojanen, T. Olsen, V. Petzold, N. A. Romero, J. Stausholm-Møller, M. Strange, G. A. Tritsaris, M. Vanin, M. Walter, B. Hammer, H. Häkkinen, G. K. H. Madsen, R. M. Nieminen, J. K. Nørskov, M. Puska, T. T. Rantala, J. Schiøtz, K. S. Thygesen, and K. W. Jacobsen, *Electronic structure*

calculations with GPAW: a real-space implementation of the projector augmented-wave method, J. Phys.: Condens. Matter **22**, 253202 (2010).

[28] J. J. Mortensen, L. B. Hansen, and K. W. Jacobsen, *Real-space grid implementation of the projector augmented wave method,* Physical Review B **71**, 035109 (2005).

[29] J. Wellendorff, K. T. Lundgaard, A. Møgelhøj, V. Petzold, D. D. Landis, J. K. Nørskov, T. Bligaard, and K. W. Jacobsen, *Density functionals for surface science: Exchange-correlation model development with bayesian error estimation,* Phys. Rev. B **85**, 235149 (2012).

[30] J. Wellendorff, T. L. Silbaugh, D. Garcia-Pintos, J. K. Nørskov, T. Bligaard, F. Studt, and C. T. Campbell, *A benchmark database for adsorption bond energies to transition metal surfaces and comparison to selected DFT functionals,* Surface Science **640**, 36 (2015).

[31] G. Henkelman, B. P. Uberuaga, and H. Jónsson, *A climbing image nudged elastic band method for finding saddle points and minimum energy paths,* The Journal of Chemical Physics **113**, 9901 (2000).

[32] G. Henkelman, A. Arnaldsson, and H. Jónsson, *A fast and robust algorithm for Bader decomposition of charge density,* Computational Materials Science **36**, 354 (2006).

[33] S. Edward, K. S. D., S. Roger, and H. Graeme, *Improved grid-based algorithm for Bader charge allocation,* Journal of Computational Chemistry **28**, 899.

[34] M. Yu and D. R. Trinkle, *Accurate and efficient algorithm for Bader charge integration,* The Journal of Chemical Physics **134**, 064111 (2011).

[35] W. Tang, E. Sanville, and G. Henkelman, *A grid-based bader analysis algorithm without lattice bias,* Journal of Physics: Condensed Matter **21**, 084204 (2009).

[36] C. J. Cramer, *Essentials of Computational Chemistry*, Vol. 42 (Wiley, 2004) pp. 334–342.

[37] K. Chan, C. Tsai, H. A. Hansen, and J. K. Nørskov, *Molybdenum sulfides and selenides as possible electrocatalysts for CO_2 reduction,* ChemCatChem **6**, 1899 (2014).

[38] F. Studt, F. Abild-Pedersen, J. B. Varley, and J. K. Nørskov, *CO and CO_2 hydrogenation to methanol calculated using the BEEF-vdW functional,* Catalysis Letters **143**, 71 (2013).

[39] H. A. Hansen, C. Shi, A. C. Lausche, A. A. Peterson, and J. K. Nørskov, *Bifunctional alloys for the electroreduction of CO_2 and CO,* Phys. Chem. Chem. Phys. **18**, 9194 (2016).

[40] M. Fishman, H. L. Zhuang, K. Mathew, W. Dirschka, and R. G. Hennig, *Accuracy of exchange-correlation functionals and effect of solvation on the surface energy of copper,* Phys. Rev. B **87**, 245402 (2013).

[41] K. Mathew, R. Sundararaman, K. Letchworth-Weaver, T. A. Arias, and R. G. Hennig, *Implicit solvation model for density-functional study of nanocrystal surfaces and reaction pathways,* The Journal of Chemical Physics **140**, 084106 (2014).

[42] G. Kresse and J. Hafner, *Ab initio molecular dynamics for liquid metals,* Phys. Rev. B **47**, 558 (1993).

[43] G. Kresse and J. Furthmüller, *Efficient iterative schemes for ab initio total-energy calculations using a plane-wave basis set,* Phys. Rev. B **54**, 11169 (1996).

[44] A. A. Peterson, F. Abild-Pedersen, F. Studt, J. Rossmeisl, and J. K. Nørskov, *How copper catalyzes the electroreduction of carbon dioxide into hydrocarbon fuels,* Energy Environ. Sci. **3**, 1311 (2010).

[45] S. A. Akhade, N. J. Bernstein, M. R. Esopi, M. J. Regula, and M. J. Janik, *A simple method to approximate electrode potential-dependent activation energies using density functional theory,* Catalysis Today **288**, 63 (2017).

[46] R. F. W. Bader, *Atoms in Molecules: A Quantum Theory* (Oxford University Press, New York, 1994).

[47] T. Cheng, H. Xiao, and W. A. Goddard, *Reaction mechanisms for the electrochemical reduction of CO_2 to CO and formate on the Cu(100) surface at 298 K from quantum mechanics free energy calculations with explicit water,* Journal of the American Chemical Society **138**, 13802 (2016).

[48] A. J. Göttle and M. T. M. Koper, *Determinant role of electrogenerated reactive nucleophilic species on selectivity during reduction of CO_2 catalyzed by metalloporphyrins,* Journal of the American Chemical Society **140**, 4826 (2018).

[49] T. Hatsukade, K. P. Kuhl, E. R. Cave, D. N. Abram, and T. F. Jaramillo, *Insights into the electrocatalytic reduction of CO_2 on metallic silver surfaces.* Physical chemistry chemical physics : PCCP **16**, 13814 (2014).

[50] Y. Hori, *Electrochemical CO_2 reduction on metal electrodes,* in *Modern Aspects of Electrochemistry*, 42 (Springer, New York, 2008) pp. 89–189.

[51] M. Schreier, Y. Yoon, M. N. Jackson, and Y. Surendranath, *Competition between H and CO for active sites governs copper-mediated electrosynthesis of hydrocarbon fuels,* Angewandte Chemie International Edition **57**, 10221.

[52] X. Nie, M. R. Esopi, M. J. Janik, and A. Asthagiri, *Selectivity of CO_2 reduction on copper electrodes: The role of the kinetics of elementary steps,* Angewandte Chemie **125**, 2519 (2013).

[53] C. Michel, J. Zaffran, A. M. Ruppert, J. Matras-Michalska, M. Jędrzejczyk, J. Grams, and P. Sautet, *Role of water in metal catalyst performance for ketone hydrogenation: A joint experimental and theoretical study on levulinic acid conversion into gamma-valerolactone,* Chem. Commun. **50**, 12450 (2014).

[54] D. Loffreda, C. Michel, F. Delbecq, and P. Sautet, *Tuning catalytic reactivity on metal surfaces: Insights from DFT,* Journal of Catalysis **308**, 374 (2013), 50th Anniversary Special Issue.

[55] Y. Sha, T. H. Yu, Y. Liu, B. V. Merinov, and W. A. Goddard, *Theoretical study of solvent effects on the platinum-catalyzed oxygen*

reduction reaction, The Journal of Physical Chemistry Letters **1**, 856 (2010).

[56] L. D. Chen, M. Urushihara, K. Chan, and J. K. Nørskov, *Electric field effects in electrochemical CO_2 reduction,* ACS Catalysis **6**, 7133 (2016).

[57] J. Resasco, L. D. Chen, E. Clark, C. Tsai, C. Hahn, T. F. Jaramillo, K. Chan, and A. T. Bell, *Promoter effects of alkali metal cations on the electrochemical reduction of carbon dioxide,* Journal of the American Chemical Society **139**, 11277 (2017), pMID: 28738673.

[58] I. Ledezma-Yanez, W. D. Z. Wallace, P. Sebastián-Pascual, V. Climent, J. M. Feliu, and M. T. M. Koper, *Interfacial water reorganization as a pH-dependent descriptor of the hydrogen evolution rate on platinum electrodes,* Nature Energy **2**, 17031 (2017).

[59] J. Rossmeisl, K. Chan, R. Ahmed, V. Tripković, and M. E. Björketun, *pH in atomic scale simulations of electrochemical interfaces,* Phys. Chem. Chem. Phys. **15**, 10321 (2013).

[60] S. Kai, W. Chaozhi, and X. Guangzhi, *Surface enhanced Raman spectra of carbonate, hydrocarbonate, and substituted acetic acids on silver hydrosols,* Spectrochimica Acta Part A: Molecular Spectroscopy **45**, 1029 (1989).

[61] H. Edwards and J. M. Chalmers, *Handbook of Vibrational Spectroscopy*, edited by J. M. Chalmers and P. R. Griffiths (John Wiley & Sons, Ltd, 2006) Chap. Spectra-Structure Correlations in Raman Spectroscopy, pp. 1887 – 1890.

[62] L. C. Grabow, B. Hvolbæk, and J. K. Nørskov, *Understanding trends in catalytic activity: The effect of adsorbate-adsorbate interactions for CO oxidation over transition metals,* Topics in Catalysis **53**, 298 (2010).

[63] E. R. Cave, C. Shi, K. P. Kuhl, T. Hatsukade, D. N. Abram, C. Hahn, K. Chan, and T. F. Jaramillo, *Trends in the catalytic activity of hydrogen evolution during CO_2 electroreduction on transition metals,* ACS Catalysis **8**, 3035 (2018).

5

Modeling the reaction environment

The environment of a CO_2 electroreduction (eCO_2R) catalyst is intimately coupled with the surface reaction energetics and is therefore a critical aspect of the overall system performance. The immediate reaction environment of the electrocatalyst constitutes the electrical double layer (EDL) which extends a few nanometers into the electrolyte and screens the surface charge density. In this study, we resolve the species concentrations and potential profiles in the EDL of an eCO_2R system by self-consistently solving the migration, diffusion and reaction phenomena using the generalized modified Poisson-Nernst-Planck (GMPNP) equations which include the effect of volume exclusion due to the solvated size of solution species. We demonstrate that the concentration of solvated cations builds at the outer Helmholtz plane (OHP) with increasing applied potential until the steric limit is reached. The formation of the EDL is expected to have important consequences for the transport of the CO_2 molecule to the catalyst surface. The electric field in the EDL diminishes the pH in the first 5 nm from the OHP, with an accumulation of protons and a concomitant depletion of hydroxide ions. This is a considerable departure from the results obtained using reaction-diffusion models where migration is ignored. Finally, we use the GMPNP model to compare the nature of the EDL for different alkali metal cations to show the effect of solvated size and polarization of water on the resultant electric field. Our results establish the significance of the EDL and electrostatic forces in defining the local reaction environment of CO_2 electrocatalysts.

This chapter has been published in Energy Environ. Sci. **12**, 3380 (2019) [1].

Research work led by Divya Bohra; Jehanzeb H. Chaudhry provided guidance for the numerical simulations; Thomas Burdyny and Evgeny A. Pidko played supervisory role; Wilson A. Smith supervised the project as the principal investigator.

5.1. Introduction

The immediate environment of the CO_2 electro-reduction (eCO_2R) catalyst is an extremely important handle to rationally optimize the overall performance of the system [2]. The concentrations of reactive as well as non-reactive species in the vicinity of the catalyst surface, and their mutual interactions, have a direct influence on catalytic behavior, and thus on the achievable activity and selectivity [3, 4]. Mass transport becomes a crucial factor for eCO_2R due to the limited solubility of CO_2 in aqueous electrolytes, the participation of CO_2 in the buffer reactions, as well as the changes in the local environment during reaction due to the continuous consumption of CO_2 and production of hydroxide (OH^-) ions. Designing more favorable reaction interfaces has helped to achieve remarkable performance gains [5–7] and the approach highlights the significance of mass transport as an influential optimization parameter for the eCO_2R system. What constitutes the local reaction environment in such an electrocatalytic system however, is still an open question. Further understanding needs to be developed to define the physical phenomena that result in the local environment of the catalyst and that sufficiently capture the parameters most important for the performance.

Although there have been several attempts to model the mass transport of solution species to the catalyst surface in eCO_2R, a vast majority of the existing literature is restricted to reaction-diffusion type models introduced by N. Gupta and co-authors [8] and ignore the formation of the electrical double layer (EDL) and therefore any migration of charged species in front of the catalyst surface [9–12]. The presence of the electrified interface has been used however, to explain the influence of cations on experimentally observed performance [4, 13]. Considering the significant applied voltage under which eCO_2R operates, the local environment for the catalysis is insufficiently defined without the inclusion of the electrostatic interactions of the ionic species with the charged metallic surface. These interactions, and the resulting double layer structure, can extend up to several nanometers from the catalyst surface (see Figure 5.1) and are necessary to consider in order to derive physically consistent hypotheses based on experimental observations.

In this study, we resolve the species concentrations and potential profiles in the EDL of a syngas (CO and H_2) producing eCO_2R system by self-

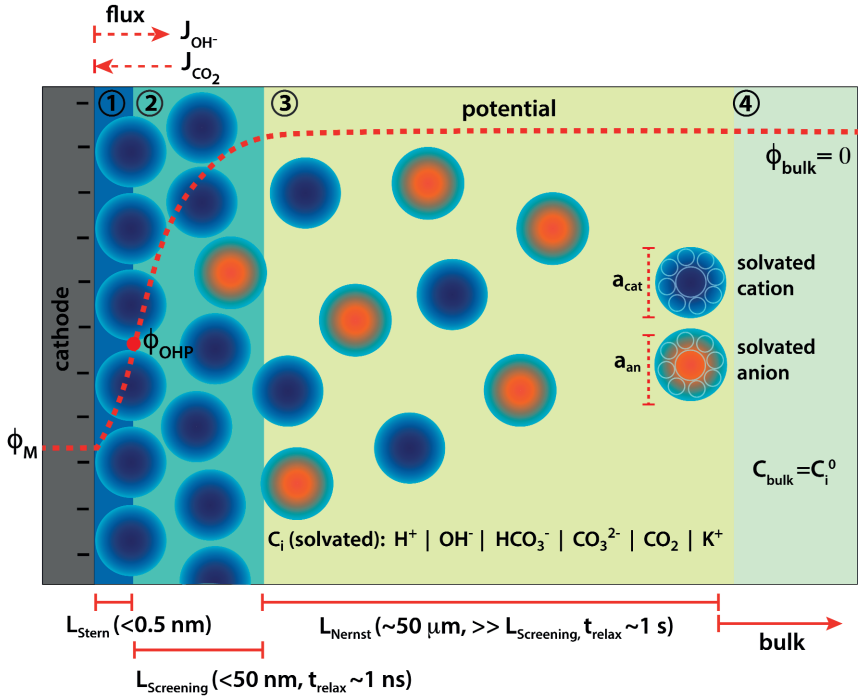

Figure 5.1: Schematic of the different mass transport zones in front of a cathode surface during eCO_2R in an aqueous electrolyte. Zone 1: Stern layer, Zone 2: potential screening layer, Zone 3: Nernst diffusion layer and Zone 4: bulk. The red dotted line in the electrolyte is a typical potential profile with ϕ_M and ϕ_{OHP} being the potential of the metal cathode and at the outer Helmholtz plane (OHP), respectively with the potential at the point of zero charge (PZC) of the catalyst surface as the reference potential (description in section 5.1.2). a_{cat} and a_{an} are the effective diameters of a solvated cation (in dark blue) and anion (in orange), respectively. L_{Stern}, $L_{Screening}$ and L_{Nernst} depict the dimensions of the Stern layer, potential screening layer and the Nernst diffusion layer, respectively and t_{relax} is the relaxation time (order of magnitude) relevant for the mass transport processes in the respective zone. $\mathbf{J}_i$ depicts the incoming and outgoing flux of species (i) OH^- and CO_2, respectively.

consistently solving the migration, diffusion and reaction phenomena in a CO_2 saturated aqueous electrolyte facing a planar cathode (see schematic in Figure 5.1). We do this by numerically solving the generalized modified Poisson-Nernst-Planck (GMPNP) set of equations which include the effect of volume exclusion due to the solvated size of solution species [14]. Using the GMPNP equations, we demonstrate that the inclusion of migration in the mass transport of species provides a drastically different picture of the catalyst reaction environment as compared to reaction-diffusion models. By comparing with a PNP system, where molecules are considered as point species without volume, we show how inclusion of size of solvated solution species is important to derive physically consistent concentration profiles at high operating potentials. The effect of volume exclusion in the GMPNP model results in a diminishing of CO_2 concentration from the EDL at high applied potentials providing strong evidence of many-body correlations playing an important role in the transport of CO_2 to the catalyst surface. The resistance to the transport of CO_2 to the catalyst surface through a densely packed layer of solvated cations can potentially play a role in the activation mechanism of the CO_2 molecule. Yet another important consequence of the interaction of the electrostatic forces in the EDL with charged species is a considerable drop in the pH and OH^- concentration for a distance of up to 5 nm from the outer Helmholtz plane (OHP). This has significant repercussions for the eCO_2R system especially from a mechanistic view-point, while requiring us to provide greater definition to what is defined as the 'local reaction environment'. Finally, we compare the properties of the EDL for different alkali metal cations and look at the results in view of the existing experimental evidence.

5.1.1. Choice of model

The Poisson-Boltzmann (PB) model, also known as the classical Gouy Chapman model [15, 16], uses dilute solution theory with point-like ionic species to model the electrical double layer which is assumed to be in equilibrium with the bulk. Similarly, the classical description from dilute solution theory of the dynamics of the double layer is given by the Poisson-Nernst-Planck (PNP) equations [17]. However, it has been shown that the PB and PNP models break down dramatically at voltages much higher than the thermal voltage ($\gg \phi_T = k_B T/e = 25$ mV, where k_B is the Boltzmann constant, T is the temperature and e is the fundamental charge

of the electron) [18] which is the region of interest for electrocatalytic applications such as eCO_2R.

One of the primary limitations of the dilute solution theory based models has been shown to be the breaking of the steric limit of ion concentration ($C_{steric} = a^{-3}$, where a is the effective size of the ion) close to the charged surface at high applied voltages relative to ϕ_T. Excluding steric effects then leads to unphysical high EDL capacitance values and inherently making the solution non-dilute in the double layer region irrespective of the concentration of the bulk solution [14, 19]. Therefore, in order to resolve the EDL of an eCO_2R system such that its essential qualitative nature is captured, we use the generalized modified PNP (GMPNP) equations [14, 20–24] to resolve the concentration and potential profiles in the screening layer (zones 2 + 3) which incorporate a mean-field continuum description of steric effects to the dilute solution theory based time-dependent PNP system. This modification is in addition to the Stern layer [25, 26], where the surface catalytic reactions occur (zone 1 in Figure 5.1), which defines the plane of closest approach; the so-called outer-Helmholtz plane (OHP). Poisson equation is used to derive the potential profile for the Stern layer as described in the following section.

5.1.2. Model description

The heterogeneous reactions (5.1) and (5.2) are considered to be occurring at the planar cathode surface in the eCO_2R process, where the protons are provided by water. For simplicity, we base our calculations on CO producing catalysts such as Ag and Au but the analysis can be easily extended to catalysts producing a wider range of CO_2 reduction products. We do not assume a Faradaic current due to the consumption of H^+ in our base-case. A comparison of the base-case with the scenario where a maximum of 10% of the bulk concentration of H^+ is present at the OHP (limiting H^+ current case) can be found in section B.1.4 in Appendix B.

$$CO_2(aq) + H_2O + 2\,e^- \rightleftharpoons CO(g) + 2\,OH^- \tag{5.1}$$

$$2\,H_2O + 2\,e^- \rightleftharpoons H_2(g) + 2\,OH^- \tag{5.2}$$

A total current density (j_{tot}) and CO Faradaic efficiency (FE_{CO}, defined as the ratio of electrons consumed for the production of CO vs. H_2)

is assumed for the simulations and data is generated for a range of j_{tot} and FE_{CO} values. The flux of the solution species at the surface is then given by equations (5.3), (5.4) and (5.5). Our simulations are in 1D and x=0 is considered to be at the OHP (the boundary between the zone 1 and zone 2 in Figure 5.1).

$$\vec{J_i}|_{x=0,t} = 0 \quad i = HCO_3^-, CO_3^{2-}, K^+, H^+ \tag{5.3}$$

$$\vec{J}_{CO_2}|_{x=0,t} = \frac{1}{n_{e,CO}} \times \frac{j_{tot}}{F} \times FE_{CO} \tag{5.4}$$

$$\vec{J}_{OH^-}|_{x=0,t} = -\frac{1}{n_{e,OH^-}} \times \frac{j_{tot}}{F} \tag{5.5}$$

where F is the Faraday's constant, t is the time, $n_{e,CO} = 2$ is the number of electrons consumed to reduce CO_2 to CO and $n_{e,OH^-} = 1$ is the number of electrons consumed per OH^- produced. The following homogeneous reactions (5.6), (5.7) and (5.8) are considered to be occurring in the electrolyte:

$$\mathrm{H_2O} \underset{k_{w2}}{\overset{k_{w1}}{\rightleftharpoons}} \mathrm{H^+ + OH^-} \tag{5.6}$$

$$\mathrm{HCO_3^- + OH^-} \underset{k_{a2}}{\overset{k_{a1}}{\rightleftharpoons}} \mathrm{CO_3^{2-} + H_2O} \tag{5.7}$$

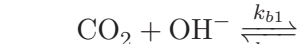

$$\mathrm{CO_2 + OH^-} \underset{k_{b2}}{\overset{k_{b1}}{\rightleftharpoons}} \mathrm{HCO_3^-} \tag{5.8}$$

The values of the rate constants for the reactions (5.6), (5.7) and (5.8) can be found in table B.2 in Appendix B. The bulk values of the concentrations of the solution species: H^+, OH^-,HCO_3^-, CO_2, CO_3^{2-} and K^+ for a 0.1 M $KHCO_3$ solution saturated with CO_2 are assumed to be constant and are calculated by solving the transient rate equations for reactions (5.6), (5.7) and (5.8) combined with the Sechenov equation [27, 28] (see section B.1.2 in Appendix B for details). Varying the bulk concentration of $KHCO_3$ will not change the nature of the EDL presented in this chapter unless either the solution volume is very small or the concentration of electrolyte is too low such that the bulk gets significantly depleted of counter-ions. However, the buffering capacity, the CO_2 solubility and therefore the concentration profiles beyond the EDL will vary considerably.

The GMPNP equations used to model the mass transport of electrolyte species (for zones 2 + 3 in Figure 5.1) are given by:

$$\frac{\partial C_i}{\partial t} = -\nabla \cdot \vec{J}_i + \sum_p R_i \tag{5.9}$$

where C_i is the concentration of species i, p is the index of the homogeneous reaction in solution, R_i is the rate of production of species i due to the homogeneous reaction p as given by equations (B.6) to (B.10) in Appendix B and $\vec{J}_i$ is the flux of species i given by:

$$\vec{J}_i = -D_i \nabla C_i - \frac{D_i C_i z_i F}{RT} \nabla \phi - D_i C_i \left(\frac{N_A \sum_{i=1}^{n} a_i^3 \nabla C_i}{1 - N_A \sum_{i=1}^{n} a_i^3 C_i} \right) \tag{5.10}$$

where D_i is the diffusion coefficient of species i, z_i is the charge of species i, R is the gas constant, T is the temperature, ϕ is the potential, N_A is the Avogadro's constant and a_i is the effective solvated diameter of the species i. The values of D_i and a_i used for the solution species in this work are provided in tables B.2 and B.2 in Appendix B, respectively. Equation (5.9) is solved simultaneously with the Poisson equation given by:

$$\nabla \cdot (\varepsilon_0 \varepsilon_r \nabla \phi) = -F \sum_{i=1}^{n} z_i C_i \tag{5.11}$$

where ε_0 is the permittivity of vacuum and ε_r is the relative permittivity of water.

Our simulations assume an overall Nernst diffusion length of 50 μm. Dirichlet boundary conditions are used for the potential at the OHP (left-hand boundary) as well as for the concentration of species and potential in the bulk (right-hand boundary). Neumann boundary conditions are used for the flux of species at x=0 as per equations (5.3), (5.4) and (5.5). The initial conditions for the concentrations are assumed to be at bulk values with $\phi = 0$ V vs PZC everywhere in the electrolyte. The scaled form of the GMPNP equations used for the numerical simulations are given in section B.1.5 in Appendix B.

The potential at the point of zero charge (PZC, $\phi_{\sigma=0}$) of the cathode is the potential at which the charge density of the surface is zero and

no electrical double layer is therefore present in the electrolyte solution facing the electrode. The potential profile can be considered to be a flat line across the metal-electrolyte interface at the PZC thereby leading to a Dirichlet boundary condition of $\phi_{bulk=0}$ at the right-hand boundary as well as an initial condition of $\phi = 0$ V vs PZC in the entire simulation domain. The $\phi_{\sigma=0}$ is thus a natural choice for a reference for all the potential values used in this study. PZC of a metal surface depends on the crystal facet as well as on the electrolyte solution in case specific adsorption happens on the surface [29]. For reference, the PZC in an aqueous solution for Ag surfaces is given in table B.2 in Appendix B. The range of OHP potentials considered in our simulations correspond to surface potentials of -0.10 to -0.61 V vs PZC, which translate to -0.55 to -1.06 V vs SHE for a Ag(111) surface and -0.80 to -1.31 V vs SHE for a polycrystalline Ag surface. It should be noted that the PZC for a polycrystalline metallic surface is not a uniquely defined quantity but is in some cases estimated using the minimum of the measured differential capacitance. We assume only non-specific adsorption of solvent species on the cathode surface for our simulations.

The relative permittivity in equation (5.11) is assumed to vary with cation concentration as given by equation (5.12) [30, 31]. The concentration terms in the equation (5.12) are in mol dm^{-3} and M_{water} is the molarity of water at room temperature taken as 55 M. The parameter w_i is the total number of water molecules held by the ion i. ε_r^0 is taken to be 80.1 equal to the relative permittivity of water at room temperature whereas ε_r^{min} is the dielectric constant of water under the condition of dielectric saturation and is taken equal to 6. The model in equation (5.12) is thus a summation of the contributions of bulk and cation-bounded water molecules to the relative permittivity. More advanced models such as the Booth model describe the dependence of the relative permittivity of the electrolyte medium as a function of the electric field [32, 33]. However, the Booth model is numerically more challenging to solve simultaneously with the GMPNP due to its non-linear nature.

$$\varepsilon_r = \varepsilon_r^0 \left(\frac{M_{water} - \sum_i^{ncat} w_i C_i}{M_{water}} \right) + \varepsilon_r^{min} \left(\frac{\sum_i^{ncat} w_i C_i}{M_{water}} \right) \tag{5.12}$$

The potential profile in the Stern region (zone 1, Figure 5.1) can be

post-calculated using equation (5.13) from the values of relative permittivity
($\varepsilon_{r,OHP}$) and electric field at the OHP obtained from the solution of the GMPNP equations for a given value of potential at the OHP. The width of the Stern layer is assumed to be 0.4 nm which is slightly larger than the radius of the largest cation considered in this study (Li^+). The electric field value and the potential value at the OHP are used as Neumann and Dirichlet boundary conditions for equation (5.13), respectively.

$$\nabla \cdot (\varepsilon_0 \varepsilon_{r,OHP} \nabla \phi) = 0 \tag{5.13}$$

The description for the reaction-diffusion model and the PNP model used for comparison with the GMPNP model described above can be found in Appendix B.

5.1.3. Numerical simulations

The GMPNP (equations (5.9)-(5.11)), PNP (equations (B.29)-(B.31) in Appendix B) as well as the reaction-diffusion system (equations (B.27) and (B.28) in Appendix B) are solved using the finite element method for spacial discretization and a backward Euler scheme for temporal discretization. The simulation domain in 1D is depicted in Figure B.1 in Appendix B. The backward Euler scheme, although computationally more intensive, was found to be necessary considering the stiff nature of both the PNP and GMPNP system of equations. We use the Python package FEniCS project [34, 35] to solve the weak Galerkin form of the transient non-linear GMPNP system such that the mass balance equation (5.9) and the Poisson equation (5.11) are solved self-consistently using the Newton method till a steady-state is reached.

The GMPNP as well as the PNP system are highly numerically unstable at the large values of applied potentials (relative to the thermal voltage ϕ_T) that are relevant for eCO_2R. The two most challenging aspects of numerically solving the (GM)PNP systems for the domain defined in this work are firstly, the characteristic length and time scales of the formation of the EDL are several orders of magnitude smaller than the length and time scales relevant for the homogeneous reaction and diffusion processes (see Figure 5.1). To simulate such a system as a single domain implies

that a variable finite element spatial mesh is needed to resolve the concentrations, both in the EDL, and in the entirety of the Nernst layer. In addition, due to numerical instability of the system very small time step sizes (1.0e-5 s) are required to converge to a solution, which makes the simulation computationally expensive to reach steady-state (10 s). Secondly, there is a very strong drift of charged species close to the cathode surface due to the high applied voltage as compared to the strength of diffusive flow in this EDL region (or a high Péclet number). This makes the standard Galerkin weak form further numerically unstable and the problem is exaggerated in the PNP relative to the GMPNP due to the assumption of point species that accumulate to unphysical high concentrations at the OHP. The inclusion of species volume in the GMPNP interestingly also make the equations numerically more stable than the PNP equations. We have used the streamline upwind Petrov-Galerkin (SUPG) method to stabilize the weak form of the PNP system in order to be able to use a computationally tractable time step size [36–39]. The formulation of the SUPG method used for PNP is described in detail in section B.1.8 in Appendix B.

5.2. Results

Figure 5.2 shows the potential and concentration profiles in the EDL region calculated using the GMPNP model for a fixed total current density of 1 mA/cm^2 with a Faradaic efficiency of CO of 0.8. The boundary condition for the potential at the OHP is varied to demonstrate the build-up of potassium ions in the EDL with increasing potential. It should be noted that the EDL is comprised of both the Stern layer as well as the potential screening layer which lies beyond the OHP (zones 1 and 2 in Figure 5.1). Since the concentration of solution species does not penetrate the OHP by definition, all the concentration profile plots start from the OHP (x=0) whereas the potential profile shown in Figure 5.2a starts at x=-0.4 nm which signifies the catalyst surface. As discussed previously, all voltage values are referenced against $\phi_{\sigma=0}$ and are thus given in V vs PZC. The concentration of K^+ cations increases till the steric limit a_{K+}^{-3}, where a_{K+} is the effective size of the solvated K^+ ion (Figure 5.2b). Once this steric limit is reached, the EDL profile grows in thickness away from the OHP with a constant density of counter-ions (cations in this case). Therefore,

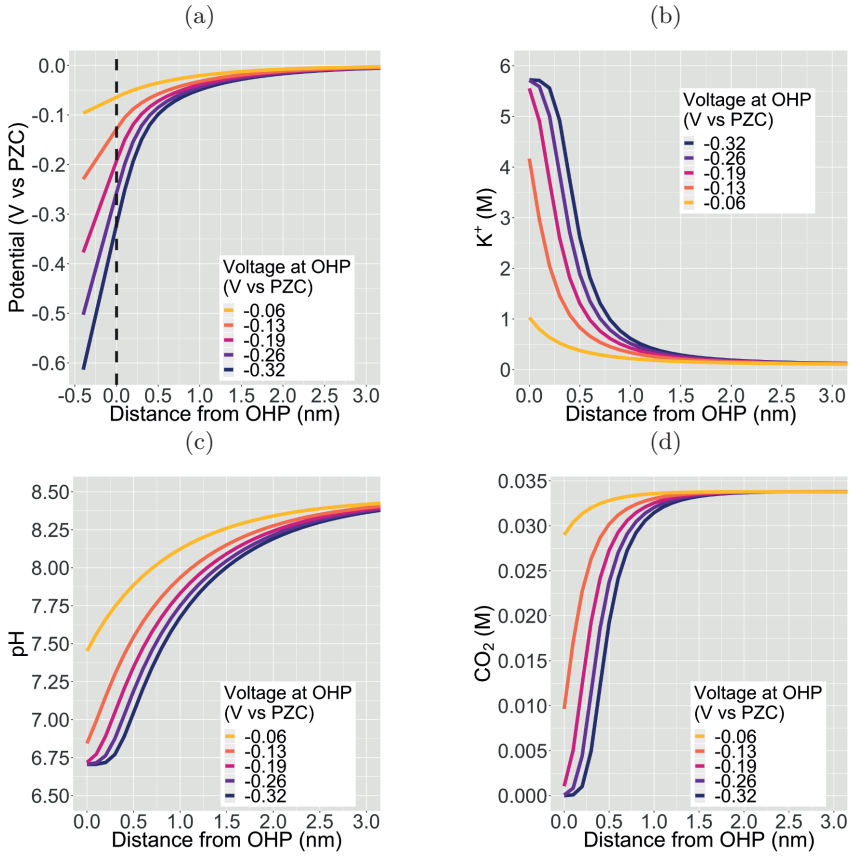

Figure 5.2: The electrical double layer (EDL) facing a planar eCO_2R catalyst for a 0.1 M $KHCO_3$ electrolyte solution saturated with CO_2. The above results are derived for a total current density of 1 mA/cm^2 and a CO Faradaic efficiency of 0.8. PZC stands for the potential of point of zero charge of the planar catalyst surface and x=-0.4nm is the catalyst surface and x=0 is the OHP (grey dotted line in (a)). The plots (b), (c) and (d) start at x=0 since the OHP marks the plane of closest approach to the catalyst for the solvated solution species.

at higher voltages relative to ϕ_T, the nature of the EDL can no longer be described as a diffuse-layer, but rather, it assumes the form of a condensed layer of counter-ions which builds in thickness with applied potential [19]. We will discuss our results in the context of the impact of the condensed double layer on CO_2 transport in section 5.2.1 and the pH in section 5.2.2. Section 5.2.3 discusses the impact of changing the alkali metal type in the

electrolyte on the nature of the EDL.

5.2.1. Influence of EDL on CO_2

The first important aspect of the build-up of counter-ions in the EDL at higher potentials is the accessibility of the catalyst surface for the CO_2 molecule. The rate at which CO_2 can diffuse to the catalyst surface, puts an upper limit to the activity that is achievable through catalysis and is therefore a critical parameter for eCO_2R performance. The diminishing of CO_2 concentration in the EDL at high applied voltages (Figure 5.2d) is a direct consequence of the steric effect incorporated in the GMPNP model. Figure 5.3 shows a comparison between the concentration profiles in the EDL obtained using a reaction-diffusion model, a PNP model which solves the migration, diffusion and reaction processes self-consistently but assumes point species and a GMPNP model which corrects the PNP for steric effects. It is evident that inclusion of migration in the PNP and GMPNP models drastically influences the activity of charged species in the EDL region. The volume exclusion in the GMPNP model has important consequences for the extent of cation concentration at the OHP which, for the PNP model, reach unphysical high concentrations (significantly higher than the steric limit, Figure 5.3b). Despite a very high cation accumulation at the OHP for the PNP model, the assumption of point species results in no exclusion of CO_2 from the EDL region as is predicted by the GMPNP model (Figure 5.3d). The minor variation between the CO_2 concentration profiles derived using the RD and PNP models stems from the significant difference in the OH^- concentrations (Figure 5.3a) leading to the formation of bicarbonate through the homogeneous reaction (5.8). These results highlight the importance of considering volume-exclusion in mass transport models attempting to resolve the EDL in electrocatalytic systems such as eCO_2R.

According to Figure 5.2d, the CO_2 concentration is completely depleted at potentials more cathodic than ~-0.2 V vs PZC at the OHP. Since there is no experimental evidence suggesting that CO_2 reduction completely terminates at high applied potentials, the result in Figure 5.2d leads us to the hypothesis that the CO_2 molecule diffuses to the catalyst surface at high applied potentials due to many-body correlations in the presence of the solvated cations in the EDL region, albeit with

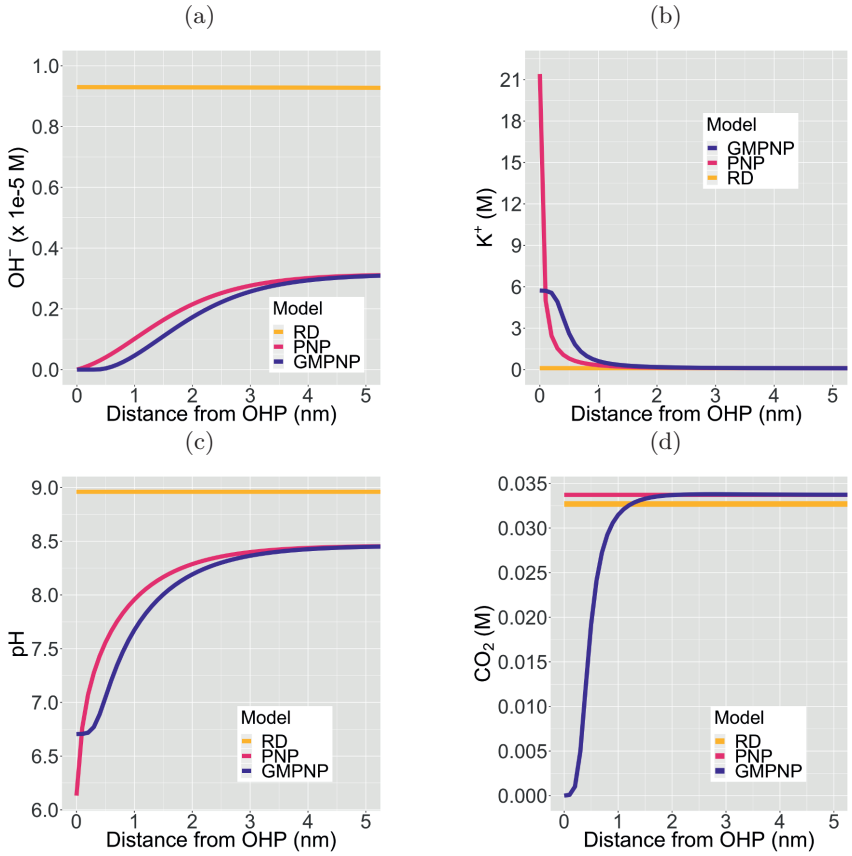

Figure 5.3: Comparison between results obtained from reaction-diffusion (RD) model, a Poisson-Nernst-Planck (PNP) model and a generalized modified PNP (GMPNP) model for the EDL region. x=0 is located at the OHP. All results have been derived for a total current density of 1 mA/cm^2 and a CO Faradaic efficiency of 0.8. The PNP and GMPNP results are for a voltage of -0.32 V vs PZC at the OHP.

a diminished diffusivity due the condensed nature of the EDL. Complex many-body correlations arising from the mutual interaction of chemical species (including water molecules) are expected to play a role especially in the EDL with a high concentration of counter-ions and the presence of competing electrostatic and van der Waals forces. In addition, the identity of the solvated cation should also have an influence on the rate of diffusion of CO_2. Cations have been shown to influence the CO_2 reduc-

tion rate through numerous experimental as well as computational studies [3, 4, 13, 40–45] however, this influence has not been studied from the perspective of changing diffusion coefficient of the CO_2 molecule. The modeling results presented in this study use Fick's law of diffusion with constant values of diffusion coefficients for all species (Fick diffusivity values are tabulated in table B.2 in Appendix B). The EDL is however a multi-component non-dilute solution where considerable deviations from the Fick's diffusivities can be expected due to non-ideal behavior. We are currently conducting force-field molecular dynamics (MD) simulations to study the diffusion of CO_2 in such an EDL environment. The effect of cation type will be discussed further in the context of Figure 5.6 later in the text.

The other possibility is that the reduction of CO_2 (at least the first reduction step) happens beyond the condensed layer of counter-ions at the EDL and not directly at catalyst surface. We believe that it is highly unlikely that all the CO_2 reduction steps occur at the EDL as it would not be able to explain the major deviation between the CO_2 reduction products amongst different metallic catalysts [46]. However, the involvement of the solvated cations in the reduction of CO_2 could be one of the reasons for the difference in performance of systems using different cation types. *Ab-initio* quantum-mechanical methods need be developed to study the first CO_2 reduction step in the presence of the condensed EDL to compare the energetics of the potential pathways.

5.2.2. Influence of EDL on pH

The second important consequence of the formation of the EDL is the drop in pH in the double layer region due to both, a higher concentration of positively charged H^+, and a depletion of negatively charged OH^- from the region measuring a few nm from the electrode surface (Figures 5.2c and S2a). The pH at the OHP drops to a threshold value and the profile extends into the double layer region at higher voltages analogous to what is observed for the accumulation of the K^+ ions in Figure 5.2b. Assuming point species and not considering volume exclusion within the PNP model, leads to an unphysical low pH value at the OHP (Figure 5.3c). Figures 5.4a - 5.4d show the pH and OH^- concentration profiles for varying values of total current densities at a fixed potential and Faradaic efficiency dis-

(a) GMPNP: EDL

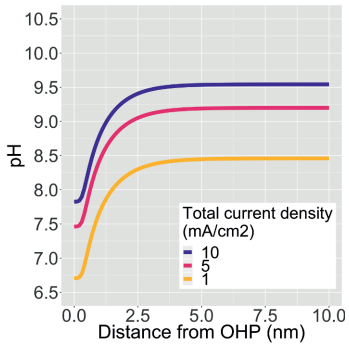

(b) GMPNP: EDL

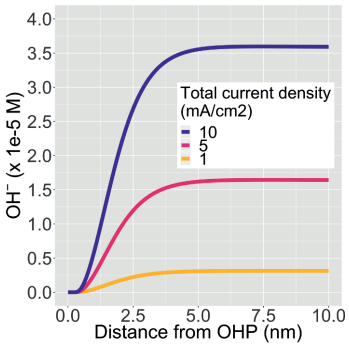

(c) GMPNP: Full domain

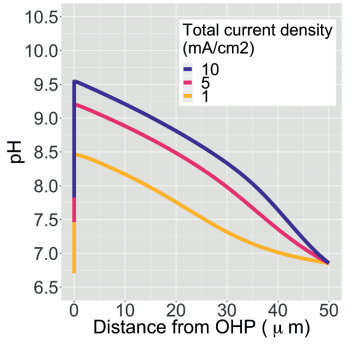

(d) GMPNP: Full domain

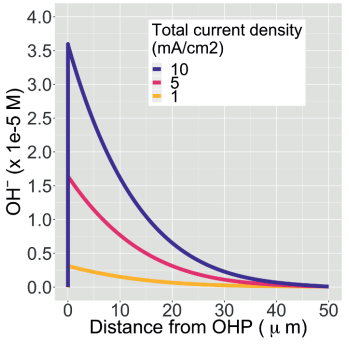

(e) RD: Full domain

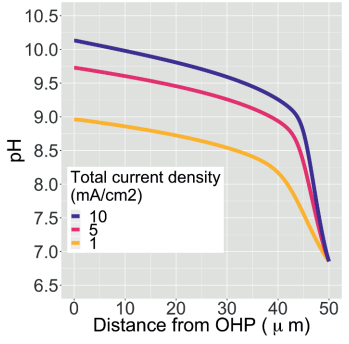

(f) RD: Full domain

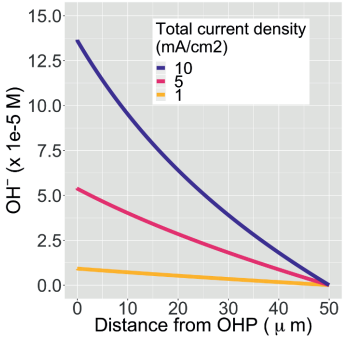

Figure 5.4: Influence of total current density on pH and OH^- concentration. Figures (a) and (b) show the profiles for a region of 10 nm from the OHP whereas Figures (c) and (d) show the profiles for the entire Nernst layer extending to 50 μm, all derived using GMPNP. Figures (e) and (f) show results obtained using reaction-diffusion (RD) model for the purpose of comparison. All results are calculated for a CO Faradaic efficiency of 0.8 and the GMPNP results are for a potential of -0.32 V vs PZC at the OHP.

tribution computed using the GMPNP model. The results obtained using the reaction-diffusion (RD) model are shown in Figures 5.4e and 5.4f for comparison.

As expected, the pH at the OHP as well as at its peak value are found to be proportional to the total current density and the pH attains a maximum value beyond the EDL at a distance of ~5 nm from the OHP (Figures 5.4a and 5.4c). The RD model predicts a considerably higher pH at x=0 and also, as expected, does not capture the drop in the pH due to migration effects very close to the electrode surface as predicted by the GMPNP model (also see Figure 5.3c). Similarly, the OH^- concentration calculated using GMPNP is completely depleted at the OHP at high voltages (Figures 5.4b and S2a) whereas the peak value beyond the EDL is proportional to the total current density. The RD model however, predicts a ~4 times higher rise in OH^- concentration at the electrode relative to the peak value predicted by GMPNP and does not account for its depletion due to electrostatic repulsion in the EDL (also see Figure 5.3a). We have also considered a limiting proton current case where no more than 10% of the bulk concentration of H^+ is allowed to accumulate at the OHP and the protons get consumed via the catalytic reactions (B.14) and (B.15) in Appendix B. Adding the flux of protons at the catalyst surface leads to the pH profiles for all current densities to overlap and a pH value of 8 is obtained at the OHP with a maximum value of ~9.7 beyond the EDL (Figure B.5 in Appendix B). The current attributed to the H^+ flux for H_2 and CO production is <0.5% of the total current density for all cases considered.

Numerous studies of eCO_2R systems have shown a strong correlation between pH of the electrolyte in the vicinity of the catalyst (or the so-called local pH) and the overall performance, especially the catalyst selectivity [28, 47–53]. Our results demonstrate that the EDL leads to pH and OH^- concentration profiles which do not monotonically increase towards the catalyst surface but in fact, become considerably diminished in the immediate vicinity of the OHP up to a distance of ~5 nm. Since the OH^- concentration is depleted from the EDL region, the pH at the OHP at high applied potentials will have a stronger dependence on the rate of H^+ consumption in catalytic processes than the total current density. Therefore, we believe that there is a strong need to explicitly define what is meant by the term 'local' in the context of pH and concentrations of solution species

when discussing mechanistic insights and relative performance of eCO_2R systems.

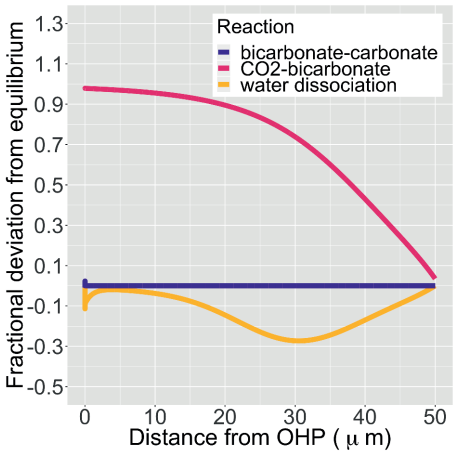

Figure 5.5: Fractional deviation from equilibrium for reactions (5.6), (5.7) and (5.8) in the simulation domain. The data shown is for a total current density of 1 mA/cm^2, a CO Faradaic efficiency of 0.8 and a potential of -0.32 V vs PZC at the OHP. We have removed the deviation values for the initial 1 nm from the OHP since the formation of the EDL wildly distorts the species concentrations.

In addition, Figure 5.5 shows the extent of the deviation of homogeneous reactions (5.6), (5.7) and (5.8) from equilibrium at steady-state as defined by the equations (B.11), (B.12) and (B.13) in Appendix B. The buffer reaction of CO_2 to HCO_3^- (reaction (5.8)) is too slow to reach equilibrium and is deficient of HCO_3^- in the entire Nernst domain. Therefore even though the concentration of OH^- rises due to eCO_2R, the competing rates of diffusion and reaction kinetics imply that CO_2 is still present in excess in reaction (5.8). This is in line to what has been shown previously using spectroscopic measurements [54]. The HCO_3^- to CO_3^{2-} buffer reaction (reaction (5.7)) remains in equilibrium in the entire domain outside the EDL which is expected considering that k_{a1} is 6 order of magnitudes bigger than k_{b1}. The water-dissociation reaction (reaction (5.6)) also deviates from its equilibrium due to competing reaction and mass transport rates. It should be noted that the results shown in Figure 5.5 remain qualitatively similar even if a reaction-diffusion model is considered. The dramatic variation of the pH profile as a function of distance from the

OHP (Figure 5.4c) as well as the deviation of the buffer reactions from their equilibrium are important factors that should be considered in experimental studies aiming to measure pH in eCO_2R systems using for e.g. spectroscopic techniques [55].

5.2.3. Influence of cation size

Finally, we consider the effect of changing the type of cation in the electrolyte solution. We compare Cs^+, K^+, Na^+ and Li^+ while keeping the composition of the other species in the bulk electrolyte the same.

In the context of the GMPNP simulations, the cations (i) differ in terms of their solvated size (a_i in equation (5.10)) and the hydration number of each ion (w_i in equation (5.12)) (the values of both parameters for each cation can be found in tables B.2 and B.2 in Appendix B, respectively). The trend of solvated sizes of the cations in an aqueous solution follows the order $Cs^+<K^+<Na^+<Li^+$ which is the inverse of the trend for the neutral atoms due to difference in the hydration properties amongst the alkali metal cations [56, 57]. Figure B.6 in Appendix B shows an illustration of the effect of cations with different sizes on the concentration at the steric limit and the thickness of the EDL. This can be used to understand the difference in concentration profiles of the cations in the EDL as shown in Figure 5.6a, with Cs^+ being the smallest solvated cation reaching the highest concentration at the OHP followed very closely by K^+ with a similar solvated size, followed by Na^+ and Li^+ in that order. The resulting trend in the electric field strength at the OHP is shown in Figure 5.6b.

Despite reaching a higher concentration at the OHP and therefore a higher charge density, the electric field strength for Cs^+ is found to be weaker as compared to K^+. This is due to the fact that Cs^+ polarizes fewer water molecules compared to the other alkali metal cations and therefore the drop in relative permittivity of the solution at the OHP is smaller based on the equation (5.12) (see Figure S7a). Multiple experimental results have shown Cs^+ to benefit the activation of CO_2 relative to other cation types [3, 40, 42–44]. The electric field strength close to the cathode surface in the presence of the cations has been regarded as an important factor leading to the observed experimental results owing to the interaction of the field with the adsorbed polar reactive species [3, 4, 13, 42]. However, based

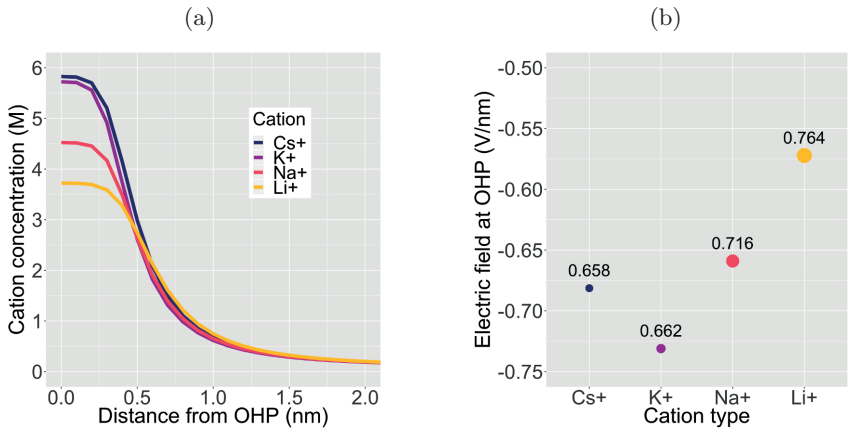

Figure 5.6: Effect of cation size on the properties of the EDL. Calculations are performed for a potential of -0.32 V vs PZC at the OHP for a total current density of 1 mA/cm^2 and a CO Faradaic efficiency of 0.8. The size of the data points in (b) are proportional to the size of the respective solvated cations which is mentioned in nm adjacent to the data points.

on our results, we believe that the observed improvement in the reduction of CO_2 in the presence of Cs^+ cannot be understood solely on the basis of electric field strength. The specific ion interactions of the cation with the surrounding water and the CO_2, as well as with the charged metal surface, also need to be taken into account.

5.3. Discussion

The reaction environment of the CO_2 electrochemical reduction process is highly complex with several coupled phenomena operating at vastly varying length and time scales that incorporate important degrees of freedom for the overall system performance. A multi-scale approach is therefore essential in order for computational simulations to effectively develop the understanding of such a reaction system to compliment the experimental efforts in the area.

Ab-initio calculations of the double layer suffer from several limitations that lead to unfeasible computational costs which can be circumvented in the continuum treatment of the double layer [58–60]. In addition, the re-

sults derived using a continuum approach such as the GMPNP can provide valuable inputs to atomistic quantum mechanical models by defining the steady-state environment under which reaction energetics need to be studied [13, 61]. However, the continuum treatment of the electrolyte system does not capture effects pertaining to ion specificity which can potentially play a role at molecular length scales and concentrations relevant in the EDL for highly charged surfaces such as in the case of eCO_2R [62–65]. The Bjerrum length ($l_B = e^2/4\pi\epsilon_r\epsilon_0 k_B T$, 0.7 nm at room temperature) defines the length scale at which the electrostatic interaction between two charged species is comparable to the thermal energy $k_B T$. The relative permittivity of the electrolyte can decrease drastically in the EDL where the electric field strength is high (Figure S2) [32, 33]. This will lead to an increase in the Bjerrum length indicating a prevalence of ion-specific effects. A promising approach to account for particle correlations in the EDL uses density functional theory (DFT) to estimate excess chemical potentials of species at equilibrium which can be used as an input to continuum models such as PNP to study transport [66, 67]. In addition, our results represent the nature of the double layer in the absence of specific short-range electrostatic interactions between the electrode surface and the solution species. The presence of specific adsorption can add significant complexity to the EDL description as it can influence the potential at the PZC, the balance of charge between the metal surface and the double layer and consequently the potential and concentration profiles at a given applied potential [61, 68]. There is a need to develop computational frameworks applicable to practical CO_2 electrocatalytic systems with high surface charge densities, multiple components, long-range concentration gradients and specific adsorption that correct the mean-field continuum dynamics of the double-layer in a computationally and numerically tractable manner.

In addition to theoretical challenges, a more practical challenge arises from solving the (GM)PNP system of partial difference equations numerically at operating potentials. The Galerkin finite element method is found to be unstable for typical values of applied potentials unless a very fine time and space discretization is used to resolve the EDL region. The SUPG method was used in this study to stabilize the PNP system as described in section 5.1.3. However, there is still a need to develop stabilization techniques suited for the modified version of the Nernst-Planck equation

with a non-linear volume exclusion term added. The development of better stabilization techniques will go a long way in making the application of the GMPNP system more feasible to a wider array of operating conditions for electrocatalytic systems of relevance.

5.4. Conclusions

Our results establish the importance of electrostatic forces and volume exclusion in the determination of the reaction environment for CO_2 electrocatalysis. The electrical double layer formed as a consequence will be highly influential for the access of the catalyst to the reactive species, both CO_2 and H^+, and will therefore play a role in the activity as well as selectivity of the process.

The defining characteristic of the EDL is the screening of the charge density on the cathode surface with solvated cations in the electrolyte and a concomitant repulsion of anions away from the surface. The nature of the cation therefore plays an important role in determining the structure of the EDL, the strength of electric field, the differential capacitance and the extent of the polarization of solvent molecules. The operating potentials of practical eCO_2R and other electrocatalytic systems imply that the cations in the EDL will reach their steric limit close to the electrode. This closed-pack nature of the EDL is expected to have significant implications for the energetics of the reactive and non-reactive processes relevant to eCO_2R. The local reaction environment of CO_2 electrocatalysis is therefore formed by the double layer and more research effort is needed to develop a stronger understanding of the region spanning the first 5 - 10 nm from the catalyst surface.

As all catalysts of practical relevance to eCO_2R have a nano and meso-structure, the effect of mass transport is expected to be even more complex and significant in the presence of nanometer scale pores and confinements [2, 69]. Nanopores and channels with sizes less than twice the potential screening length can have overlapping double layers which can lead to interesting effects due to selective ion enrichment and depletion with several practical applications [62, 70]. Nanostructuring is therefore a very important tool to influence the reaction environment and thus the performance of the catalyst. Unlike a planar surface, the distribution of charge density

over a structured surface will be non-uniform and will lead to a varying double layer structure across the catalyst. Application of models such as the GMPNP in higher dimensions can then be very useful to study such phenomena. Gas diffusion electrode (GDE) based eCO_2R systems employing nanostructured catalyst layers and significantly shorter diffusion length of CO_2 have achieved considerably higher current densities and enhanced selectivity through better mass transport [6, 7]. Electrified porous catalysts therefore are a very practically relevant class of systems where continuum modeling approach similar to the one presented here can play an important role.

In conclusion, the continuum treatment of the GMPNP equations provides a computationally tractable method to model the reaction environment of eCO_2R close to highly charged surfaces, although with certain limitations. We believe that our approach can provide a qualitatively sound starting point for further theoretical as well as experimental investigations while bridging some of the gap between quantum mechanical surface reactivity studies and mass transport of species from the bulk solution in electrocatalytic systems.

References

[1] D. Bohra, J. H. Chaudhry, T. Burdyny, E. A. Pidko, and W. A. Smith, *Modeling the electrical double layer to understand the reaction environment in a CO_2 electrocatalytic system,* Energy Environ. Sci. **12**, 3380 (2019).

[2] G. O. Larrazábal, A. J. Martín, and J. Pérez-Ramírez, *Building Blocks for High Performance in Electrocatalytic CO_2 Reduction: Materials, Optimization Strategies, and Device Engineering,* The Journal of Physical Chemistry Letters **8**, 3933 (2017).

[3] J. Resasco, L. D. Chen, E. Clark, C. Tsai, C. Hahn, T. F. Jaramillo, K. Chan, and A. T. Bell, *Promoter effects of alkali metal cations on the electrochemical reduction of carbon dioxide,* Journal of the American Chemical Society **139**, 11277 (2017), pMID: 28738673.

[4] M. Liu, Y. Pang, B. Zhang, P. De Luna, O. Voznyy, J. Xu, X. Zheng, C. T. Dinh, F. Fan, C. Cao, F. P. G. de Arquer, T. S. Safaei, A. Mepham, A. Klinkova, E. Kumacheva, T. Filleter, D. Sinton, S. O.

Kelley, and E. H. Sargent, *Enhanced electrocatalytic CO_2 reduction via field-induced reagent concentration,* Nature **537**, 382 EP (2016).

[5] M. G. Kibria, J. P. Edwards, C. M. Gabardo, C.-T. Dinh, A. Seifitokaldani, D. Sinton, and E. H. Sargent, *Electrochemical CO_2 reduction into chemical feedstocks: From mechanistic electrocatalysis models to system design,* Advanced Materials **0**, 1807166 (2019).

[6] T. Burdyny and W. A. Smith, *CO_2 reduction on gas-diffusion electrodes and why catalytic performance must be assessed at commercially-relevant conditions,* Energy Environ. Sci. **12**, 1442 (2019).

[7] C.-T. Dinh, T. Burdyny, M. G. Kibria, A. Seifitokaldani, C. M. Gabardo, F. P. García de Arquer, A. Kiani, J. P. Edwards, P. De Luna, O. S. Bushuyev, C. Zou, R. Quintero-Bermudez, Y. Pang, D. Sinton, and E. H. Sargent, *CO_2 electroreduction to ethylene via hydroxide-mediated copper catalysis at an abrupt interface,* Science **360**, 783 (2018).

[8] N. Gupta, M. Gattrell, and B. MacDougall, *Calculation for the cathode surface concentrations in the electrochemical reduction of CO_2 in $KHCO_3$ solutions,* Journal of Applied Electrochemistry **36**, 161 (2006).

[9] D. Raciti, M. Mao, and C. Wang, *Mass transport modelling for the electroreduction of CO_2 on Cu nanowires,* Nanotechnology **29**, 044001 (2018).

[10] H. Hashiba, L.-C. Weng, Y. Chen, H. K. Sato, S. Yotsuhashi, C. Xiang, and A. Z. Weber, *Effects of electrolyte buffer capacity on surface reactant species and the reaction rate of CO_2 in electrochemical CO_2 reduction,* The Journal of Physical Chemistry C **122**, 3719 (2018).

[11] C. Delacourt, P. L. Ridgway, and J. Newman, *Mathematical modeling of CO_2 reduction to CO in aqueous electrolytes i. Kinetic study on planar silver and gold electrodes,* J. Electrochem. Soc. **157**, B1902 (2010).

[12] S. Suter and S. Haussener, *Optimizing mesostructured silver catalysts for selective carbon dioxide conversion into fuels,* Energy Environ. Sci. **12**, 1668 (2019).

[13] S. Ringe, E. L. Clark, J. Resasco, A. Walton, B. Seger, A. T. Bell, and K. Chan, *Understanding cation effects in electrochemical CO_2 reduction,* Energy Environ. Sci. , 10.1039/C9EE01341E (2019).

[14] M. S. Kilic, M. Z. Bazant, and A. Ajdari, *Steric effects in the dynamics of electrolytes at large applied voltages. II. Modified Poisson-Nernst-Planck equations,* Phys. Rev. E **75**, 021503 (2007).

[15] Gouy, M., *Sur la constitution de la charge électrique à la surface d'un électrolyte,* J. Phys. Theor. Appl. **9**, 457 (1910).

[16] D. L. Chapman, *LI. A contribution to the theory of electrocapillarity,* The London, Edinburgh, and Dublin Philosophical Magazine and Journal of Science **25**, 475 (1913).

[17] J. Newman and K. E. Thomas-Alyea, *Electrochemical Systems*, 3rd ed. (John Wiley & Sons, 2004).

[18] J. Lyklema, *Fundamentals of interface and colloid science. Volume 2: Solid-liquid interfaces. With special contributions by A. de Keizer, B.H. Bijsterbosch, G.J. Fleer and M.A. Cohen Stuart.* (Academic Press, 1995) pp. –.

[19] M. S. Kilic, M. Z. Bazant, and A. Ajdari, *Steric effects in the dynamics of electrolytes at large applied voltages. I. Double-layer charging,* Phys. Rev. E **75**, 021502 (2007).

[20] L. Pilon, H. Wang, and A. d'Entremont, *Recent advances in continuum modeling of interfacial and transport phenomena in electric double layer capacitors,* J. Electrochem. Soc. **162**, A5158 (2015).

[21] H. Wang, A. Thiele, and L. Pilon, *Simulations of cyclic voltammetry for electric double layers in asymmetric electrolytes: A generalized modified Poisson-Nernst-Planck model,* The Journal of Physical Chemistry C **117**, 18286 (2013).

[22] M. Z. Bazant, M. S. Kilic, B. D. Storey, and A. Ajdari, *Towards an understanding of induced-charge electrokinetics at large applied voltages in concentrated solutions,* Advances in Colloid and Interface Science **152**, 48 (2009).

[23] I. Borukhov, D. Andelman, and H. Orland, *Steric effects in electrolytes: A modified Poisson-Boltzmann equation,* Phys. Rev. Lett. **79**, 435 (1997).

[24] A. Iglic and V. Kralj-Iglic, *Influence of finite size of ions on electrostatic properties of electric double layer,* Electrotecnical Rev. (Slovenia) **61**, 127 (1994).

[25] O. Stern, *Zur theorie der elektrolytischen doppelschicht,* Zeitschrift für Elektrochemie und angewandte physikalische Chemie **30**, 508 (1924).

[26] H. Helmholtz, *Studien über electrische grenzschichten,* Annalen der Physik **243**, 337 (1879).

[27] S. Weisenberger and A. Schumpe, *Estimation of gas solubilities in salt solutions at temperatures from 273 K to 363 K,* AIChE Journal **42**, 298 (1996).

[28] T. Burdyny, P. J. Graham, Y. Pang, C.-T. Dinh, M. Liu, E. H. Sargent, and D. Sinton, *Nanomorphology-enhanced gas-evolution intensifies CO_2 reduction electrochemistry,* ACS Sustainable Chemistry & Engineering **5**, 4031 (2017).

[29] S. Trasatti and E. Lust, *The potential of zero charge,* in *Modern Aspects of Electrochemistry*, edited by R. E. White, J. O. Bockris, and B. E. Conway (Springer US, Boston, MA, 1999) pp. 1–215.

[30] J. B. Hasted, D. M. Ritson, and C. H. Collie, *Dielectric properties of aqueous ionic solutions. Parts I and II,* The Journal of Chemical Physics **16**, 1 (1948).

[31] J. O. Bockris and A. K. Reddy, *Volume 1: Modern Electrochemistry*, 2nd ed. (Springer US, 1998).

[32] F. Booth, *The dielectric constant of water and the saturation effect,* The Journal of Chemical Physics **19**, 391 (1951).

[33] A. J. Appleby, *Electron transfer reactions with and without ion transfer,* in *Modern Aspects of Electrochemistry*, edited by B. E. Conway, C. G. Vayenas, R. E. White, and M. E. Gamboa-Adelco (Springer US, Boston, MA, 2005) pp. 175–301.

[34] M. S. Alnæs, J. Blechta, J. Hake, A. Johansson, B. Kehlet, A. Logg, C. Richardson, J. Ring, M. E. Rognes, and G. N. Wells, *The FEniCS project version 1.5,* Archive of Numerical Software **3**, 9 (2015).

[35] A. Logg, K.-A. Mardal, G. N. Wells, *et al.*, *Automated Solution of Differential Equations by the Finite Element Method* (Springer, 2012).

[36] J. H. Chaudhry, J. Comer, A. Aksimentiev, and L. N. Olson, *A stabilized finite element method for modified Poisson-Nernst-Planck equations to determine ion flow through a nanopore,* Communications in Computational Physics **15**, 93 (2014).

[37] P. B. Bochev, M. D. Gunzburger, and J. N. Shadid, *Stability of the SUPG finite element method for transient advection-diffusion problems,* Computer Methods in Applied Mechanics and Engineering **193**, 2301 (2004).

[38] T. J. Hughes, L. P. Franca, and G. M. Hulbert, *A new finite element formulation for computational fluid dynamics: VIII. The galerkin/least-squares method for advective-diffusive equations,* Computer Methods in Applied Mechanics and Engineering **73**, 173 (1989).

[39] L. P. Franca, S. L. Frey, and T. J. Hughes, *Stabilized finite element methods: I. Application to the advective-diffusive model,* Computer Methods in Applied Mechanics and Engineering **95**, 253 (1992).

[40] M. R. Singh, Y. Kwon, Y. Lum, J. W. Ager, and A. T. Bell, *Hydrolysis of electrolyte cations enhances the electrochemical reduction of CO_2 over Ag and Cu,* Journal of the American Chemical Society **138**, 13006 (2016), pMID: 27626299.

[41] C. X. Zhao, Y. F. Bu, W. Gao, and Q. Jiang, *CO_2 reduction mechanism on the Pb(111) surface: Effect of solvent and cations,* The Journal of Physical Chemistry C **121**, 19767 (2017).

[42] A. Murata and Y. Hori, *Product selectivity affected by cationic species in electrochemical reduction of CO_2 and CO at a Cu electrode,* Bulletin of the Chemical Society of Japan **64**, 123 (1991).

[43] M. R. Thorsona, K. I. Siila, and P. J. A. Kenis, *Effect of cations on the electrochemical conversion of CO_2 to CO,* J. Electrochem. Soc. **160**, F69 (2013).

[44] C. M. Gunathunge, V. J. Ovalle, and M. M. Waegele, *Probing promoting effects of alkali cations on the reduction of CO at the aqueous electrolyte/copper interface,* Phys. Chem. Chem. Phys. **19**, 30166 (2017).

[45] L. D. Chen, M. Urushihara, K. Chan, and J. K. Nørskov, *Electric field effects in electrochemical CO_2 reduction,* ACS Catalysis **6**, 7133 (2016).

[46] Y. Hori, *Electrochemical CO_2 reduction on metal electrodes,* in *Modern Aspects of Electrochemistry*, edited by C. G. Vayenas, R. E. White, and M. E. Gamboa-Aldeco (Springer New York, New York, NY, 2008) pp. 89–189.

[47] S. Lee, S. Hong, and J. Lee, *Bulk pH contribution to CO/$HCOO^-$ production from CO_2 on oxygen-evacuated Cu_2O electrocatalyst,* Catalysis Today **288**, 11 (2017), electrochemical Reduction of Carbon Dioxide by heterogenous and homogeneous catalysts: Experiment and Theory.

[48] M. Ma, B. J. Trześniewski, J. Xie, and W. A. Smith, *Selective and efficient reduction of carbon dioxide to carbon monoxide on oxide-derived nanostructured silver electrocatalysts,* Angewandte Chemie International Edition **55**, 9748 (2016).

[49] K. J. P. Schouten, E. P. Gallent, and M. T. Koper, *The influence of pH on the reduction of CO and CO_2 to hydrocarbons on copper electrodes,* Journal of Electroanalytical Chemistry **716**, 53 (2014), special Issue in Honour of Kingo Itaya.

[50] M. Ma, K. Djanashvili, and W. A. Smith, *Controllable hydrocarbon formation from the electrochemical reduction of CO_2 over Cu*

nanowire arrays, Angewandte Chemie International Edition **55**, 6680 (2016).

[51] R. Kas, R. Kortlever, H. Yilmaz, M. T. M. Koper, and G. Mul, *Manipulating the hydrocarbon selectivity of copper nanoparticles in CO_2 electroreduction by process conditions,* ChemElectroChem **2**, 354 (2015).

[52] A. S. Varela, M. Kroschel, T. Reier, and P. Strasser, *Controlling the selectivity of CO_2 electroreduction on copper: The effect of the electrolyte concentration and the importance of the local pH,* Catalysis Today **260**, 8 (2016), surface Analysis and Dynamics (SAND).

[53] Y. Hori, A. Murata, and R. Takahashi, *Formation of hydrocarbons in the electrochemical reduction of carbon dioxide at a copper electrode in aqueous solution,* J. Chem. Soc., Faraday Trans. 1 **85**, 2309 (1989).

[54] M. Dunwell, X. Yang, B. P. Setzler, J. Anibal, Y. Yan, and B. Xu, *Examination of near-electrode concentration gradients and kinetic impacts on the electrochemical reduction of CO_2 using surface-enhanced infrared spectroscopy,* ACS Catalysis **8**, 3999 (2018).

[55] O. Ayemoba and A. Cuesta, *Spectroscopic evidence of size-dependent buffering of interfacial pH by cation hydrolysis during CO_2 electroreduction,* ACS Applied Materials & Interfaces **9**, 27377 (2017), pMID: 28796478.

[56] E. R. Nightingale, *Phenomenological theory of ion solvation. Effective radii of hydrated ions,* The Journal of Physical Chemistry **63**, 1381 (1959).

[57] J. O. Bockris and P. P. S. Saluja, *Ionic solvation numbers from compressibilities and ionic vibration potentials measurements,* The Journal of Physical Chemistry **76**, 2140 (1972).

[58] A. Asthagiri and M. J. Janik, eds., *Computational Catalysis*, Catalysis Series (The Royal Society of Chemistry, 2014) pp. 116 – 156.

[59] J. A. Gauthier, S. Ringe, C. F. Dickens, A. J. Garza, A. T. Bell, M. Head-Gordon, J. K. Nørskov, and K. Chan, *Challenges in modeling electrochemical reaction energetics with polarizable continuum models,* ACS Catalysis **9**, 920 (2019).

[60] F. Nattino, M. Truscott, N. Marzari, and O. Andreussi, *Continuum models of the electrochemical diffuse layer in electronic-structure calculations,* The Journal of Chemical Physics **150**, 041722 (2019).

[61] A. Baskin and D. Prendergast, *Improving continuum models to define practical limits for molecular models of electrified interfaces,* J. Electrochem. Soc. **164**, E3438 (2017).

[62] L. Bocquet and E. Charlaix, *Nanofluidics, from bulk to interfaces,* Chem. Soc. Rev. **39**, 1073 (2010).

[63] W. Kunz, P. L. Nostro, and B. Ninham, *The present state of affairs with Hofmeister effects,* Current Opinion in Colloid & Interface Science **9**, 1 (2004).

[64] B. W. Ninham and V. Yaminsky, *Ion binding and ion specificity: The Hofmeister effect and Onsager and Lifshitz theories,* Langmuir **13**, 2097 (1997).

[65] P. Attard, *Electrolytes and the electric double layer,* in *Advances in Chemical Physics* (John Wiley & Sons, Ltd, 2007) pp. 1–159.

[66] D. Gillespie, W. Nonner, and R. S. Eisenberg, *Coupling Poisson-Nernst-Planck and density functional theory to calculate ion flux,* Journal of Physics: Condensed Matter **14**, 12129 (2002).

[67] A. Voukadinova, M. Valiskó, and D. Gillespie, *Assessing the accuracy of three classical density functional theories of the electrical double layer,* Phys. Rev. E **98**, 012116 (2018).

[68] A. Bard and L. Faulkner, *Electrochemical Methods: Fundamentals and Applications*, Vol. 6 (John Wiley & Sons, Inc., 2001).

[69] J. H. Bae, J.-H. Han, and T. D. Chung, *Electrochemistry at nanoporous interfaces: new opportunity for electrocatalysis,* Phys. Chem. Chem. Phys. **14**, 448 (2012).

[70] R. B. Schoch, J. Han, and P. Renaud, *Transport phenomena in nanofluidics,* Rev. Mod. Phys. **80**, 839 (2008).

6

Mass transport in GDE catalytic pores

Divya Bohra, Thomas Burdyny, Jehanzeb H. Chaudhry, Evgeny A. Pidko, Wilson A. Smith

GDE-based setups have shown promising performance for CO_2 electrocatalysis and further development of these systems will be important on the path to industrial feasibility. In this chapter, we model an effective catalyst pore within a flow-cell to study the influence of the catalyst structure and operating conditions on the reaction environment for CO_2 electrocatalysis at practically relevant current densities. We show that the length of the catalyst pore as well as the boundary conditions at the gas-electrolyte and electrolyte-electrolyte interfaces across this length are highly influential parameters for determining the conditions within the catalyst pore. Pores with the same catalytic surface area can have very different reaction environments depending primarily on the pore length and not the pore radius. Properties such as electrolyte pH and buffer breakdown, ionic strength and CO_2 concentration are sensitive to the catalyst layer thickness, gas pressure, electrolyte flow rate and the flow-channel geometry. The applied potential impacts the concentration of ionic species in the pore, which in turn determines the solubility of CO_2 available for

the reaction. Our results underline the need to understand and manage transport within GDE-based electrocatalysis systems as an essential means to control catalyst performance. Benchmarking of GDE-based electrocatalytic systems against their structural and operational parameters will be important for achieving improvements in performance that can be ultimately translated to large-scale operation.

The results in this chapter are currently under preparation for publication.

Research work led by Divya Bohra; Jehanzeb H. Chaudhry provided guidance for the numerical simulations; Thomas Burdyny provided guidance for the GDE model definition; Evgeny A. Pidko played supervisory role; Wilson A. Smith supervised the project as the principal investigator.

6.1. Gas diffusion electrode-based eCO_2R systems

The solubility of carbon dioxide (CO_2) in aqueous electrolytes under ambient conditions is ~33 mM. In a system design where the electrolyte is saturated with dissolved CO_2, mass transport limits the achievable CO_2 reduction current density to below 50 mA/cm^2 irrespective of the nature of the catalyst employed [1–11]. In order for the process to be economically feasible, a minimum threshold current density of ~200 mA/cm^2 is estimated to be required in addition to the selectivity, over-potential and stability targets [12–14]. Gas diffusion electrodes (GDE) based cell designs have been demonstrated to successfully overcome this mass transfer limitation in eCO_2R systems [15–21].

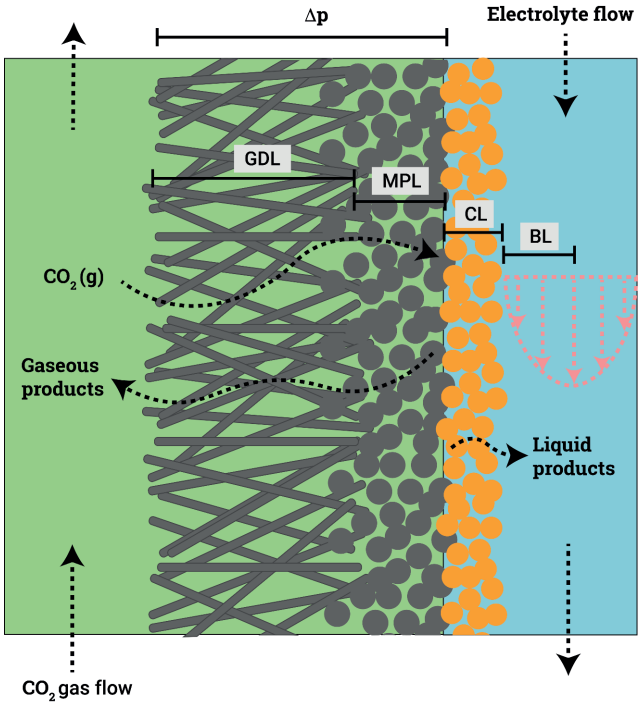

Figure 6.1: Illustration of a typical cathode setup in a GDE-based flow-cell for CO_2 reduction. The green and the blue zones signify the gas and the aqueous phase, respectively. The dotted arrows represent the general direction of the flow. GDL: gas diffusion layer, MPL: micro-porous layer, CL: catalyst layer, BL: boundary layer.

The classical GDE-based eCO_2R systems studied in literature are flow-cells or microfluidic cells following a general setup as shown in Figure 6.1 for the cathode half of the reactor [22–31]. The GDE cathode itself is typically composed of 3 layers: 1) the gas diffusion layer (GDL) which acts as a gas distribution network for the incoming CO_2 and outgoing gaseous products to and from the catalyst, 2) a thin micro-porous layer (MPL) of carbon nanoparticles deposited on the GDL which acts as the current collector and 3) the electrocatalyst layer (CL) which is deposited on top of the MPL.

During operation of a GDE, a gas stream of pure CO_2 flows from the inlet of a channel along the GDL, leaving the gas channel with the gaseous products of the catalysis. Similarly, a liquid flow channel facing the catalyst of the GDE continuously circulates the aqueous electrolyte. The diffusion length of CO_2 to the catalyst surface in such a setup is several orders of magnitude smaller than in a system where the CO_2 dissolved in the bulk electrolyte has to diffuse to the cathode surface (from here-on referred to as an H-cell type setup), resulting in a drastic improvement in the achievable current density attributed to eCO_2R.

Other system configurations such as membrane-electrode assemblies (MEA) inspired by fuel cell architectures have been proposed in literature as an alternative to flow-cells [24, 32–39]. MEAs reduce the impacts of flooding due to the elimination of liquid electrolyte flow, and can potentially achieve even higher eCO_2R current densities due to better access to CO_2 from the gas phase. These advantages make MEA setups an attractive candidate for systems operating at practically relevant scales. However, controlling product selectivity, water management, salt precipitation-related fouling as well as membrane stability can be a challenge in these setups due to the numerous competing physical phenomena occurring in a compact domain. There is considerable variation in the cell-design and performance analysis among the initial MEA studies, making a comparison between the different approaches difficult. Further systematic studies are required to establish best design and operational practices for optimal performance for the respective eCO_2R products.

In this chapter, we will focus on modeling the mass transport within the CL in flow-cell type systems as depicted in Figure 6.1. There are practical advantages to electrolyte-flow systems that make them a desirable setup for studying and optimizing eCO_2R such as: a higher control of

reaction conditions and therefore catalyst selectivity and activity through the composition of the electrolyte [18, 22, 25, 27, 31], better water management for the catalysis and for membrane stability, and ease of liquid product sampling due to continuous flow [24, 28]. As the number of experimental studies using GDE-based flow-cells increase, there is a rising need to compliment these with simulations to better understand the effect of the various system parameters on the measured performance. Flow-cell systems are much more complex than the H-cell setups that have been modeled extensively in literature so far [40–42], making it difficult to isolate and experimentally measure the effects of the various parameters. The porous structure of the CL is an essential feature of the flow-cell systems and this necessitates the consideration of the effect of catalyst structure on performance. Additionally, flow-cells present several design and operational handles to influence reaction conditions within the CL.

Electrolyte composition and pH within the catalyst layer of the GDE is understood to be an influential parameter for the selectivity of CO_2 reduction. Multiple experimental studies using flow-cells observe a correlation between the electrolyte and C-C coupling reaction on Cu catalysts to form ethylene [22, 27, 31], CO Faradaic efficiency on Ag [24–26, 30] and formate production on Sn [28]. An optimal control of the reaction environment is expected to have a dramatic influence on the catalyst performance as has also been observed in studies in H-cell setups [43–49]. Previously reported models pertaining to GDE flow-cell configurations assume a one-dimensional (1D) structure-less approach to simulating transport within the flow-cell CL [31, 50–52]. Here we simulate the reaction environment within an effective three-dimensional (3D) catalytic pore of a GDE-based flow-cell to understand the influence of changing pore structure and boundary conditions on the electrolyte composition during steady-state operation at practically relevant current densities (> 50 mA/cm^2, see Figure 6.4). We use the generalized modified Poisson-Nernst-Planck (GMPNP) model [40, 53, 54] from chapter 5 and extend it for 3D cylindrical pores with appropriate boundary conditions relevant for laboratory flow-cell setups.

Our analysis of the GDE flow-cell finds that the length of the pore is one of the most influential structural parameters of the catalyst layer for the median pH and ion concentration within the pore. The length of the pore becomes an important parameter due to the fact that the

fluxes of species at the gas-electrolyte and electrolyte-electrolyte interface are large enough to compete with the rates of the reactive and diffusive processes within the pore. As a result, the boundary conditions for the catalyst layer such as the gas pressure and the electrolyte flow rate play a very important role in determining optimal reaction conditions for the catalyst. By comparing the performance of the GMPNP model with a reaction-diffusion model, we discuss the relevance of the applied potential for ionic concentration, CO_2 solubility and edge effects within the pore. GDE-based flow-cells are characterized by a narrow and porous catalyst layer surrounded by interfaces that have a major influence on transport of species in and out of the reactive domain. The reaction environment in GDE setups is expected to deviate significantly from what is encountered in eCO_2R in H-cell setups and therefore a considerably different performance with respect to onset-potential, selectivity and activity can be expected.

6.2. Model description

Figure 6.2 illustrates the cylindrical pore domain used for the GMPNP simulation. This is an idealization of the CL for the purposes of deduction. The pore structures in the actual CL deposited on the GDL are expected to be highly heterogeneous as reported in a very recent tomography study on Ag GDE cathode [55]. We assume the catalytic pore to be completely flooded with electrolyte such that the gas-electrolyte interface is located at the pore entry (the boundary between the MPL and CL, S_1). We believe that this is a reasonable assumption for a metal catalyst pore with small radii at a reducing potential and that a vast majority of current density in flow-cell systems can be attributed to the double-phase electrolyte-catalyst boundary (S_2) like in case of an H-cell. We use CO producing catalysts as a test case for our simulations due to the prevalence of several experimental studies using GDEs showing promising results for CO_2 reduction to CO [56–59]. Below sections discuss the boundary conditions assumed at S_1, S_2 and S_3 in detail. The values of the constants used in the model can be found in section B.2 in the Appendix. Parameters depicted in bold lettering imply vectors.

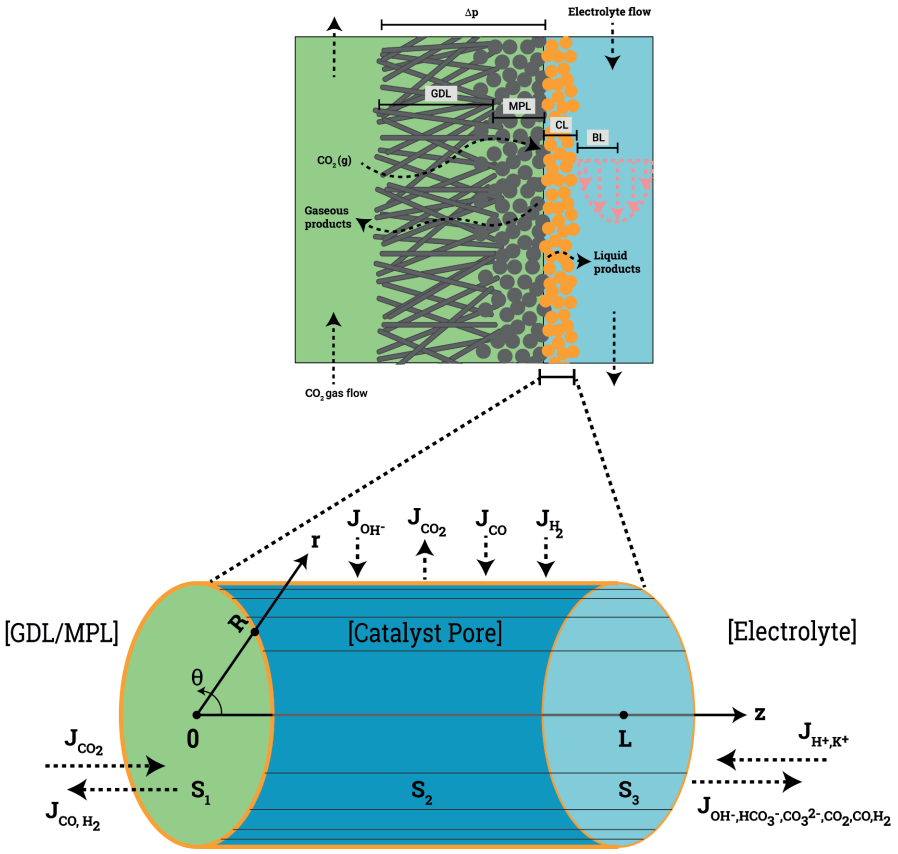

Figure 6.2: Illustration of the effective cylindrical pore used as the model system. S_1, S_2 and S_3 are the simulation domain boundary surfaces and represent the gas-electrolyte interface at the pore entry, the cylindrical catalyst surface and the electrolyte-electrolyte interface at the pore exit, respectively. R is the pore radius and L is the pore length. r, z and Θ represent the radial, longitudinal and azimuthal axes, respectively. $\mathbf{J}_i$ stands for the flux of species i normal to the respective surface.

6.2.1. Gas-electrolyte interface

The surface S_1 represents the gas-electrolyte interface located at the boundary between the MPL and the catalyst layer. The gas phase is assumed to be composed of 95% CO_2, 4.5% carbon monoxide (CO) and 0.5% hydrogen (H_2) and the pressure at S_1, p_1 is assumed to be 1 bar. We have ignored

the presence of humidity in the gas stream. The gas phase composition for CO producing GDE setups have not been reported for experimental setups in literature. We assume the gas phase to consist of a high % of CO_2 based on the fact that single-pass conversion efficiency for eCO_2R is typically low for lab-scale flow-cells. Several factors such as the incoming gas-phase CO_2 flow rate, the Faradaic efficiency of CO_2 reduction, the current density and the transport characteristics of the GDL and rate of the flux of the product gases across the gas-electrolyte interface will determine the steady-state composition at S_1. The interface S_1 is considered to be in equilibrium and Dirichlet boundary conditions are assumed for CO_2, CO and H_2 concentrations at S_1 as per the equation (6.1). The assumption of equilibrium at the gas-liquid interface is valid in majority of situations, except when very high mass transfer rates are present at the interface [60]. This can possibly be the case for the flux of the product species CO and H_2 across S_1 which are present in low concentrations in the gas phase and have relatively low solubility in the electrolyte. This is not seen as an issue for resolving the reaction environment within the pore, since, in addition to their low solubility, CO and H_2 do not interact with the electric field nor participate in the homogeneous reaction kinetics.

$$C_i^{S1} = H_i p_1 y_i \rho_e \tag{6.1}$$

where H_i is Henry's constant for species i (in mol·kg^{-1}·bar^{-1}), p_1 is the gas phase pressure at S_1 (in bar), y_i is the mole fraction of i at S_1, ρ_e is the density of the electrolyte (assumed as water density, not adjusted for ion concentration for simplicity, in kg·m^{-3} at 25°C) and C_i^{S1} is the concentration of species i at S_1 (in mM). H_{CO_2} is calculated using Sechenov equation [61, 62] (see section B.1.2 in the Appendix) to account for the effect of ion concentrations in the pore. Median values of ion concentrations in the pore are used at every time step to iteratively adjust the value of H_{CO_2} to determine the Dirichlet condition at S_1.

$$\mathbf{J}_{HCO_3^-, CO_3^{2-}, K^+, H^+, OH^-}|_{z=0,x,y,t} = 0 \tag{6.2}$$

The fluxes ($\mathbf{J}_i$) of all species except CO_2, CO and H_2 are considered to be 0 at S_1 (no-flux boundary condition). Dirichlet boundary condition is used for the potential at S_1 as given in equation (6.3).

$$\phi|_{z=0,x,y,t} = 0 \tag{6.3}$$

6.2.2. Catalyst surface

The following heterogeneous reactions are considered to be occurring at the cathode surface S_2 during eCO_2R. We assume CO producing catalysts such as Ag/Au as our test case.

$$CO_2(aq) + H_2O + 2\,e^- \rightleftharpoons CO(g) + 2\,OH^- \tag{6.4}$$

$$2\,H_2O + 2\,e^- \rightleftharpoons H_2(g) + 2\,OH^- \tag{6.5}$$

A total current density (I_{tot}) and Faradaic efficiency (FE) distribution (ratio of electrons consumed for H_2 production vs CO) is assumed for the simulations. No direct consumption of H^+ is assumed since the associated current will be negligible especially at the high current densities associated with flow-cells. The flux of the solution species at the surface is given by the equations (6.6) - (6.10). r=R in our simulations is assumed to be the outer Helmholtz plane (OHP) since there is no charge density in the Stern layer by definition. The factor of 0.5 in the equations (6.7) - (6.9) comes from the product to electron stoichiometry of the reactions (6.4) - (6.5). We assume no bubble formation of the product species within the catalyst pore and therefore also no convection or turbulence effects within the pore due to bubbling.

$$\mathbf{J}_{HCO_3^-,CO_3^{2-},K^+}|_{\sqrt{x^2+y^2}=R,z,t} = 0 \tag{6.6}$$

$$\mathbf{J}_{CO_2}|_{\sqrt{x^2+y^2}=R,z,t} = 0.5 \times \frac{I_{total}}{F} \times FE_{CO} \tag{6.7}$$

$$\mathbf{J}_{CO}|_{\sqrt{x^2+y^2}=R,z,t} = -0.5 \times \frac{I_{total}}{F} \times FE_{CO} \tag{6.8}$$

$$\mathbf{J}_{H_2}|_{\sqrt{x^2+y^2}=R,z,t} = -0.5 \times \frac{I_{total}}{F} \times FE_{H_2} \tag{6.9}$$

$$\mathbf{J}_{OH^-}|_{\sqrt{x^2+y^2}=R,z,t} = -\frac{I_{total}}{F} \tag{6.10}$$

where F is the Faraday's constant and FE_{CO} and FE_{H_2} are assumed to be 95% and 5%, respectively. Dirichlet boundary condition is used for the potential at S_2 as given in equation (6.11) where V_{app} is the applied voltage in V.

$$\phi|_{\sqrt{x^2+y^2}=R,z,t} = V_{app} \tag{6.11}$$

6.2.3. Electrolyte-electrolyte interface

We assume an electrolyte concentration of 1 M $KHCO_3$ as the bulk solution with the electrolyte flow parallel to the catalyst surface with a flow velocity $\mathbf{v}_e$ in $m^3 \cdot s^{-1}$. The flux of species i across the surface S_3 is assumed to depend linearly on the concentration gradient between S_3 and the bulk electrolyte solution as per the equation (6.12). We have assumed a very small concentration (1 % of equilibrium concentration at S_1) of CO and H_2 in the bulk solution to be able to normalize the concentrations of both species to solve the MPNP equations and to define the driving force for the flux in equation (6.12). Physically, this assumption implies that although, a majority of the CO and H_2 produced leave the system through the gas-liquid interface at S_1, a small quantity also moves into the bulk electrolyte through the liquid-liquid interface S_3 due to diffusive and convective fluxes. The value of 1% is arbitrarily chosen for the current simulations. Experimental data or models with more detailed treatment of CO and H_2 mass transport through the system can be used to better inform the concentration of CO and H_2 into the bulk electrolyte flow at steady state as a function of the operating conditions.

$$\mathbf{J}_i^e|_{z=L,x,y,t} = k_i^e(C_i^{S_3} - C_i^0) \quad i = CO_2, CO, H_2, HCO_3^-, CO_3^{2-}, H^+, OH^-, K^+ \tag{6.12}$$

$$Sh = \frac{k_i^e}{D_i/L_c} = 1.017(\frac{2L_c}{L_{cross}} ReSc)^{1/3} \tag{6.13}$$

$$Re = \frac{\rho_e |\mathbf{v}_e| L_c}{\mu_e A_{cross}} \tag{6.14}$$

$$Sc = \frac{\mu_e}{\rho_e D_i} \tag{6.15}$$

where k_i^e is the convective mass transfer coefficient in $\mathrm{m{\cdot}s^{-1}}$ derived using the Sherwood number (Sh) as per equation (6.13) [60]. $C_i^{S_3}$ and C_i^0 are the concentrations of species i at S_3 and in the bulk electrolyte, respectively (in mM). Equation (6.13) is applicable for laminar flow over a flat plate of length L_c (in m), which in this case, is the length of the catalyst along which the electrolyte is flowing, for an electrolyte film thickness assumed to be half of the cross-sectional width of the liquid channel ($L_{cross}/2$, in m) and a flow cross-section of A_{cross} (in $\mathrm{m^2}$). Re and Sc are Reynolds and Schmidt numbers respectively and are given by equations (6.14) and (6.15). ρ_e and μ_e are density (in $\mathrm{kg{\cdot}m^{-3}}$ at 25°C) and viscosity (in $\mathrm{kg{\cdot}m^{-1}{\cdot}s^{-1}}$ at 1 atm, 25°C) of the electrolyte, respectively and are assumed be that of pure water. Dirichlet boundary condition is used for the potential at S_3 as given in equation (6.16).

$$\phi|_{z=L,x,y,t} = 0 \tag{6.16}$$

6.2.4. GMPNP system of equations

The generalized modified Poisson-Nernst-Planck (MPNP) equations used to model the mass transport of species in the electrolyte within the cylindrical pore are the same as used in chapter 5.

$$\frac{\partial C_i}{\partial t} = -\nabla \cdot \mathbf{J}_i + \sum_j R_i \tag{6.17}$$

where C_i is the concentration of species i, t is time, j is the index of the homogeneous reaction in solution, R_i is the rate of production of species i due to the homogeneous reaction j as given by equations (B.6) to (B.10) and $\mathbf{J}_i$ is the flux of species i given by:

$$\mathbf{J}_i = -D_i^{eff}\nabla C_i - \frac{D_i^{eff} C_i z_i F}{R_G T}\nabla\phi - D_i^{eff} C_i \left(\frac{N_A \sum_{i=1}^{n} a_i^3 \nabla C_i}{1 - N_A \sum_{i=1}^{n} a_i^3 C_i}\right) \tag{6.18}$$

$$D_i^{eff} = \frac{D_i \epsilon \delta}{\tau^2} \tag{6.19}$$

where D_i^{eff} is the effective diffusion coefficient of species i given by equation (6.19) [63], z_i is the charge of species i, R_G is the gas constant, T is the temperature, N_A is the Avogadro's constant and a_i is the effective solvated diameter of the species i. In equation (6.19), D_i is the diffusion coefficient, ϵ, δ and τ are the effective porosity, constrictivity and tortuosity of the catalyst layer, respectively (assumed to be 0.5, 1.5 and 0.9, respectively). Equation (6.17) needs to be solved self-consistently with the Poisson equation given by:

$$\nabla \cdot (\varepsilon_0 \varepsilon_r \nabla \phi) = -F \sum_{i=1}^{n} z_i C_i \tag{6.20}$$

where ε_0 is the permittivity of vacuum, ε_r is the relative permittivity of the electrolyte and ϕ is the potential. The relative permittivity in equation (6.20) is assumed to vary with cation concentration as given by equation (6.21) [64, 65]. The concentration terms in the equation (6.21) are in M. M_{water} is the molarity of water at room temperature taken to be 55 M and the parameters w_i are the total number of water molecules held by the cation i. ε_r^0 is taken to be 80.1 equal to the relative permittivity of water at room temperature whereas ε_r^{min} is the dielectric constant of water under the condition of dielectric saturation and is taken as 6. The scaled GMPNP equations for the 3D cylindrical pore is given in the section B.1.6 in the Appendix.

$$\varepsilon_r = \varepsilon_r^0 \left(\frac{M_{water} - \sum_i^{ncat} w_i C_i}{M_{water}} \right) + \varepsilon_r^{min} \left(\frac{\sum_i^{ncat} w_i C_i}{M_{water}} \right) \tag{6.21}$$

All species are assumed to be at their bulk concentrations at t=0 with the catalyst in a grounded state as given in equations (6.22) and (6.23).

$$C_i|_{x,y,z,t=0} = C_i^0 \tag{6.22}$$

$$\phi|_{x,y,z,t=0} = 0 \tag{6.23}$$

The FEniCS project [66, 67] Python package is used to solve the Galerkin (weak) form of the GMPNP equations (6.17) - (6.20) using backward Euler method for time discretization (section B.1.6 in Appendix) over a uniform 3D cylindrical mesh.

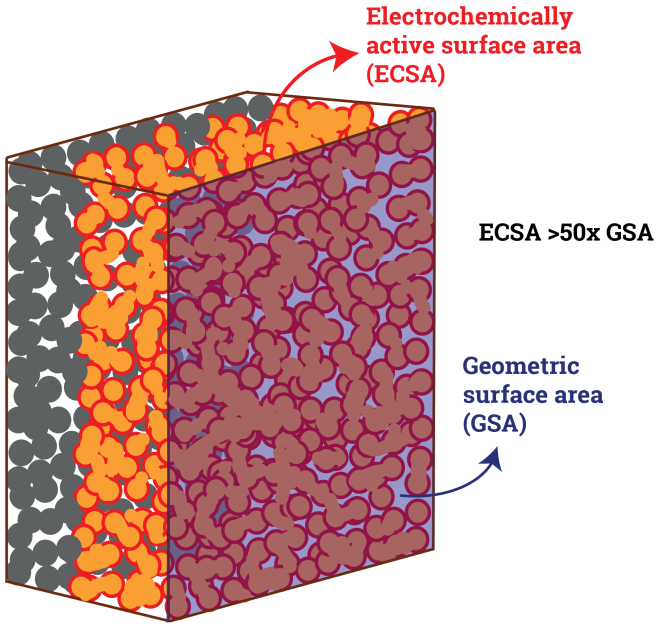

Figure 6.3: A cartoon illustration comparing the electrochemically active surface area (ECSA) depicted through the red outlines on the yellow catalyst *vs.* the geometric surface area (GSA) depicted through the blue semi-opaque projected surface on top of the catalyst layer. The grey particles represent the MPL deposited on top of the GDL as shown in Figure 6.1.

Since we are modeling an effective catalyst pore, the current density used for the simulations should be understood as electrochemically active surface area (ECSA)-normalized current density (I_{ECSA}) and not geometrically normalized (I_{geom}). Comparing and benchmarking the performance of nanostructured and porous electrodes for electrocatalysis necessitates the estimation of I_{ECSA} through catalytically active surface area measurements [68–70]. Figure 6.3 illustrates the difference between the catalyst surface area relevant for estimating I_{ECSA} *vs.* I_{geom}. I_{ECSA} can be understood in terms of I_{geom} and the catalyst roughness factor (f_r) as given by equation (6.24).

$$I_{ECSA} = \frac{I_{geom}}{f_r} \tag{6.24}$$

McLaughlin *et al.* [55] have recently reported surface area measure-

ments for Ag GDE which are equivalent to a roughness factor of ~50. f_r will depend on the properties of the catalyst and the GDL/MPL layer as well as on the deposition technique and the CL thickness. Additionally, the roughness can also change due to restructuring of the catalyst during operation. We use I_{ECSA} values of 1 mA/cm^2, 2 mA/cm^2 and 3 mA/cm^2 for the simulations in this chapter. Figure 6.4 shows I_{geom} as a function of I_{ECSA} with f_r as the slope (equation (6.24)).

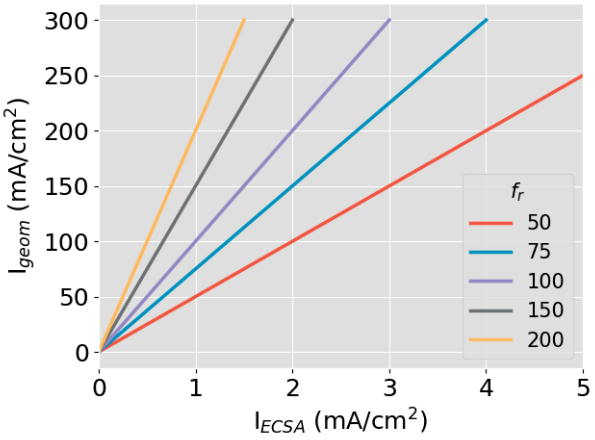

Figure 6.4: Plot showing geometrically normalized current density (I_{geom}) as a function of the electrochemically active surface area-normalized current density I_{ECSA} for different values of the roughness factor (f_r) as per equation (6.24).

In the following section, we present the results for GMPNP simulations within a cylindrical pore for changing pore geometry and boundary conditions. Unlike the 1D GMPNP simulations in chapter 5, where a wide range of potentials were simulated to study the effect on the electrical double layer (EDL), here we focus on comparing the median values of species concentrations within the catalytic pore. The 3D simulations are numerically unstable beyond a small applied potential (V_{app}) at the OHP of -25 mV vs potential at the point of zero charge (PZC) and require extremely small time steps to converge. This makes the simulations at higher V_{app} computationally intractable. All GMPNP results reported in this chapter are derived for an applied potential of -25 mV vs PZC which corresponds to a surface potential of ~-0.5 V vs standard hydrogen electrode (SHE) for Ag(111) and ~-0.75 V vs SHE for polycrystalline Ag (table B.2 and

Figure 5.2a). Steric effects are not expected to play an important role at small applied potentials and similar results are expected from a PNP model without any steric modifications to the flux term in equation (6.18). However, as discussed in section 5.1.3 in chapter 5, the GMPNP equations are numerically more stable than PNP and do not require additional numerical stabilization for convergence.

Lastly, based on the few attempts at measuring the pore structure properties of metal catalysts deposited on GDEs for eCO_2R [22, 55], the pore radii are expected to lie between 100 to 1000 nm. We have assumed a radius of 5 nm for our simulations unless otherwise stated, primarily due to computational limitations since the finite element mesh grows with R^2. A very fine space discretization is needed in order to resolve the EDL region close to the cylindrical surface S_2 using the GMPNP model. A mesh with radially variable element sizes can be used for pores with larger radii to circumvent this issue. The pore radius is not expected to influence the conclusions drawn regarding the influence of pore structure on mean reaction conditions within the pore (section 6.3.1). However, the influence of R will become prominent when studying the effect of applied potential on median reaction conditions within the pore and will be discussed further in section 6.3.2.

6.3. Results

In the section 6.3.1 that follows, we vary different aspects of the pore structure to study its effect on the median properties of the electrolyte within the effective catalyst pore. The section 6.3.2 considers the effect of the model choices such as the boundary conditions in more detail and provides a comparison with the reaction-diffusion model.

6.3.1. Pore structure of catalyst

Length of catalyst pore

The length of the catalyst pore is a function of the thickness of the catalyst layer deposited on top of the MPL as well as the tortuosity (τ) of the porous structure. We have varied the length of the model cylindrical pore L in order to study its effect on the concentration of the various solution species within the pore. Catalyst layer thickness has been shown

to effect the eCO_2R performance experimentally where the variation has been attributed to CO_2 concentration and the pH within the catalyst pores [31].

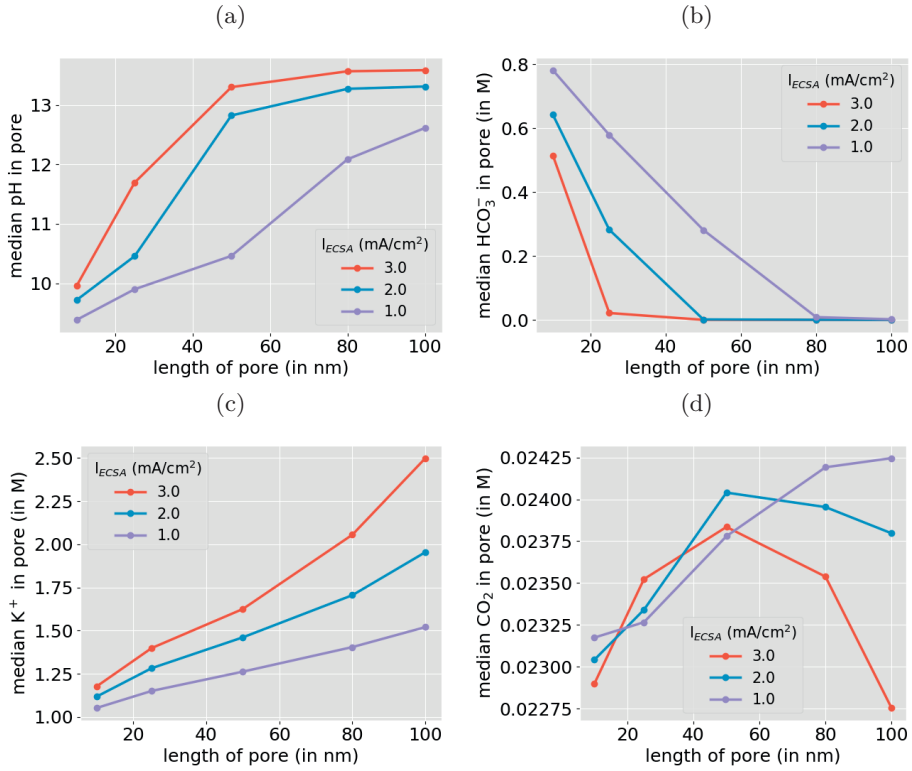

Figure 6.5: Influence of changing length (L) of effective catalyst pore on median concentrations of electrolyte species within pore for different values of I_{ECSA}. Figure 6.4 and equation (6.24) can be used to translate the I_{ECSA} values to the corresponding I_{geom} and roughness factor (f_r). The radius (R) of all pores is 5 nm.

Figure 6.5a and 6.5b show how, as the length of the pore increases, the pH in the pore becomes more basic accompanied by a buffer breakdown seen by the depletion of HCO_3^- from the pore. This dramatic increase in pH for constant I_{ECSA} with increasing L is a result of the relative rate of diffusion of species within the pore and their flux at the electrolyte-electrolyte interface S_3. The length of the pore needed for the buffer

breakdown to happen goes down with increasing I_{ECSA} due to a higher rate of OH^- production. Another interesting consequence of increasing pore length is the build-up of cations and carbonate ions within the pore as can be seen in Figure 6.5c and B.8. The concentration of these charged species has an influence on the solubility of CO_2 within the pore as described in section 6.2.1. The concentration of the cations and carbonate ions can also be relevant for ion precipitation within the catalyst pores which can potentially lead to fouling [22, 30]. We do not assume any specific adsorption of cations on the catalyst surface in our simulations as in chapter 5. However, an increased build-up of cations within the pores at high applied voltage can possibly result in the cations chemically adsorbing on the catalyst walls and significantly influencing catalyst activity. Although, the absolute CO_2 concentration does not change significantly over the whole range of L and I_{ECSA} (Figure 6.5d), the trend shows a clear competition between the outgoing CO_2 fluxes at S_2 and S_3 as well as the influence of higher ion concentrations on the equilibrium concentration of CO_2 at S_1.

Figures 6.10b, B.14b, B.16a, B.15b and B.17 show the distribution of electrolyte species across a longitudinal cross-section of a 5 nm x 100 nm (R x L) pore derived for the GMPNP model. No significant variation can be observed for the solution species along the length of the pore except for the products CO and H_2 which are present in a very low concentration. The species fluxes and the applied potential, however, have a clear influence on the concentration profiles along the pore boundaries. The influence of applied potential on concentration profiles follows the same general behavior as discussed in chapter 5. The product gases CO and H_2 are assumed to be at equilibrium at the gas-liquid interface as mentioned previously. This implies that as the catalytic reaction progresses within the pore, CO and H_2 build up beyond their equilibrium solution concentration along the length of the pore as can be seen in Figure B.17. The mass transport of gaseous product species from the flooded catalyst pore through the GDL can be much more complex than captured by the model used. However, since CO and H_2 are present in very low concentrations, are uncharged species and do not participate in any homogeneous reactions in the electrolyte, their mass transport within the pore can be independently resolved through more complex models that take into account possible nucleation and bubble formation. If the formation of gaseous bub-

bles is, in fact, a significant effect within the catalyst pores, this will in turn influence the mass transport of other species through turbulence and fluctuation of catalyst surface voltage [71] leading to a much more complex dependence between the transport and catalyst performance.

Surface area of catalyst pore

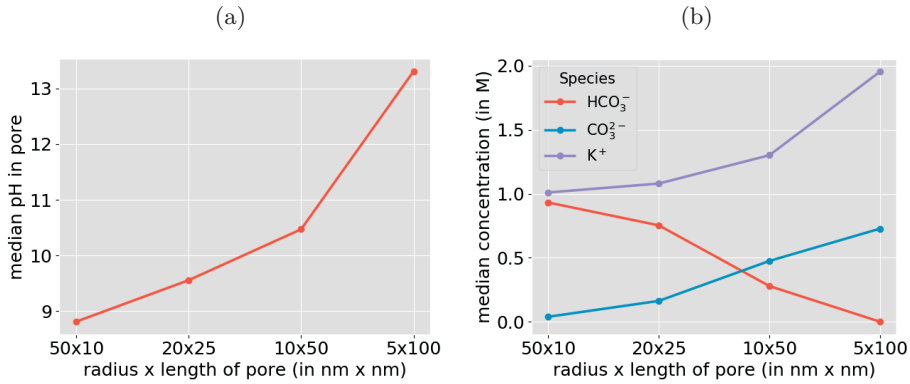

Figure 6.6: Comparison of median concentration of electrolyte species within catalyst pore for pores with same surface area. Results derived at I_{ECSA}=2 mA/cm^2.

Catalyst surface area is often regarded as a very important parameter for improving performance. Figure 6.6 compares the concentration of electrolyte species for catalyst pores having the same surface area but different R and L. It can be seen that even for the same surface area and I_{ECSA}, the difference between the reaction environment within the pores is dramatic. The construction of the GDE flow-cell system is such that a relatively thin catalyst layer faces a gas-liquid interface on one side and electrolyte flowing in a direction perpendicular to the pore length on the other. As a consequence, the thickness of the catalyst layer (L) ends up being the dominant effect and the trend seen in Figure 6.6 is not very different from the blue curves for I_{ECSA}=2 mA/cm^2 in Figure 6.5. Therefore, catalysts with the same surface area but with different catalyst layer thickness can be expected to show very different selectivity for CO_2 reduction.

Effective diffusion coefficient in catalyst pore

One of the effects of changing the porous structure of the catalyst is the change in the effective diffusion coefficient of electrolyte species as given by equation (6.19). For catalyst pores flooded with electrolyte, the ratio of the effective and bulk diffusion coefficient (D^i_{eff}/D^i) for a species can range between 0 and 1. Figure B.9 in the Appendix shows how changing this ratio has no considerable effect on the median reaction environment within the pore. Therefore, it can be concluded that unless the medium of species transport within the pore changes, the change in the effective diffusion coefficient of species with changing catalyst structure is not an important effect. The effective porosity (ϵ), constrictivity (δ) and tortuosity (τ) are however, influential factors as they are directly related to the catalyst structure.

Geometric vs ECSA normalized current density

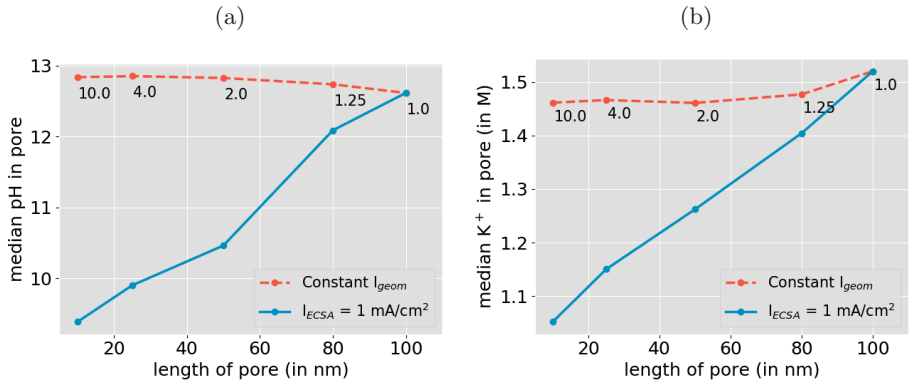

Figure 6.7: A comparison between median pH and cation concentration within pore derived for constant I_{geom} *vs.* constant I_{ECSA} of 1 mA/cm^2. The annotations on the red dotted curve signify the value of I_{ECSA} corresponding to the respective pore size for the constant I_{geom}. The radius of pore (R) is 5 nm for all cases.

Figure 6.7 and B.10 demonstrate the difference between comparing the reaction environment within the catalyst pores at a fixed ECSA *vs.* geometrically normalized current density. I_{geom} is fixed (red dotted curve) such that the I_{ECSA} is 1 mA/cm^2 for a pore of length 100 nm. The

roughness factor is assumed to be directly proportional to the pore surface area and the I_{ECSA} is adjusted accordingly to keep $I_{ECSA}{}^{*}f_r$ or I_{geom} constant (see equation 6.24). The pH or the cation concentration within the pore does not change significantly when compared at constant I_{geom} unlike at a constant I_{ECSA}. However, a comparison of different catalysts at constant I_{geom} is not useful for isolating the influence of the inherent catalytic activity and the reaction environment by not taking into account the active surface area of the catalyst [68–70].

6.3.2. Boundary conditions and choice of model

The CL thickness is typically relatively small in the order of a few 100 nm in a typical GDE based flow-cell. Consequently, the boundary conditions for the CL play a hugely important role in determining the reaction conditions. The following sections discuss the influence of the electrolyte flow rate at the electrolyte-electrolyte-interface S_3, the gas pressure at the gas-electrolyte interface S_1 and the applied potential at the catalyst surface S_2 on the environment within the model pore.

Electrolyte flow rate

Figure 6.8 shows the influence of changing the Reynolds number for the electrolyte flow at the electrolyte-electrolyte interface in a direction perpendicular to the pore length (see Figure 6.1). The default Reynolds number according to the laboratory setup and the parameters reported in table B.2 is ~28. This is equivalent to an electrolyte flow velocity of 0.1 m/min or a volumetric flow of 15 ml/min ($\mid \mathbf{v}_e \mid$) across a flow channel with cross section of 1.5 cm^2 (A_{cross}) as per equation (6.14). The Reynolds number for the electrolyte flow influences the flux of species at the interface S_3 according to the equations (6.12) - (6.15).

The pH within the catalyst pore reduces dramatically on increasing the Reynolds number as seen in Figure 6.8a by increasing the flux of OH^- ions out of the pore towards the bulk electrolyte. The red curve for $HCO_3{}^-$ in Figure 6.8b follows the pH trend signifying buffer breakdown at low electrolyte flow rates. Although, the CO_2 concentration in the pore does not change significantly due to Reynolds number as shown in Figure B.11, the concave nature of the curve demonstrates the competition between CO_2 solubility based on the ionic concentration within the pore

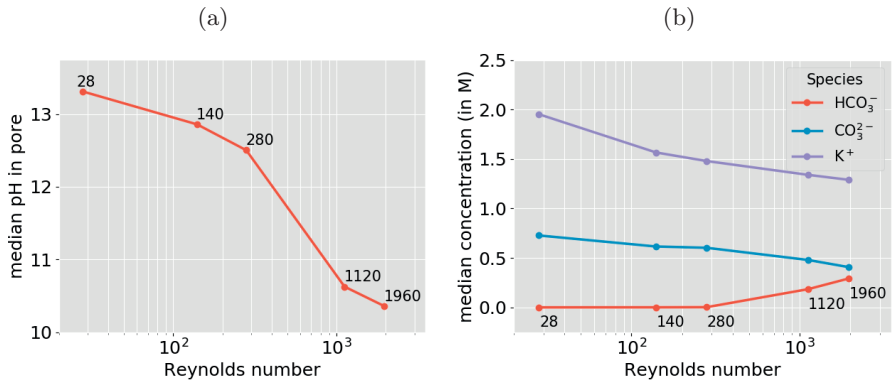

Figure 6.8: Effect of changing Reynolds number on the median pH and concentration of charged species in the catalyst pore. Reynolds numbers of 28, 140, 280, 1120 and 1960 corresponds to electrolyte flow velocities ($|\ \mathbf{v}_e\ |/A_{cross}$ in equation (6.14)) of 0.1 m/min, 0.5 m/min, 1 m/min, 4 m/min and 7 m/min, respectively. A pore of 5 nm x 100 nm (R x L) and I_{ECSA}=2 mA/cm^2 is used for all data points.

and the outward flux of the CO_2 at S_3. Flow rate of electrolyte has been shown to influence the catalyst selectivity in experimental studies using flow-cells [24, 28]. This is not surprising considering the extent to which electrolyte flow can potentially alter conditions within the CL. Management of pressure drop across the GDE can however, be a non-trivial aspect of the operation of the flow-cell and can possibly limit the use of electrolyte flow rate as a control mechanism for product selectivity.

Gas pressure

Gas pressure has also been used as an operational handle to tune product selectivity in flow-cells [26]. A variation in gas-pressure will need adjustment of the liquid pressure in order to maintain the gas-electrolyte interface at S_1 such that the capillary pressure of the pores plus the liquid pressure balance the gas pressure. A pressure imbalance can lead to either gas channels within the CL pores or flooding of the GDL and will significantly change the nature of mass transport within the CL. We assume that S_1 remains stationary after increasing the gas pressure and that the electrolyte properties remain unchanged.

Figure B.12 in the Appendix shows the influence of increasing pressure

at the gas-electrolyte interface S_1 on the reaction environment within the pore. Increasing the gas pressure from 1 bar to 10 bar leads to a reduction in the pH by ~0.8 units and factor of 10 increase in the median CO_2 concentration. The reduction of pH on increasing gas pressure also results in an increase in CO_3^{2-} and K^+ as a consequence of the buffer reactions and the electrostatic interactions in the electrolyte. In terms of pH, the effect of increasing the gas pressure by a factor of 10 is very similar to the effect of reducing the electrolyte flow velocity by a factor of 10 at the electrolyte-electrolyte interface (see drop in pH between a Reynolds number of 28 and 280 in Figure 6.8a). The influence on the CO_2 availability within the pore however, is very different for the two scenarios. Both operational handles of gas pressure and electrolyte flow involve practical challenges regarding management of flooding of the GDL and electrolyte distribution within the CL. The appropriate control mechanism for reaction conditions can be chosen based on whether CO_2 concentration becomes limiting through the CL (for thick layers) and the stability of the gas-electrolyte interface.

Applied potential

We compare the output from a reaction diffusion model (section B.1.7 in Appendix) with the GMPNP model to understand the influence of taking applied potential at the catalyst surface S_2 into account. For the small pore radius of 5 nm and also a small applied potential of -25 mV vs PZC used as a boundary condition for the GMPNP model, the median pH (Figure 6.9a) and buffer breakdown (Figure B.13) with changing pore length does not vary significantly between the two models. This is not surprising, since the effect of the EDL formation is restricted to ~1 nm around the catalyst surface at the small applied potential and is not expected to perturb the median H^+ concentration of the pore drastically. The slightly low pH obtained for GMPNP is owing to the fact that the catalyst surface is negatively charged leading to a build-up of positively charged ions in the EDL. The effect of the EDL is exaggerated, however, for CO_3^{2-} and K^+ (Figures 6.9c and 6.9d) which are present in a much higher concentration in the solution relative to protons and hydroxide ions especially in a condition of a buffer breakdown. The repulsion of CO_3^{2-} due to the negative charge on the surface leads to a very different balance of charged species within the pore. This variation in-turn influences the solubility of

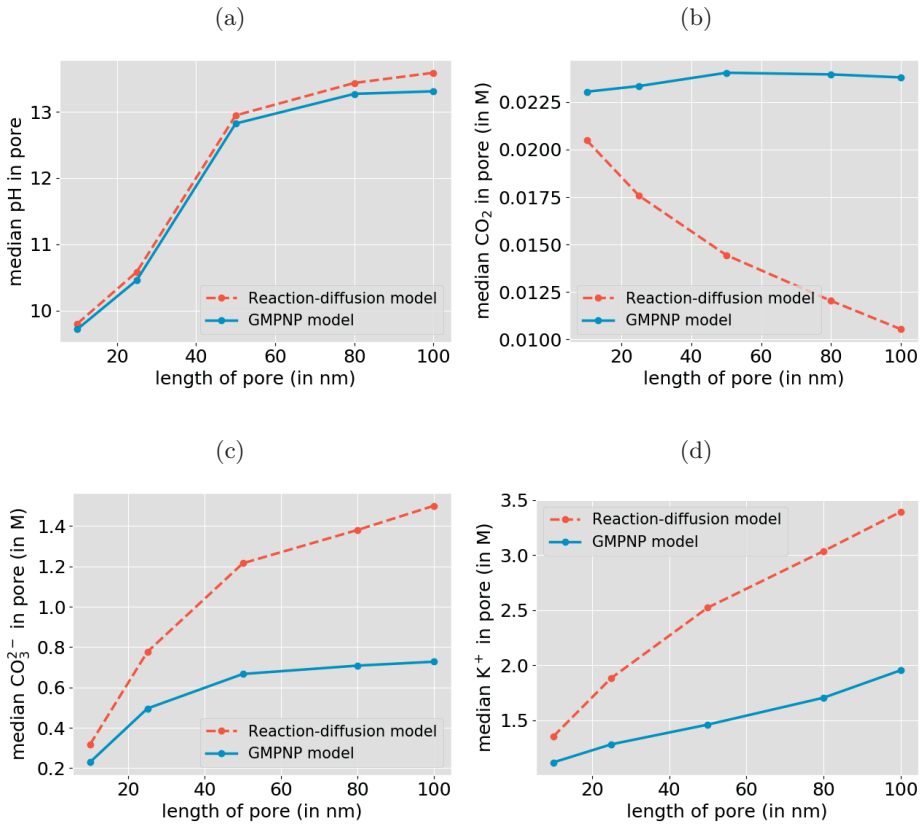

Figure 6.9: Comparing the median concentration of species in the catalyst pore with changing pore length (L) derived using a reaction-diffusion model and a GMPNP model. A pore of 5 nm x 100 nm (R x L) and I_{ECSA}=2 mA/cm^2 is used for all data points.

CO_2 in the electrolyte and results in the deviating trends seen for median CO_2 concentration in Figure 6.9b.

Figure 6.10 shows the CO_2 concentration along a longitudinal cross-section of the pore. The concentration of CO_2 does not vary significantly within the pore for either of the models as can be seen from Figure 6.10a. However, making the concentration scales narrower for each model reveals a very different distribution of CO_2, both radially and longitudinally. The concentration profile obtained using the GMPNP model in Figure 6.10b

(a) Common scale

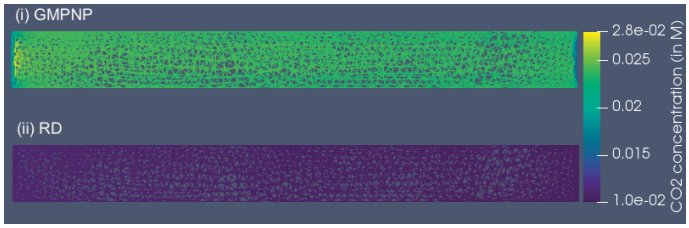

(b) GMPNP

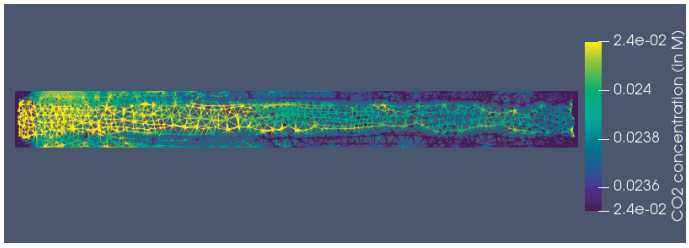

(c) RD

Figure 6.10: A comparison of CO_2 concentration along a longitudinal cross-section of a pore with R x L of 5 nm x 100 nm and I_{ECSA}=2 mA/cm^2 for the GMPNP and reaction-diffusion (RD) model. An applied potential of -25 mV vs PZC for the catalyst surface is used for the GMPNP model. The gas-liquid interface is the left edge whereas the electrolyte-electrolyte interface is the right edge with the top and bottom edges being part of the catalyst surface. (a) shows the output of the GMPNP and RD model on the same scale for comparison. (b) and (c) show the distribution on separate scales for clarity.

clearly captures the edge effects due to the presence of the electric field at the catalyst surface as well as ion accumulation in the EDL which are absent in the reaction-diffusion model in Figure 6.10a. Similar comparisons for other solution species can be found in Figures B.14b, B.16a, B.15b and B.17 in the Appendix.

Increasing the radius of the pore is expected to diminish the influence of the EDL on the median concentration predicted by the GMPNP. On the other hand, a higher applied potential should further exaggerate the differences in the prediction from the GMPNP *vs.* the reaction-diffusion model. Using the reaction-diffusion model to derive trends for median reaction conditions in the pore volume can be a reasonable choice, especially when studying pores with large radii and lengths. However, if it is desired to study the edge effects in these systems such as the environment in the vicinity of the interfaces, the reaction-diffusion model can be grossly insufficient owing to the missing electrostatic effects. The curvature of pores with >= 5 nm radius is expected to be large enough for the EDL to behave similar to a flat plate and 1D simulations such as in chapter 5 can instead be used to specifically study the EDL properties [72]. The arrangement of ions within pores with radii similar in length scale to the EDL can no longer be accurately predicted using continuum models and requires molecular level treatment [73–75]. Pores with high curvature (small radii) can make the limitations of the current GMPNP model even more pronounced, especially regarding the treatment of solvent water molecules and their relative interaction with the hydrophilic catalyst surface *vs.* the ionic species, van der Waals forces and Coulombic interaction between charged species [76] (also see section 5.3 of chapter 5). It is not expected for pores below 5 nm radius to have a significant population in the CL and therefore can be safely ignored for building models for the CL [22, 55].

6.4. Conclusions

An effective flooded cylindrical catalyst pore was used to study the influence of changing pore geometry and boundary conditions on the reaction environment during eCO_2R in a GDE-based flow cell setup. The length of the catalytic pore was found to be an important parameter, determining the pH, buffer breakdown and concentration of ionic species in the pore. We find that pores with the same surface area but different lengths can have very different reaction environments. The thickness of the deposited catalyst layer on top of the GDL is therefore expected to be an important design handle for optimizing performance. The flux of species across the gas-electrolyte interface at the MPL/CL boundary as well as across the

electrolyte-electrolyte interface play a significant role in determining the reaction conditions within the CL. The transport properties and operating conditions for the gas flow, the gas composition and pressure, and the electrolyte flow rate and flow-channel geometry, are therefore expected to have a major influence on the resultant catalyst selectivity and activity. We also find that the dependence of the diffusion coefficient of solution species on the pore structure does not have any considerable impact on the mass transport as long as the catalyst pores are assumed to be flooded with the electrolyte. A comparison of the GMPNP model with the reaction-diffusion model shows that the applied potential is an important parameter for ionic concentration within the pore, which in turn influences the CO_2 solubility in the electrolyte. Reaction-diffusion model can be sufficient for studying median concentration of species within the catalyst layer for pores with large radii and length since the influence of the relatively thin electrical double layer (EDL) diminishes with the increasing pore volume. However, considering the electrostatic effect of the applied potential becomes essential if studying edge effects and the environment in the vicinity of the catalyst surface is the aim.

Management of pressure drop across the various system components to maintain the desired gas-electrolyte interfaces for catalysis can be very challenging for practical operation of flow-cell systems. There is a need to better understand the wetting properties of the catalyst layer and the parameters influencing flooding, film thickness and formation of vapor channels in this layer. Fluid dynamics is therefore an important aspect of flow-cell systems and should be coupled with the PNP equations to model the transport and possible two-phase flow within the CL. Lastly, a major challenge in modeling heterogeneous porous catalytic systems lies in the upscaling of microscopic models such as the one reported here to the macroscopic level [77]. Developing upscaling frameworks to accurately model the influential aspects of the mass transport will be an important step to study the performance of GDE-based eCO_2R systems. The presence of 2-phase interfaces and electrolyte flow at the boundaries of a relatively thin, charged and nanostructured catalyst layer, make mass transport central to the performance of flow-cell setups for eCO_2R. The sensitivity of the catalysis to structural and operational parameters for such systems will be significantly higher than the traditionally studied H-cells. The field should therefore move towards benchmarking of sys-

tem performance against these parameters to improve reproducibility and shorten the development cycle towards an industrial scale system.

References

[1] W. Zhang, Y. Hu, L. Ma, G. Zhu, Y. Wang, X. Xue, R. Chen, S. Yang, and Z. Jin, *Progress and perspective of electrocatalytic CO_2 reduction for renewable carbonaceous fuels and chemicals,* Advanced Science **5**, 1700275 (2018).

[2] L. Zhang, Z. Wang, N. Mehio, X. Jin, and S. Dai, *Thickness- and particle-size-dependent electrochemical reduction of carbon dioxide on thin-layer porous silver electrodes,* ChemSusChem **9**, 428 (2016).

[3] Q. Lu, J. Rosen, Y. Zhou, G. S. Hutchings, Y. C. Kimmel, J. G. Chen, and F. Jiao, *A selective and efficient electrocatalyst for carbon dioxide reduction,* Nature Communications **5**, 3242 (2014).

[4] F. Li, S.-F. Zhao, L. Chen, A. Khan, D. R. MacFarlane, and J. Zhang, *Polyethylenimine promoted electrocatalytic reduction of CO_2 to CO in aqueous medium by graphene-supported amorphous molybdenum sulphide,* Energy Environ. Sci. **9**, 216 (2016).

[5] S. K. Kim, Y.-J. Zhang, H. Bergstrom, R. Michalsky, and A. Peterson, *Understanding the low-overpotential production of CH_4 from CO_2 on Mo_2C catalysts,* ACS Catalysis **6**, 2003 (2016).

[6] F. Li, L. Chen, G. P. Knowles, D. R. MacFarlane, and J. Zhang, *Hierarchical mesoporous SnO_2 nanosheets on carbon cloth: a robust and flexible electrocatalyst for CO_2 reduction with high efficiency and selectivity,* Angewandte chemie international edition **56**, 505 (2017).

[7] W. Luc, C. Collins, S. Wang, H. Xin, K. He, Y. Kang, and F. Jiao, *Ag-sn bimetallic catalyst with a core-shell structure for CO_2 reduction,* Journal of the American Chemical Society **139**, 1885 (2017).

[8] J. He, X. Liu, H. Liu, Z. Zhao, Y. Ding, and J. Luo, *Highly selective electrocatalytic reduction of CO_2 to formate over tin(IV) sulfide monolayers,* Journal of Catalysis **364**, 125 (2018).

[9] R. Reske, H. Mistry, F. Behafarid, B. Roldan Cuenya, and P. Strasser, *Particle size effects in the catalytic electroreduction of CO_2 on Cu nanoparticles,* Journal of the American Chemical Society **136**, 6978 (2014).

[10] D. Ren, Y. Deng, A. D. Handoko, C. S. Chen, S. Malkhandi, and B. S. Yeo, *Selective electrochemical reduction of carbon dioxide to ethylene and ethanol on copper(I) oxide catalysts,* ACS Catalysis **5**, 2814 (2015).

[11] H.-P. Yang, S. Qin, Y.-N. Yue, L. Liu, H. Wang, and J.-X. Lu, *Entrapment of a pyridine derivative within a copper-palladium alloy: a bifunctional catalyst for electrochemical reduction of CO_2 to alcohols with excellent selectivity and reusability,* Catal. Sci. Technol. **6**, 6490 (2016).

[12] M. Jouny, W. Luc, and F. Jiao, *General techno-economic analysis of CO_2 electrolysis systems,* Industrial & Engineering Chemistry Research **57**, 2165 (2018).

[13] S. Verma, B. Kim, H.-R. Jhong, S. Ma, and P. J. A. Kenis, *A gross-margin model for defining technoeconomic benchmarks in the electroreduction of CO_2,* ChemSusChem **9**, 1972 (2016).

[14] J. M. Spurgeon and B. Kumar, *A comparative technoeconomic analysis of pathways for commercial electrochemical CO_2 reduction to liquid products,* Energy Environ. Sci. **11**, 1536 (2018).

[15] O. G. Sánchez, Y. Y. Birdja, M. Bulut, J. Vaes, T. Breugelmans, and D. Pant, *Recent advances in industrial CO_2 electroreduction,* Current Opinion in Green and Sustainable Chemistry **16**, 47 (2019), cO2 Capture and Chemistry.

[16] T. Burdyny and W. A. Smith, *CO_2 reduction on gas-diffusion electrodes and why catalytic performance must be assessed at commercially-relevant conditions,* Energy Environ. Sci. **12**, 1442 (2019).

[17] D. Higgins, C. Hahn, C. Xiang, T. F. Jaramillo, and A. Z. Weber, *Gas-diffusion electrodes for carbon dioxide reduction: A new paradigm,* ACS Energy Letters **4**, 317 (2019).

[18] D. M. Weekes, D. A. Salvatore, A. Reyes, A. Huang, and C. P. Berlinguette, *Electrolytic CO_2 reduction in a flow cell,* Accounts of Chemical Research **51**, 910 (2018).

[19] L. Fan, C. Xia, F. Yang, J. Wang, H. Wang, and Y. Lu, *Strategies in catalysts and electrolyzer design for electrochemical CO_2 reduction toward C_{2+} products,* Science Advances **6** (2020), 10.1126/sciadv.aay3111.

[20] M. G. Kibria, J. P. Edwards, C. M. Gabardo, C.-T. Dinh, A. Seifitokaldani, D. Sinton, and E. H. Sargent, *Electrochemical CO_2 reduction into chemical feedstocks: from mechanistic electrocatalysis models to system design,* Advanced Materials **31**, 1807166 (2019).

[21] B. Endrődi, G. Bencsik, F. Darvas, R. Jones, K. Rajeshwar, and C. Janáky, *Continuous-flow electroreduction of carbon dioxide,* Progress in Energy and Combustion Science **62**, 133 (2017).

[22] J.-J. Lv, M. Jouny, W. Luc, W. Zhu, J.-J. Zhu, and F. Jiao, *A highly porous copper electrocatalyst for carbon dioxide reduction,* Advanced Materials **30**, 1803111 (2018).

[23] J. Wu, S. Ma, J. Sun, J. I. Gold, C. Tiwary, B. Kim, L. Zhu, N. Chopra, I. N. Odeh, R. Vajtai, A. Z. Yu, R. Luo, J. Lou, G. Ding, P. J. A. Kenis, and P. M. Ajayan, *A metal-free electrocatalyst for carbon dioxide reduction to multi-carbon hydrocarbons and oxygenates,* Nature Communications **7**, 13869 (2016).

[24] C. Delacourt, P. L. Ridgway, J. B. Kerr, and J. Newman, *Design of an electrochemical cell making syngas ($CO+H_2$) from CO_2 and H_2O reduction at room temperature,* Journal of The Electrochemical Society **155**, B42 (2008).

[25] S. Verma, X. Lu, S. Ma, R. I. Masel, and P. J. A. Kenis, *The effect of electrolyte composition on the electroreduction of CO_2 to CO on Ag based gas diffusion electrodes,* Phys. Chem. Chem. Phys. **18**, 7075 (2016).

[26] C. M. Gabardo, A. Seifitokaldani, J. P. Edwards, C.-T. Dinh, T. Burdyny, M. G. Kibria, C. P. O'Brien, E. H. Sargent, and D. Sinton,

Combined high alkalinity and pressurization enable efficient CO_2 electroreduction to CO, Energy & Environmental Science **11**, 2531 (2018).

[27] M. G. Kibria, C.-T. Dinh, A. Seifitokaldani, P. De Luna, T. Burdyny, R. Quintero-Bermudez, M. B. Ross, O. S. Bushuyev, F. P. García de Arquer, P. Yang, D. Sinton, and E. H. Sargent, *A surface reconstruction route to high productivity and selectivity in CO_2 electroreduction toward C^{2+} hydrocarbons,* Advanced Materials **30**, 1804867 (2018).

[28] D. T. Whipple, E. C. Finke, and P. J. A. Kenis, *Microfluidic reactor for the electrochemical reduction of carbon dioxide: The effect of pH,* Electrochemical and Solid-State Letters **13**, B109 (2010).

[29] H. Li and C. Oloman, *The electro-reduction of carbon dioxide in a continuous reactor,* Journal of Applied Electrochemistry **35**, 955 (2005).

[30] S. Verma, Y. Hamasaki, C. Kim, W. Huang, S. Lu, H.-R. M. Jhong, A. A. Gewirth, T. Fujigaya, N. Nakashima, and P. J. A. Kenis, *Insights into the low overpotential electroreduction of co2 to co on a supported gold catalyst in an alkaline flow electrolyzer,* ACS Energy Letters **3**, 193 (2018).

[31] C.-T. Dinh, T. Burdyny, M. G. Kibria, A. Seifitokaldani, C. M. Gabardo, F. P. G. De Arquer, A. Kiani, J. P. Edwards, P. De Luna, O. S. Bushuyev, *et al.*, *CO_2 electroreduction to ethylene via hydroxide-mediated copper catalysis at an abrupt interface,* Science **360**, 783 (2018).

[32] Y. C. Li, D. Zhou, Z. Yan, R. H. Gonçalves, D. A. Salvatore, C. P. Berlinguette, and T. E. Mallouk, *Electrolysis of CO_2 to syngas in bipolar membrane-based electrochemical cells,* ACS Energy Letters **1**, 1149 (2016).

[33] Z. Liu, R. I. Masel, Q. Chen, R. Kutz, H. Yang, K. Lewinski, M. Kaplun, S. Luopa, and D. R. Lutz, *Electrochemical generation of syngas from water and carbon dioxide at industrially important rates,* Journal of CO2 Utilization **15**, 50 (2016).

[34] W. Lee, Y. E. Kim, M. H. Youn, S. K. Jeong, and K. T. Park, *Catholyte-free electrocatalytic co2 reduction to formate,* Angewandte Chemie International Edition **57**, 6883 (2018).

[35] T. Zheng, K. Jiang, N. Ta, Y. Hu, J. Zeng, J. Liu, and H. Wang, *Large-scale and highly selective CO_2 electrocatalytic reduction on nickel single-atom catalyst,* Joule **3**, 265 (2019).

[36] C. M. Gabardo, C. P. O'Brien, J. P. Edwards, C. McCallum, Y. Xu, C.-T. Dinh, J. Li, E. H. Sargent, and D. Sinton, *Continuous carbon dioxide electroreduction to concentrated multi-carbon products using a membrane electrode assembly,* Joule **3**, 2777 (2019).

[37] C. Xia, P. Zhu, Q. Jiang, Y. Pan, W. Liang, E. Stavitski, H. N. Alshareef, and H. Wang, *Continuous production of pure liquid fuel solutions via electrocatalytic CO_2 reduction using solid-electrolyte devices,* Nature Energy **4**, 776 (2019).

[38] Z. Yin, H. Peng, X. Wei, H. Zhou, J. Gong, M. Huai, L. Xiao, G. Wang, J. Lu, and L. Zhuang, *An alkaline polymer electrolyte CO_2 electrolyzer operated with pure water,* Energy Environ. Sci. **12**, 2455 (2019).

[39] F. P. G. de Arquer, C.-T. Dinh, A. Ozden, J. Wicks, C. McCallum, A. R. Kirmani, D.-H. Nam, C. Gabardo, A. Seifitokaldani, X. Wang, *et al.*, *CO_2 electrolysis to multicarbon products at activities greater than 1 A cm^{-2},* Science **367**, 661 (2020).

[40] D. Bohra, J. H. Chaudhry, T. Burdyny, E. A. Pidko, and W. A. Smith, *Modeling the electrical double layer to understand the reaction environment in a CO_2 electrocatalytic system,* Energy Environ. Sci. **12**, 3380 (2019).

[41] N. Gupta, M. Gattrell, and B. MacDougall, *Calculation for the cathode surface concentrations in the electrochemical reduction of CO_2 in $KHCO_3$ solutions,* Journal of Applied Electrochemistry **36**, 161 (2006).

[42] S. Suter and S. Haussener, *Optimizing mesostructured silver catalysts for selective carbon dioxide conversion into fuels,* Energy Environ. Sci. **12**, 1668 (2019).

[43] M. Liu, Y. Pang, B. Zhang, P. De Luna, O. Voznyy, J. Xu, X. Zheng, C. T. Dinh, F. Fan, C. Cao, F. P. G. de Arquer, T. S. Safaei, A. Mepham, A. Klinkova, E. Kumacheva, T. Filleter, D. Sinton, S. O.

Kelley, and E. H. Sargent, *Enhanced electrocatalytic CO_2 reduction via field-induced reagent concentration,* Nature **537**, 382 EP (2016).

[44] J. Resasco, L. D. Chen, E. Clark, C. Tsai, C. Hahn, T. F. Jaramillo, K. Chan, and A. T. Bell, *Promoter effects of alkali metal cations on the electrochemical reduction of carbon dioxide,* Journal of the American Chemical Society **139**, 11277 (2017).

[45] G. O. Larrazábal, A. J. Martín, and J. Pérez-Ramírez, *Building Blocks for High Performance in Electrocatalytic CO_2 Reduction: Materials, Optimization Strategies, and Device Engineering,* The Journal of Physical Chemistry Letters **8**, 3933 (2017).

[46] A. S. Varela, M. Kroschel, T. Reier, and P. Strasser, *Controlling the selectivity of CO_2 electroreduction on copper: The effect of the electrolyte concentration and the importance of the local pH,* Catalysis Today **260**, 8 (2016), surface Analysis and Dynamics (SAND).

[47] R. Kas, R. Kortlever, H. Yilmaz, M. T. M. Koper, and G. Mul, *Manipulating the hydrocarbon selectivity of copper nanoparticles in CO_2 electroreduction by process conditions,* ChemElectroChem **2**, 354 (2015).

[48] M. Ma, K. Djanashvili, and W. A. Smith, *Controllable hydrocarbon formation from the electrochemical reduction of CO_2 over Cu nanowire arrays,* Angewandte Chemie International Edition **55**, 6680 (2016).

[49] M. Ma, B. J. Trześniewski, J. Xie, and W. A. Smith, *Selective and efficient reduction of carbon dioxide to carbon monoxide on oxide-derived nanostructured silver electrocatalysts,* Angewandte Chemie International Edition **55**, 9748 (2016).

[50] J. Giner and C. Hunter, *The mechanism of operation of the teflon-bonded gas diffusion electrode: A mathematical model,* Journal of The Electrochemical Society **116**, 1124 (1969).

[51] L.-C. Weng, A. T. Bell, and A. Z. Weber, *Modeling gas-diffusion electrodes for CO_2 reduction,* Phys. Chem. Chem. Phys. **20**, 16973 (2018).

[52] K. Wu, E. Birgersson, B. Kim, P. J. Kenis, and I. A. Karimi, *Modeling and experimental validation of electrochemical reduction of CO_2 to CO in a microfluidic cell,* Journal of The Electrochemical Society **162**, F23 (2015).

[53] M. S. Kilic, M. Z. Bazant, and A. Ajdari, *Steric effects in the dynamics of electrolytes at large applied voltages. II. Modified Poisson-Nernst-Planck equations,* Phys. Rev. E **75**, 021503 (2007).

[54] H. Wang, A. Thiele, and L. Pilon, *Simulations of cyclic voltammetry for electric double layers in asymmetric electrolytes: A generalized modified Poisson-Nernst-Planck model,* The Journal of Physical Chemistry C **117**, 18286 (2013).

[55] D. McLaughlin, M. Bierling, R. Moroni, C. Vogl, G. Schmid, and S. Thiele, *Tomographic reconstruction and analysis of a silver CO_2 reduction cathode,* Advanced Energy Materials **n/a**, 2000488 (2020).

[56] T. Haas, R. Krause, R. Weber, M. Demler, and G. Schmid, *Technical photosynthesis involving CO_2 electrolysis and fermentation,* Nature Catalysis **1**, 32 (2018).

[57] S. Verma, Y. Hamasaki, C. Kim, W. Huang, S. Lu, H.-R. M. Jhong, A. A. Gewirth, T. Fujigaya, N. Nakashima, and P. J. Kenis, *Insights into the low overpotential electroreduction of CO_2 to CO on a supported gold catalyst in an alkaline flow electrolyzer,* ACS Energy Letters **3**, 193 (2017).

[58] S. Ma, R. Luo, J. I. Gold, Z. Y. Aaron, B. Kim, and P. J. Kenis, *Carbon nanotube containing ag catalyst layers for efficient and selective reduction of carbon dioxide,* Journal of Materials Chemistry A **4**, 8573 (2016).

[59] E. J. Dufek, T. E. Lister, S. G. Stone, and M. E. McIlwain, *Operation of a pressurized system for continuous reduction of CO_2,* Journal of The Electrochemical Society **159**, F514 (2012).

[60] R. B. Bird, W. E. Stewart, and E. N. Lightfoot, in *Transport Phenomena, Revised 2nd Edition* (Wiley, 2006) pp. 671–725.

[61] S. Weisenberger and A. Schumpe, *Estimation of gas solubilities in salt solutions at temperatures from 273 K to 363 K,* AIChE Journal **42**, 298 (1996).

[62] T. Burdyny, P. J. Graham, Y. Pang, C.-T. Dinh, M. Liu, E. H. Sargent, and D. Sinton, *Nanomorphology-enhanced gas-evolution intensifies CO_2 reduction electrochemistry,* ACS Sustainable Chemistry & Engineering **5**, 4031 (2017).

[63] J. van Brakel and P. Heertjes, *Analysis of diffusion in macroporous media in terms of a porosity, a tortuosity and a constrictivity factor,* International Journal of Heat and Mass Transfer **17**, 1093 (1974).

[64] J. B. Hasted, D. M. Ritson, and C. H. Collie, *Dielectric properties of aqueous ionic solutions. Parts I and II,* The Journal of Chemical Physics **16**, 1 (1948).

[65] J. O. Bockris and A. K. Reddy, *Volume 1: Modern Electrochemistry*, 2nd ed. (Springer US, 1998).

[66] M. S. Alnæs, J. Blechta, J. Hake, A. Johansson, B. Kehlet, A. Logg, C. Richardson, J. Ring, M. E. Rognes, and G. N. Wells, *The FEniCS project version 1.5,* Archive of Numerical Software **3**, 9 (2015).

[67] A. Logg, K.-A. Mardal, G. N. Wells, *et al.*, *Automated Solution of Differential Equations by the Finite Element Method* (Springer, 2012).

[68] S. Nitopi, E. Bertheussen, S. B. Scott, X. Liu, A. K. Engstfeld, S. Horch, B. Seger, I. E. L. Stephens, K. Chan, C. Hahn, J. K. NÃžrskov, T. F. Jaramillo, and I. Chorkendorff, *Progress and perspectives of electrochemical CO_2 reduction on copper in aqueous electrolyte,* Chemical Reviews **119**, 7610 (2019).

[69] R. Kas, K. Yang, D. Bohra, R. Kortlever, T. Burdyny, and W. A. Smith, *Electrochemical CO_2 reduction on nanostructured metal electrodes: fact or defect?* Chem. Sci. **11**, 1738 (2020).

[70] E. L. Clark, J. Resasco, A. Landers, J. Lin, L.-T. Chung, A. Walton, C. Hahn, T. F. Jaramillo, and A. T. Bell, *Standards and protocols for data acquisition and reporting for studies of the electrochemical reduction of carbon dioxide,* ACS Catalysis **8**, 6560 (2018).

[71] C. Lee, B. Zhao, J. K. Lee, K. F. Fahy, K. Krause, and A. Bazylak, *Bubble formation in the electrolyte triggers voltage instability in CO_2 electrolyzers,* iScience , 101094 (2020).

[72] C.-H. Hou, P. Taboada-Serrano, S. Yiacoumi, and C. Tsouris, *Monte carlo simulation of electrical double-layer formation from mixtures of electrolytes inside nanopores,* The Journal of Chemical Physics **128**, 044705 (2008).

[73] S. T. Cui and H. D. Cochran, *Molecular dynamics simulation of interfacial electrolyte behaviors in nanoscale cylindrical pores,* The Journal of Chemical Physics **117**, 5850 (2002).

[74] C. Lian, D.-e. Jiang, H. Liu, and J. Wu, *A generic model for electric double layers in porous electrodes,* The Journal of Physical Chemistry C **120**, 8704 (2016).

[75] J. H. Bae, J.-H. Han, and T. D. Chung, *Electrochemistry at nanoporous interfaces: new opportunity for electrocatalysis,* Phys. Chem. Chem. Phys. **14**, 448 (2012).

[76] G. Feng, R. Qiao, J. Huang, B. G. Sumpter, and V. Meunier, *Ion distribution in electrified micropores and its role in the anomalous enhancement of capacitance,* ACS Nano **4**, 2382 (2010).

[77] V. Joekar-Niasar, · . L. Schreyer, · . M. Sedighi, M. Icardi, and J. Huyghe, *Coupled processes in charged porous media: From theory to applications,* Transport in Porous Media **130**, 183 (2019).

7

Future perspective

The results in this thesis address important questions at different length scales within the eCO_2R system. Electrochemical conversion of CO_2 is a complex multiscale challenge and necessitates such an hierarchical approach to both simulations and experimental research. Like with most research endeavors, our results answer some questions while posing some others. What is the accuracy of *ab-initio* DFT simulations for different levels of model complexity? What properties of the reaction interface are essential to reliably model reaction energetics? Is bulk diffusion sufficient to understand the transport of CO_2 to the catalyst surface or does EDL influence its transport? What are the repercussions of ion-specificity in the non-ideal EDL region? How are the gas-liquid interfaces distributed in a GDE-based flow cell device and how can they be manipulated? What is the morphology and structural parameters of a typical catalyst layer deposited on a GDE? What are the implications of the accumulation of ionic species within catalytic pores of a flow-cell device? These are some of the important questions that appear through the analysis presented in this thesis. And we hope that they will be the subject of future research activities in the area.

Society needs to reach net-zero CO_2 emissions along with a drastic reduction in non-CO_2 GHG emissions within the next three decades. To put the time period in perspective, there has been a consensus in the scientific community on the warming effect of anthropogenic CO_2 emissions since the late 1980s, that is, more than three decades ago. Meanwhile, in this

period, the total CO_2 emissions have steadily increased from ~20,500 Mt in 1990 to ~32,800 Mt in 2017. Climate change mitigation is therefore, to a large extent, a *political* problem rather than a purely technical challenge. The price associated with emitting CO_2, policy incentives for transitioning to a renewable electricity grid and financial support for development of new technologies will all have a major influence on the feasibility of eCO_2R and CCU in general.

If feasible, and deployed at large scale, eCO_2R has the potential to be an enabler for renewable grid management and a source for a low-carbon form of essential hydrocarbon molecules. Developments in fuel-cell-inspired GDE devices promise to bring the eCO_2R technology closer to commercial feasibility. eCO_2R has therefore entered an exciting era where not just academia, but also commercial players have started to play an active role. However, it is important that CCU technologies are not used or communicated as a means to circumvent the elimination of CO_2 emissions where it is possible. Also, carbon dioxide reduction technologies do not necessarily guarantee a reduction in emissions over the life cycle of the process, and this should be thoroughly assessed using appropriate methodologies within the context of the specific application. Not emitting more CO_2 molecules will remain the most effective strategy to combat global warming. The promise of CCU is, after all, akin to fire-fighting and a testament to the failure of our society and its leadership to act in a timely manner to the crisis of climate change.

A

The competition between two-electron reduction products

A.1. Experimental Methods: SERS

All experiments were carried out in a three-electrode cell configuration: a flame-annealed silver wire served as counter electrode, an eDAQ leak-less Ag/AgCl electrode was used as reference electrode, and a home-made silver electrode (99.999% pure Ag) was designed in a L-shape as a working electrode surface, orthogonal to the laser probe for Raman spectra acquisition. The electrolyte solutions were freshly prepared using Millipore MilliQ water (resistivity > 18.2 MΩ.cm), and the reactants used are listed as lithium tetraborate (99.995% trace metals basis, Sigma-Aldrich), boric acid (99.9999 Suprapur, Sigma-Aldrich) and KCl (anhydrous, beads, trace metals basis, Sigma-Aldrich). Argon (5.5) and carbon dioxide (6.0) gases were purchased from Linde.

Prior to experiments, the glassware was cleaned by boiling it in a 1:1 mixture of concentrated sulfuric and nitric acids, rinsed thoroughly, and

This appendix has been published as supplementary information in Angew. Chem. Int. Ed. **58**, 1345 (2019) [1].

Computational research work led by D. Bohra and supervised by G. Li and E. A. Pidko; Experimental research work led by I. Ledezma-Yanez and supervised by W. de Jong; W. A. Smith supervised the project as the principal investigator.

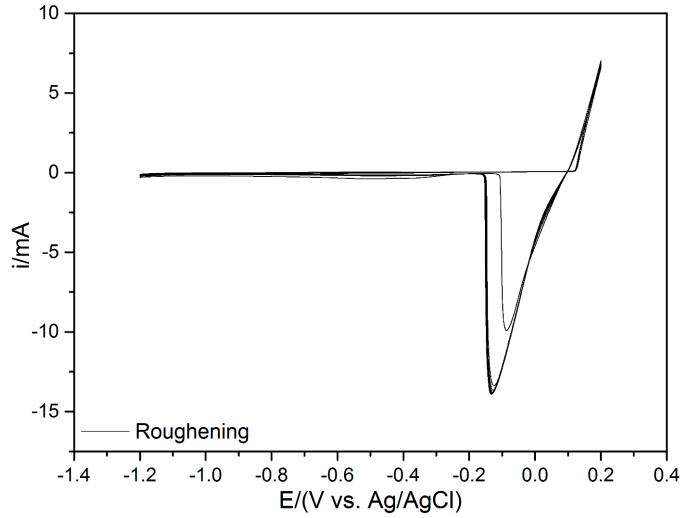

Figure A.1: Cyclic voltammograms recorded during the Ag roughening in KCl 0.1 M

boiled with Millipore MilliQ water five times for each time we changed electrolyte. It was kept in the oven at 90 °C when not in use. The working electrode was polished mechanically to mirror finish with alumina of three different meshes, in descending order of grain size: 1 μm, 0.5 μm and 0.03 μm. A 10:90 ethanol/water mixture was prepared to clean the electrode from alumina traces by applying an ultrasonic bath for 15 minutes. After this treatment, the electrode was rinsed with abundant ultrapure water and used as is for recording cyclic voltammograms. For surface-enhanced Raman probing, a roughening procedure was used to generate a plasmonic surface on the working electrode: 26 consecutive oxidation/reduction cycles with a 1.5 s step at 0.2 V vs. Ag/AgCl per each cycle, in a 0.1 M KCl solution. The voltammograms recorded are shown in Figure A.1. Cyclic voltammograms and potential control were recorded using a BioLogic SP-200 potentiostat/galvanostat, whereas the surface-enhanced Raman measurements were collected using a RAMANRXN2 multichannel-532 from Kaiser Optical Systems, with a 532 nm Invictus™VIS laser (100 mW), with a spectral resolution of 5 cm^{-1}. A total of 20 interferograms were collected in an interval of 120 s per each measurement.

Figure A.2 shows the blank cyclic voltammograms obtained from the

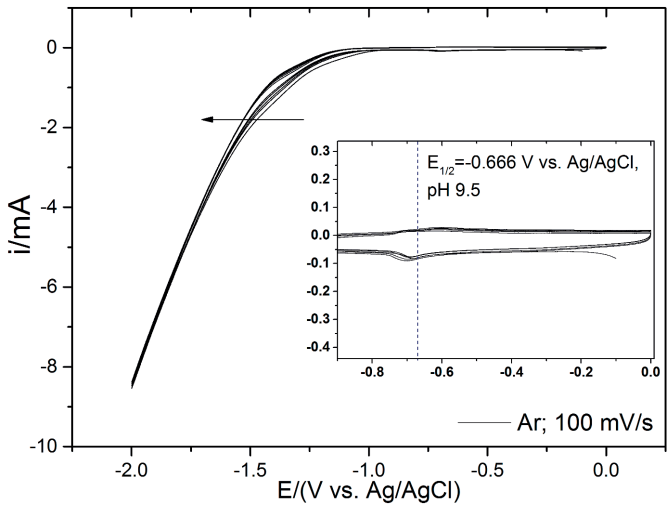

Figure A.2: Cyclic voltammograms recorded in $Li_2B_4O_7$ 0.05 M under argon atmosphere (5 scans).

silver electrode in 0.05 M $Li_2B_4O_7$ solution purged with argon (pH=9.5). A total of five scans were recorded in a cathodic working window of 2 V, at a scan rate of 100 mV/s. A redox couple with a reduction peak ca. -0.66 V vs. Ag/AgCl is shown in the insert of Figure A.2. This feature corresponds to the formation of LiOH on the electrode surface due to the high pH of the solution. Still, no significant shift in pH, current or shape is observed after the five scans, suggesting that the formation of LiOH does not affect the active sites for hydrogen evolution nor the interfacial pH in an irreversible way.

Figure A.3 contains the cyclic voltammograms recorded on a silver electrode in 0.05 M $Li_2B_4O_7$ solution, saturated with carbon dioxide under continuous CO_2 flux (pH=6.1; carbonic acid regime). The scan rate used was 20 mV/s, in a 2 V working window with a pH correction of 180 mV/Dec pH when compared to the original electrolyte (pH=9.5). The voltammograms shift towards cathodic potentials after each consecutive cycle, evidencing the pH change on the electrode interface due to the water decomposition into hydrogen and hydroxyl groups. This translates into a more alkaline interface; 6.1< pH <9.5, since the LiOH redox couple is not observed as in Figure A.2. The insert in Figure A.3 shows a reduction peak

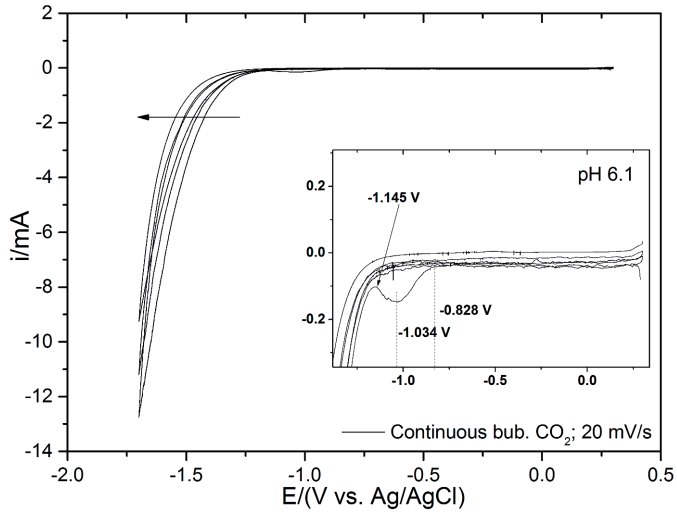

Figure A.3: Cyclic voltammograms recorded in $Li_2B_4O_7$ 0.05 M under CO_2 atmosphere (continuous bubbling; 3 scans).

with an onset potential at -0.828 V vs. Ag/AgCl (ca. -1.2 V vs RHE), attributed to CO_2 reduction in the first scan. The second and third scans are featureless. Although the current is not normalized per surface area, the geometrical area of the electrode is the same for the voltammograms presented in Figures A.2 and A.3, suggesting that the current in presence of dissolved CO_2 is larger when compared to that obtained under argon atmosphere, provided the correction for applied potential. The pH increase translates into an increase of the free energy, decreasing with this the thermodynamic driving force of the reaction. Figure A.4 shows the cyclic voltammetries from Figures A.2 and A.3 with the measured potentials corrected for pH.

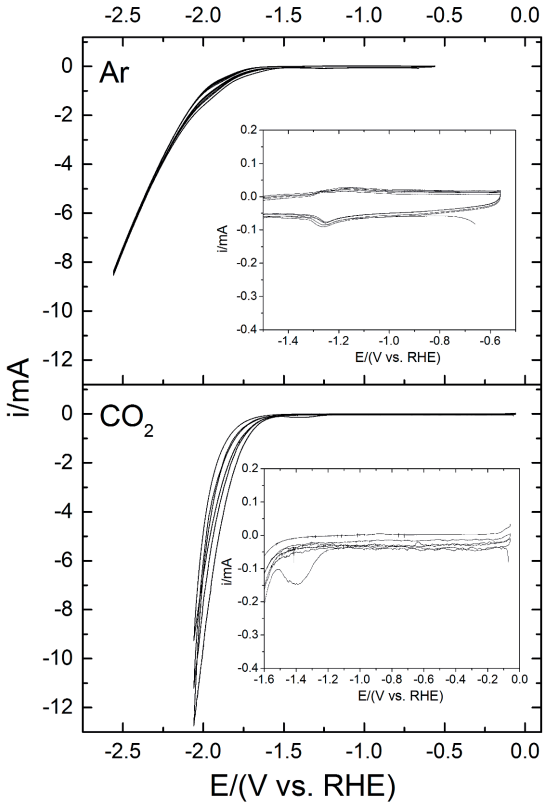

Figure A.4: Cyclic voltammograms recorded in $Li_2B_4O_7$ 0.05 M under Ar and CO_2 atmospheres respectively (same data as in Figures A.2 and A.3) with potentials corrected for pH and reported vs RHE.

A.2. Supporting Results

A.2.1. SERS measurements

This section provides spectroscopic data collected from the electrochemical CO_2 reduction performed on a silver electrode immersed in a 0.05 M $Li_2B_4O_7$ solution, saturated with CO_2. The electrolyte choice plays an important role in the stabilization of intermediates, given the fact that alkali metals modify the surrounding water networks by affecting the entropy of solvation at the electrode interface. We choose an electrolyte containing lithium ions (high electronic affinity) to facilitate the proton transfer to

the surface and the formation of dipoles necessary to stabilize the short-lived intermediates during the measurements, since CO_2ER proceeds in a low proton availability regime (pH>3).

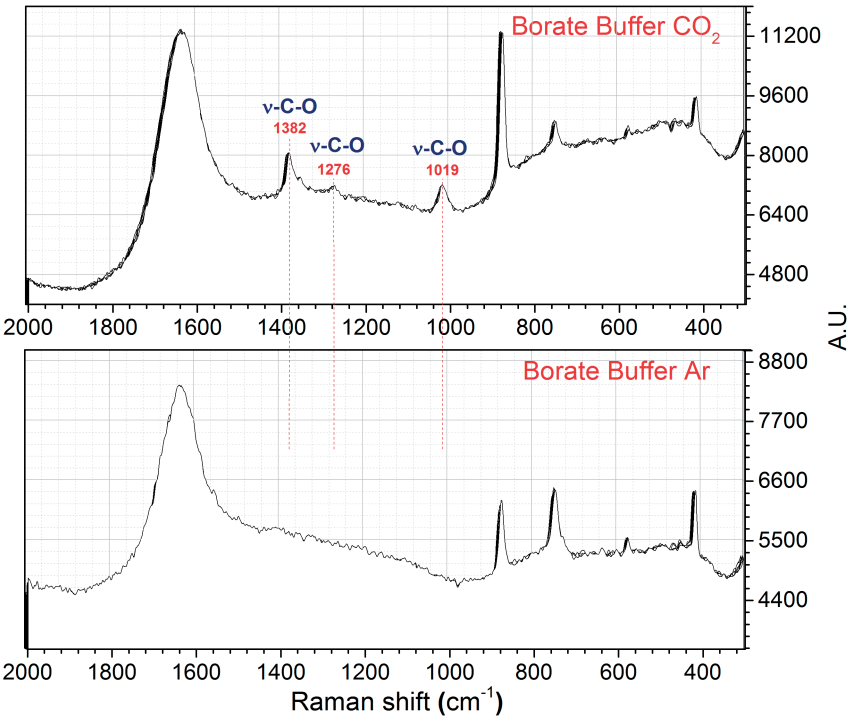

Figure A.5: Raman measurements recorded in 0.05 M borate buffer solutions under Ar atmosphere and CO_2 saturation, respectively.

Prior the electrocatalysis, transmission Raman spectra from the solutions were collected to identify the formation of the carbonated species in the electrolyte, compared with the solutions saturated with argon. Figure A.5, bottom panel, shows the transmission spectra collected from 0.05 M borate buffer solutions, with an initial pH=9.0. The solution was saturated with argon, with no pH change, as expected. The water bending can be observed ca. 1630 cm^{-1} and the bands ca. 850, 750 and 420 cm^{-1} are attributed to buffer solution. The spectra corresponding to the borate buffer saturated with CO_2 is shown in the top panel of Figure A.5. The pH decreased to 6.1 after one hour of constant CO_2 bubbling, confirming

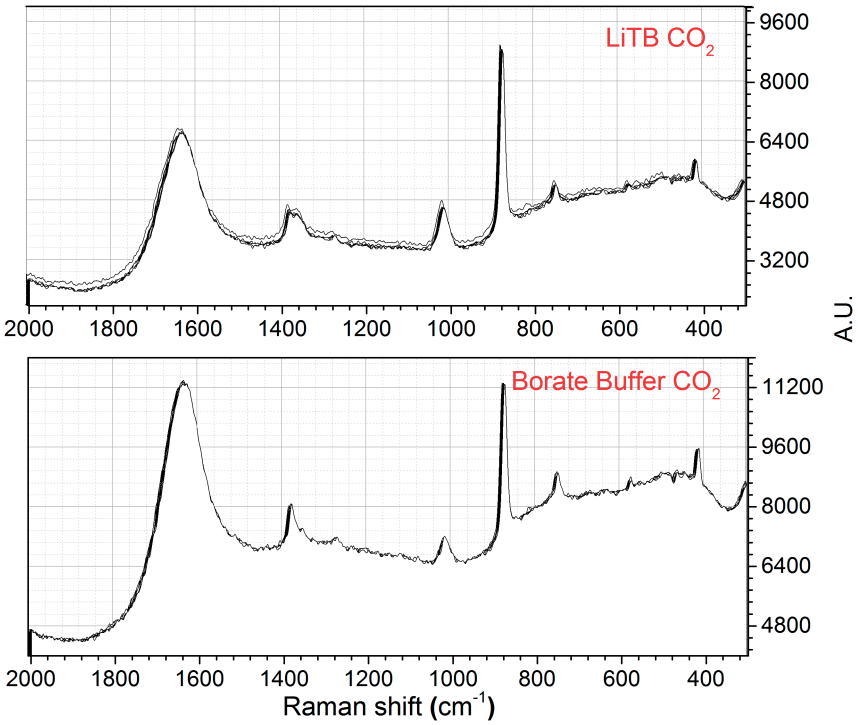

Figure A.6: Raman measurements recorded in 0.05 M $Li_2B_4O_7$ and 0.05 M borate buffer solutions saturated with CO_2; pH 6.1.

the acidification of the solution (formation of carbonic acid as solvated CO_2). Raman shift frequencies corresponding to the presence of dissolved CO_2 are identified as 1382 cm^{-1} from ν CO_2, 1276 cm^{-1} from δ C-OH, and 1019 cm^{-1} as ν C-OH from HCO_3^- [2]. Figure A.6 shows the comparison of the spectra collected for 0.05 M $Li_2B_4O_7$ and 0.05 M borate buffer solutions saturated with CO_2. The spectra reveal the same bands for both solutions at the final measured pH=6.1, suggesting that the equilibrium between carbonate/bicarbonate in lithium tetraborate and boric acid behaves in a similar way.

We present the full spectra collected for in-situ SERS for CO_2ER on polycrystalline Ag in Figure A.7. The most prominent bands are shown in the region 3600 - 3000 cm^{-1}, corresponding to the water, followed by C−H interactions between 3000 - 2650 cm^{-1}. Due to its complexity, the

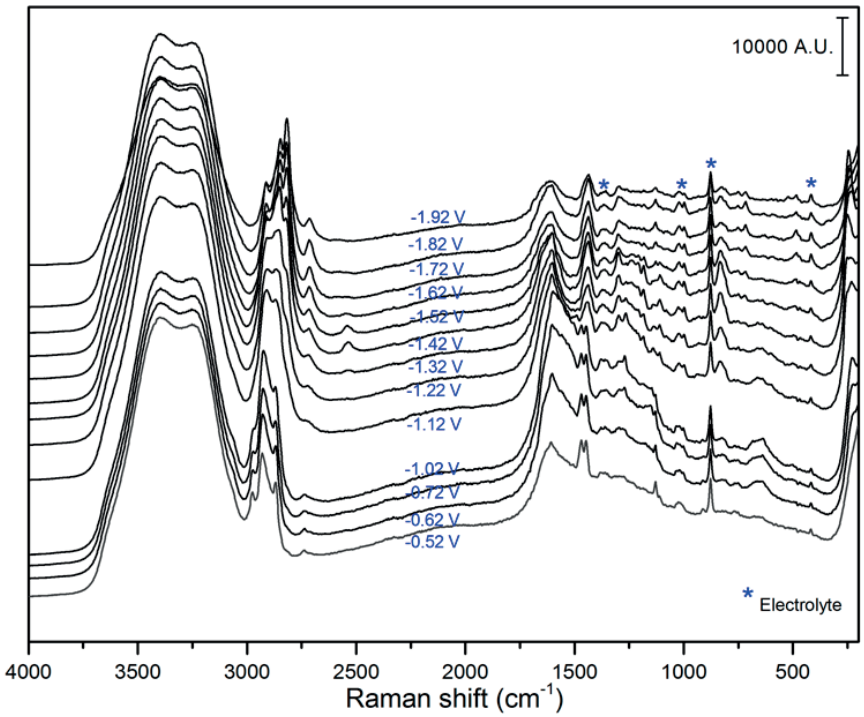

Figure A.7: SERS measurements recorded as a function of applied potential in 0.05 M $Li_2B_4O_7$ saturated with CO_2 at bulk pH 6.1.

region between 1750 - 200 cm^{-1} is presented in three different sections: the 1750 - 1300 cm^{-1} region corresponds to Figure 4.10 in the chapter 4, and the 1100 - 400 cm^{-1} and the 300 - 200 cm^{-1} regions are shown with our band assignments in Figures A.8 and A.9, respectively. For the figures used for band assignment, the electrolyte was subtracted using a SERS spectrum taken at open circuit potential.

From Figure A.7 the most prominent bands correspond to water stretching and water bending, observed at 3000 - 3750 cm^{-1} and 1630 cm^{-1} respectively. In this raw full spectra it is shown how strong the baseline distortion is from the water deformation, although it may have a more complex origin related to an artifact that we cannot discard. Nonetheless, when we approach more cathodic potentials (-1.12 V), we observe the formation of other species (See Figure A.8, region 600 - 700 cm^{-1}) and the shifting of bands that concertedly happen with an ease or relaxation of

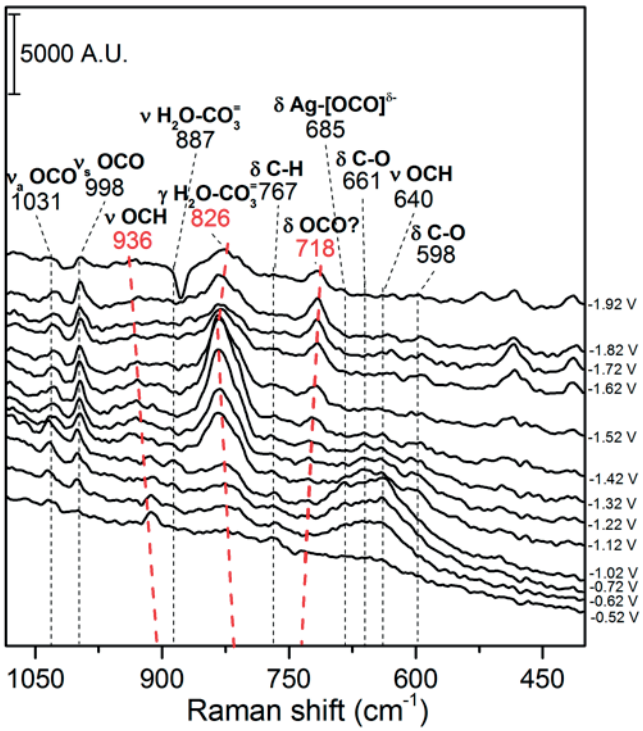

Figure A.8: Zoomed-in SERS measurements recorded as function of applied potential in 0.05 M $Li_2B_4O_7$ saturated with CO_2 at bulk pH 6.1. Raman shift region: 1100 - 400 cm^{-1}.

these baseline deformations. We believe that these phenomena are related to H-bond breaking and making, which becomes quite slow in presence of electrolytes with pH higher than 3, when the hydrogen evolution depends on protons from water and the stabilization capacity of the catalyst, aided by cation solvation processes.

We probed polycrystalline Ag catalyst surface during CO_2ER using in-situ electrochemical SERS measurements in 0.05 M $Li_2B_4O_7$ [3, 4] saturated with CO_2, with a bulk pH of 6.1. We assign the bands at 1436 and 1469 cm^{-1} to an O-bound bidentate intermediate on the Ag surface, which we believe corresponds to $*$OCHO (Figure 4.10 in chapter 4). Evidence of an O-bound bidentate configuration with a similar double-band shape and spectral region has been discussed previously for carboxylate

species on silver hydrosols studied with SERS [5]. Factors such as the applied electric field, interaction with the other surface species, the protonated carbon atom as opposed to the carboxylate species reported by Kai *et al.* [5], will affect the frequency at which the bidentate double-band appears. The anti-Stark effect can explain the 1469 cm^{-1} band shift towards slightly negative frequencies, with the so-called resonance transfer among species containing C=O groups being another potential cause for this shift [6, 7]. As we approach more cathodic potentials (-1.12 V), the bidentate signal merges into a broader band and a new band forms at 1298 cm^{-1}, corresponding to a δC−H vibration [8].

In the case of the formation of a monodentate configuration, a band should appear at 1567 cm^{-1} (denoted with a red dotted line in Figure 4.10 in chapter 4). However, the baseline deformation is strong and the observation is inconclusive. The species I_1 in Figure 4.6 shows the configuration of a monodentate O-bound species formed along the reaction path in the CI-NEB calculation leading to the more stable bidentate intermediate ∗OCHO. In our geometrical optimization calculations, we find that the species I_1, or ∗HCOO, can be metastable in the sense that the potential energy surface is flat in the vicinity of this configuration. We suspect that at high overpotentials, the monodentate species ∗HCOO can be stabilized to a greater extent due to a stronger Ag−H interaction and solvation by tightly bound interfacial water molecules. It is worth noting that the solvation energy of ∗HCOO is significantly higher than for the ∗OCHO species in the absence of electric field (Table S1). According to the theoretical calculations, there is a prerequisite Volmer step in order for the O-bound ∗OCHO intermediate to form. The baseline distortions observed experimentally in the water deformation region may be linked to the occurrence of this Volmer step in addition to the effect of polarized species on the dipole moment of the interfacial water molecules.

Zooming in into the 1100 - 400 cm^{-1} region of the full spectra shown in Figure A.7, (Figure A.8), we identify several vibrational modes from species related to the CO_2ER, confirming that the catalysis is taking place. The prominent features are related to O−C and O−C−O species, and the band assignment was made based on previous reports for Raman spectroscopy analysis performed for liquid samples and SERS analysis on silver substrates [2, 5, 8].

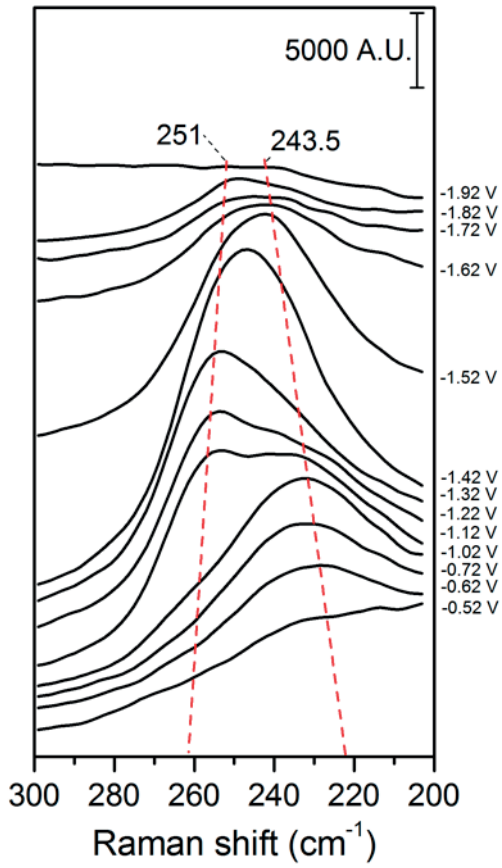

Figure A.9: Zoomed-in SERS measurements recorded as function of applied potential in 0.05 M $Li_2B_4O_7$ saturated with CO_2 at bulk pH 6.1. Raman shift region: 300 - 200 cm^{-1}.

Figure A.9 shows the 300 - 200 cm^{-1} region of the SERS spectra shown in Figure A.7. There are strong bands present at 243.5 and 251 cm^{-1} (Figure A.9), that can be attributed to Ag−O interactions with the carbonated species formed from the CO_2ER. The absence of νAg−O bands at 330, 470 and 860 cm^{-1} reported previously [9] rule out the formation of surface oxides and hydroxides, reinforcing our band assignment of the O-bound species.

From the spectra in Figure A.10, we observe no CO formation until -2.02 V vs. RHE, presented as a function of time with a fixed applied

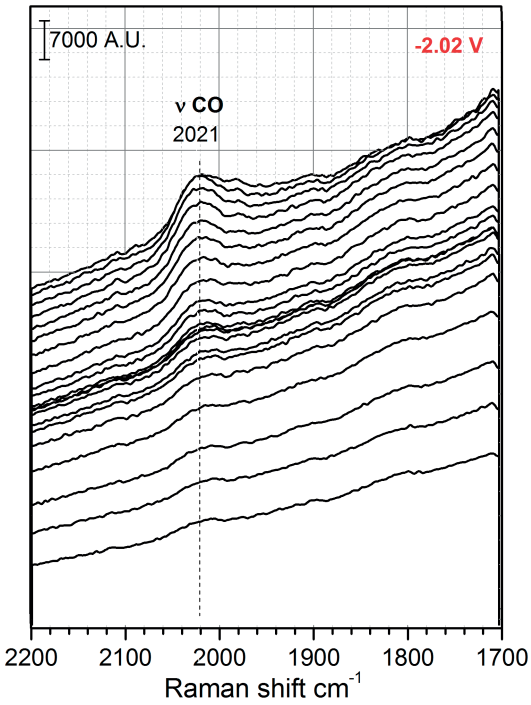

Figure A.10: Zoomed-in SERS measurements recorded as function of time in 0.05 M $Li_2B_4O_7$ saturated with CO_2 at bulk pH 6.1. At the applied potential of -2.02 V we observe the formation of CO at 2021 cm^{-1}.

potential.

SERS experiments for CO_2ER on polycrystalline silver were performed in lithium borate buffer solutions, pH 6.9, and are shown in Figure A.11. The region corresponds to 1750 - 300 cm^{-1} and shows the bands from the electrolyte solution as well as the water bending. At -2.03 V vs. RHE, we observe the formation of a double band: 1442 and 1421 cm^{-1} attributed to a O−(CH)−O vibration bonded to the Ag through both oxygen atoms, as can also bee seen in Figure 4.10 in chapter 4. We also observe the concerted formation of a band at 1298 cm^{-1} corresponding to a C−H deformation [8], and a band at 1162 cm^{-1} associated with the bidentate species. These experiments suggest that pH plays a role in CO_2ER at lower overpotentials due to its dependence on the hydride formation on the Ag electrode. The C−H band as seen in Figure 4.10 in chapter 4

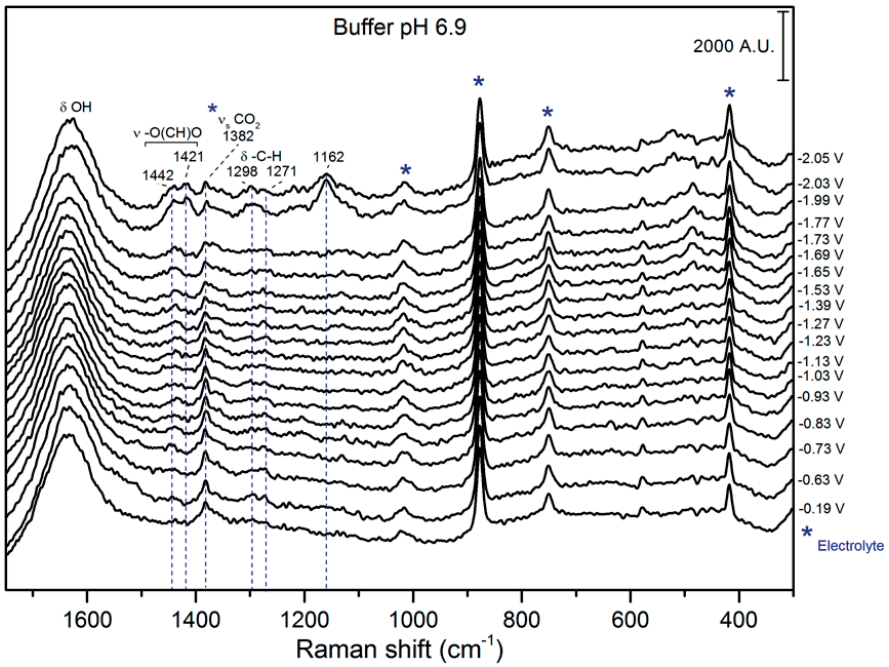

Figure A.11: Zoomed-in SERS measurements recorded as function of time in 0.05 M borate buffer saturated with CO_2 at bulk pH 6.9. Raman shift region: 1750 - 300 cm^{-1}.

for the 0.05 M $Li_2B_4O_7$ buffer (pH 6.1) is also formed in presence of the borate buffer solution as shown in Figure A.11, along with the formation of the bidentate species at high overpotentials, indicating a correlation in the formation of these species.

Figure A.11 also shows a unique band at 1382 cm^{-1} from -0.19 V vs.RHE which is attributed to νCO_2 by Rudolph *et al.* [2]. This band is also observed in the transmission spectra of our CO_2-saturated electrolyte solution (see Figures A.5 and A.6), and corresponds to one of the two νCOO^- bands assigned by Kai *et al.* [5] for bidentate carboxylate. The appearance of bands at 1442 and 1421 cm^{-1} at -2.06 V in Figure A.11 present a slight baseline deformation while the hydrogen evolution is occurring suggesting that, firstly, the band we assign as bidentate is independent from the 1382 cm^{-1} band, hence the coexistence; and secondly, there is a sensitivity to hydrogen population on the electrode surface in

order for the 1442 and 1421 cm^{-1} species to form. Note that there is also a frequency shift of these bands when compared to the bidentate species assigned in Figure 4.10 in chapter 4, showing how slight changes in the measurement conditions (bulk pH in this case) may lead to frequency shifts.

A.2.2. Computational results

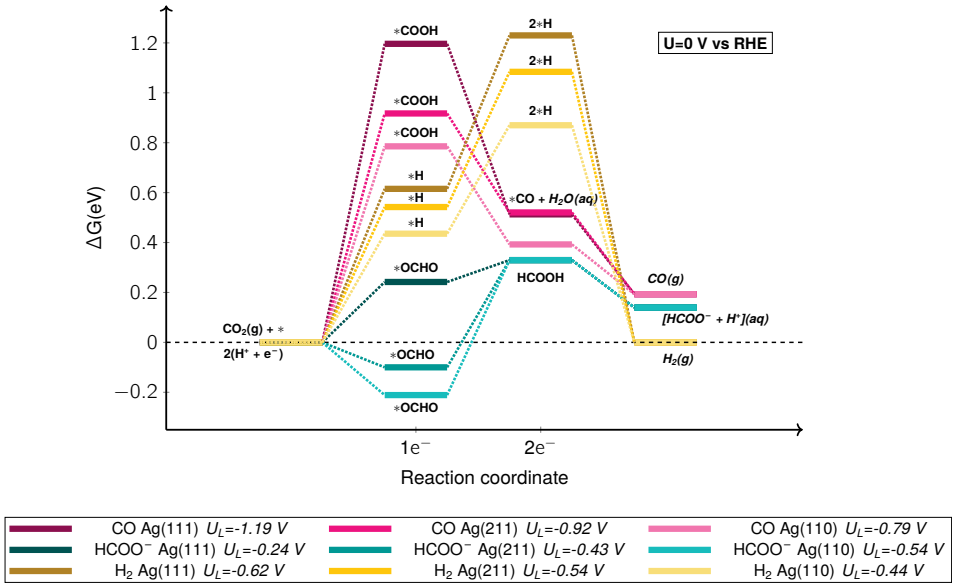

Figure A.12: Free energy plot showing CO(g) and $HCOO^-$(aq) formation pathways for (111), (211) and (110) Ag surfaces. The limiting potentials (U_L) are vs. RHE. The free energy values have been corrected for solvation (see Table A.1).

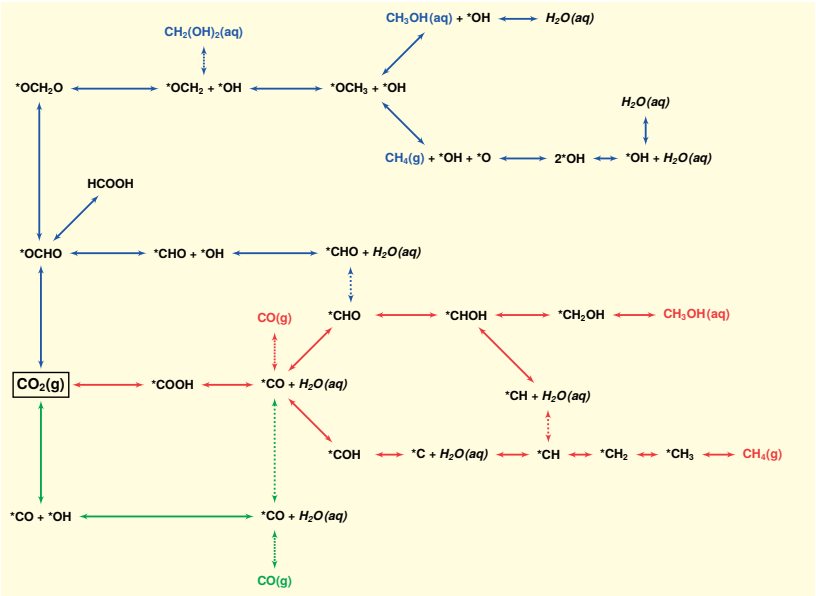

Figure A.13: A schematic of the proposed general reaction network for eCO_2R. Network colored blue goes via $*OCHO$ intermediate, red goes via $*COOH$ intermediate and green pathway leads to the direct formation of $*CO+*OH$ by breaking of the C−O bond on protonation of the O atom. Colored molecules are product molecules from the respective pathways whereas black molecules are surface bound intermediates. Dotted arrows denote merging of one pathway with another.

Figure A.14 shows the influence of the various corrections to the activation barriers calculated using CI-NEB calculations. The values of U^o (the potential for which equation (4.7) is at equilibrium) is different for every plot in Figure A.14 due the the different potentials needed to bind $*H$ exergonically depending on the level of corrections applied to E^{DFT}. Solvation correction has a significant influence on the activation barrier for formation of $*OCHO$ whereas the free energy corrections have a significant influence on the relative activation barriers of the Tafel and Heyrovsky H_2 production steps. Without the free energy corrections, the Heyrovsky step seems considerably more favorable than the Tafel step however, the two barriers become very similar on performing the corrections. The effect of the corrections on the barrier for $*COOH$ formation is limited and the barrier remains $\sim$1 eV.

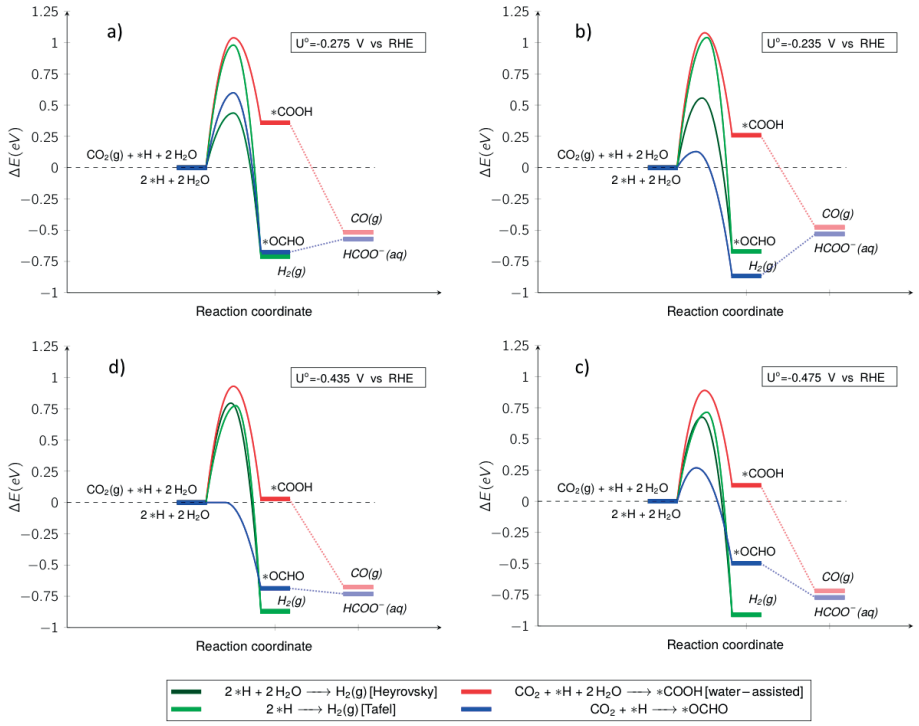

Figure A.14: a) Activation barriers without any corrections (only E^{DFT}). b) Activation barriers corrected for only solvation (E^{DFT} - E_{solv}). c) Activation barriers corrected for vibrational entropy, enthalpy, zero point energy as well a systematic DFT functional errors but not solvation or in other words the free energy of activation in vacuum ($E^{DFT} + E^{ZPVE} + \int_{T=0}^{T} C_p dT$ - $TS^{vib} + E_{xc}$). d) Free energy of activation corrected for solvation ($E^{DFT} + E^{ZPVE} + \int_{T=0}^{T} C_p dT$ - $TS^{vib} + E_{xc}$ - E_{solv}) same as Figure 4.9 in chapter 4.

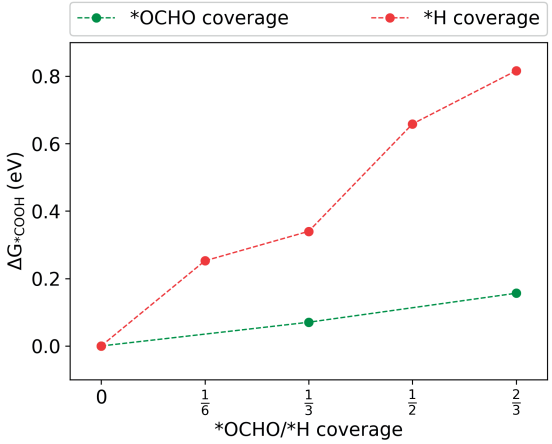

Figure A.15: Change in the binding energy of ∗COOH for different coverages of ∗OCHO (green data points) and ∗H (red data points). 0 eV on the y-axis corresponds to only ∗COOH present on the Ag(110) surface.

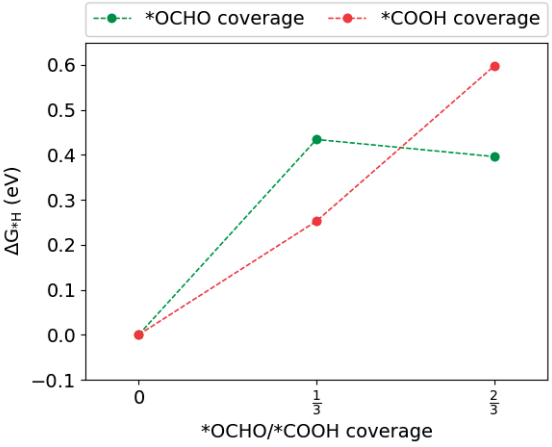

Figure A.16: Change in the binding energy of ∗H for different coverages of ∗OCHO (green data points) and ∗COOH (red data points). 0 eV on the y-axis corresponds to only ∗H present on the Ag(110) surface.

A coverage of 1 for ∗OCHO in Figure A.17a corresponds to a bi-dentate configuration on on-top sites across the short-bridge for a 2x3x6 (110) surface, a bi-dentate configuration on step sites for a 3x3x4 (211) surface and a bi-dentate configuration on on-top sites for a 3x3x4 (111) surface. Correspondingly, A coverage of 1 for ∗COOH in Figure A.17b corresponds to a bi-dentate (C and O bound) configuration on on-top sites across the long-bridge for a 2x3x6 (110) surface, a bi-dentate (C and O bound) configuration on step sites for a 3x3x4 (211) surface and a mono-dentate (C bound) configuration on on-top sites for a 3x3x4 (111) surface. ∗H is present on the short-bridge site for (110), the bridge of the step for (211) and in an fcc hollow site for (111). These configurations are found to be the most stable for the ∗OCHO, ∗COOH and ∗H on the respective surfaces. The most stable adsorbate configurations on Ag(111) are used for Figure A.18. Geometrical optimization is performed on all configurations as described previously.

It can be seen from Figure A.17a that the effect of the presence of ∗OCHO on the binding energy of ∗H is highly pronounced on a (110) surface and the influence diminishes as the surface becomes less active in the order (110)>(211)>(111) (see Figure A.12). However, the trend in the change in ΔG_{*H} due to the presence of ∗COOH does not seem to correlate with the binding strength of adsorbates with the facet and is similar for (110), (211) and (111) surfaces (Figure A.17b).

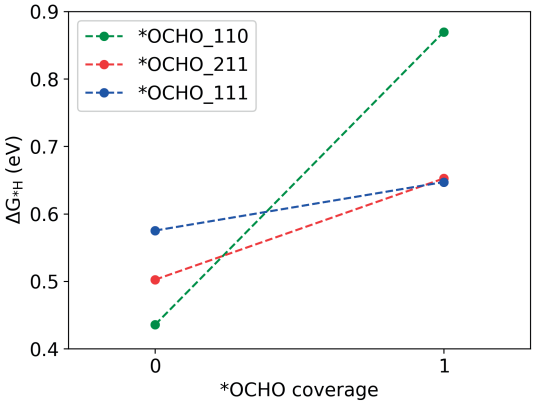

(a)

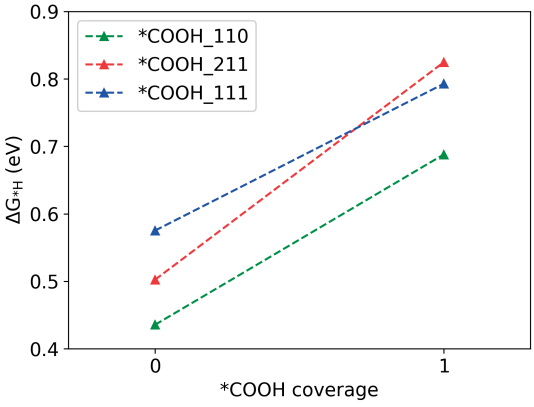

(b)

Figure A.17: Change in the binding energy of ∗H in the presence of ∗OCHO (a) and ∗COOH (b) for Ag(110), Ag(211) and Ag(111) surfaces. The binding free energy value for 0 coverage of ∗OCHO/∗COOH corresponds to the binding energy of *H on the respective surfaces.

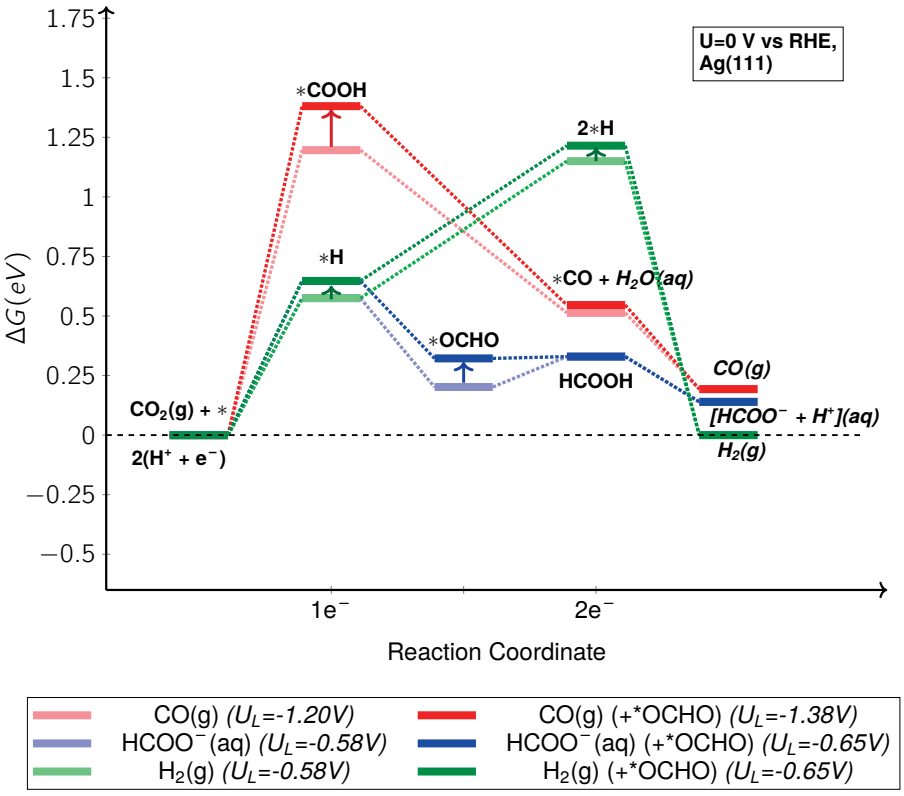

Figure A.18: Free energy diagram for formation of CO(g), $HCOO^-$(aq) and H_2(g) on Ag(111) surface at 0 V vs. RHE. The adsorption energies shown in dark red, blue and green are in the presence of ∗OCHO (θ=2/9), whereas the energies in light red, blue and green are without ∗OCHO. The upward arrows denote the change in free energy of the respective intermediates due to the presence of ∗OCHO on the surface. Formation of ∗OCHO has been shown to occur following the formation of ∗H as per the proposed mechanism and is not an electron transfer step. Limiting potentials (U_L) are given vs. RHE.

A

$*X$	E_{solv} in eV
CO_2 + *H + $2H_2O$	-0.32
*COOH	-0.19
*COOH + $2H_2O$	-0.42
*H	-0.04
2*H + $2H_2O$	-0.54
*CO	-0.02
*OH	-0.04
*OCHO	-0.23
*HCOO (I_1)	-0.70
*CO + *OH	-0.05
*C	-0.06
*CH	-0.01
*CH_2	-0.01
*CH_2OH	-0.19
*CH_3	-0.04
*CHO	-0.1
*CHOH	-0.05
*COH	-0.31
*OCH_2	-0.17
*OCH_2O	-0.19
*OCH_3	-0.09
*OCHO + *COOH	-0.37
TS species	E_{solv} in eV
*$COOH^{TS}$	-0.28^{**}
*$OCHO^{TS}$	-0.59
$H^{TS}_{2_{tafel}}$	-0.02
$H^{TS}_{2_{heyrovsky}}$	-0.42^{**}

Table A.1: Solvation energies for intermediate and transition state species calculated using implicit solvation method. **Include the two participating explicit water molecules.

References

[1] D. Bohra, I. Ledezma-Yanez, G. Li, W. de Jong, E. A. Pidko, and W. A. Smith, *Lateral adsorbate interactions inhibit $HCOO^-$ while promoting CO selectivity for CO_2 electrocatalysis on silver,* Angewandte

Chemie International Edition **58**, 1345 (2019).

[2] W. W. Rudolph, G. Irmer, and E. Konigsberger, *Speciation studies in aqueous HCO_3^--CO_3^{2-} solutions. A combined Raman spectroscopic and thermodynamic study,* Dalton Trans. , 900 (2008).

[3] I. Ledezma-Yanez, W. D. Z. Wallace, P. Sebastián-Pascual, V. Climent, J. M. Feliu, and M. T. M. Koper, *Interfacial water reorganization as a pH-dependent descriptor of the hydrogen evolution rate on platinum electrodes,* Nature Energy **2**, 17031 (2017).

[4] J. Rossmeisl, K. Chan, R. Ahmed, V. Tripković, and M. E. Björketun, *pH in atomic scale simulations of electrochemical interfaces,* Phys. Chem. Chem. Phys. **15**, 10321 (2013).

[5] S. Kai, W. Chaozhi, and X. Guangzhi, *Surface enhanced Raman spectra of carbonate, hydrocarbonate, and substituted acetic acids on silver hydrosols,* Spectrochimica Acta Part A: Molecular Spectroscopy **45**, 1029 (1989).

[6] C. H. Wang and J. McHale, *Vibrational resonance coupling and the noncoincidence effect of the isotropic and anisotropic Raman spectral components in orientationally anisometric molecular liquids,* The Journal of Chemical Physics **72**, 4039 (1980).

[7] G. D. Mahan and A. A. Lucas, *Collective vibrational modes of adsorbed CO,* The Journal of Chemical Physics **68**, 1344 (1978).

[8] H. Edwards and J. M. Chalmers, *Handbook of Vibrational Spectroscopy*, edited by J. M. Chalmers and P. R. Griffiths (John Wiley & Sons, Ltd, 2006) Chap. Spectra-Structure Correlations in Raman Spectroscopy, pp. 1887 – 1890.

[9] N. Iwasaki, Y. Sasaki, and Y. Nishina, *Ag electrode reaction in NaOH solution studied by in-situ Raman spectroscopy,* Surface Science **198**, 524 (1988).

B

GMPNP Model

B.1. Model details

B.1.1. Simulation domain

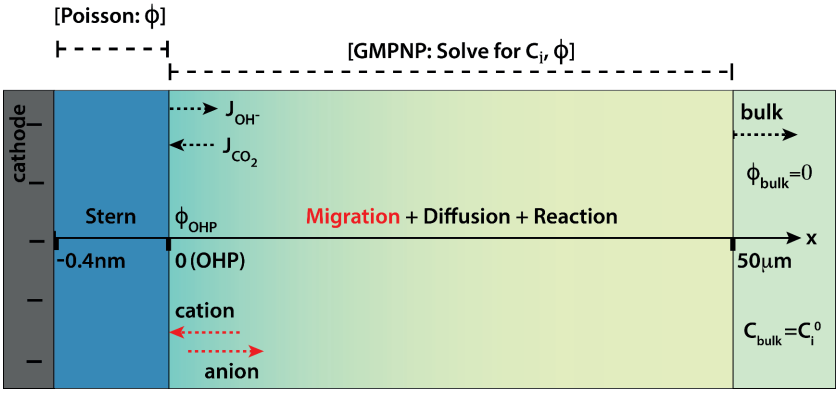

Figure B.1

Parts of this appendix have been published as supplementary information in Energy Environ. Sci. **12**, 3380 (2019) [1].

Research work led by D. Bohra; J. H. Chaudhry provided guidance for the numerical simulations; T. Burdyny and E. A. Pidko played supervisory role; W. A. Smith supervised the project as the principal investigator.

B.1.2. Calculating bulk concentrations

We assume Henry's law to be valid for CO_2 gas and calculate its concentration in water using equation (B.1). We assume the fugacity of CO_2 to be 1 bar.

$$C^0_{CO2,aq} = K^0_H C_{CO2,g} \tag{B.1}$$

where K^0_H is Henry's constant and is given as a function of temperature T by equation (B.2) [2]. The temperature is assumed to be 298.15 K for our calculations.

$$\ln K^0_H = 93.4517 * \left(\frac{100}{T}\right) - 60.2409 + 23.3585 * \ln\left(\frac{T}{100}\right) \tag{B.2}$$

The saturated concentration of CO_2 in an electrolyte ($C_{CO2,aq}$) with 0.1 M $KHCO_3$ is then given by equation (B.3) [3].

$$\log\left(\frac{C^0_{CO2,aq}}{C_{CO2,aq}}\right) = K_S C_S \tag{B.3}$$

where C_S is the molar concentration of the electrolyte (0.1) and K_S is the Sechenov's constant and can be estimated using parameters h_i for species i. Values of h for all species can be found in the Parameters section.

$$K_S = \sum(h_{CO2} + h_{ion}) \tag{B.4}$$

$$h_{CO2} = h^0_{CO2} + h^T_{CO2}(T - 298.15) \tag{B.5}$$

In order to calculate the concentration of solution species in the bulk electrolyte, the Sechenov equation (B.3) is used to estimate the saturated concentration of CO_2 in a 0.1 M $KHCO_3$ electrolyte. The estimated CO_2 concentration is then used to solve the rate equations (B.6) to (B.10) (corresponding to equations (5.6), (5.7) and (5.8) in the chapter 5) till steady state is reached.

$$R_{H^+} = \frac{\partial C_{H^+}}{\partial t} = -k_{w2} C_{H^+} C_{OH^-} + k_{w1} \tag{B.6}$$

$$R_{OH^-} = \frac{\partial C_{OH^-}}{\partial t} = -k_{w2} C_{H^+} C_{OH^-} - k_{a1} C_{OH^-} C_{HCO_3^-} - k_{b1} C_{CO_2} C_{OH^-} + k_{w1} + k_{a2} C_{CO_3^{2-}} + k_{b2} C_{HCO_3^-} \tag{B.7}$$

$$R_{HCO_3^-} = \frac{\partial C_{HCO_3^-}}{\partial t} = - k_{a1} C_{OH^-} C_{HCO_3^-} - k_{b2} C_{HCO_3^-} + k_{a2} C_{CO_3^{2-}} + k_{b1} C_{CO_2} C_{OH^-} \tag{B.8}$$

$$R_{CO_3^{2-}} = \frac{\partial C_{CO_3^{2-}}}{\partial t} = -k_{a2} C_{CO_3^{2-}} + k_{a1} C_{OH^-} C_{HCO_3^-} \tag{B.9}$$

$$R_{CO_2} = \frac{\partial C_{CO_2}}{\partial t} = -k_{b1} C_{CO_2} C_{OH^-} + k_{b2} C_{HCO_3^-} \tag{B.10}$$

The resulting bulk species concentrations for a 0.1 M $KHCO_3$ electrolyte saturated with CO_2 at 1 bar and room temperature are (in mM): $C^0_{CO2} = 34.061$, $C^0_{CO_3^{2-}} = 0.039$, $C^0_{H^+} = 0.00014$, $C^0_{HCO_3^-} = 99.920$, $C^0_{K^+} = 100.0$, $C^0_{OH^-} = 7.1\text{e-}05$, pH = 6.853.

B.1.3. Deviation from equilibrium

Equilibrium constants for the reactions (5.6), (5.7) and (5.8) in chapter 5 are defined as:

$$Keq_w = \frac{k_{w1}}{k_{w2}} \quad and \quad Keq_a = \frac{k_{a1}}{k_{a2}} \quad and \quad Keq_b = \frac{k_{b1}}{k_{b2}}$$

The deviation of the homogeneous reactions from their equilibrium is then defined as:

$$dev_{water-dissociation} = 1 - \frac{[\mathrm{H^+}][\mathrm{OH^-}]}{Keq_w} \tag{B.11}$$

$$dev_{bicarbonate-carbonate} = 1 - \frac{[\mathrm{CO_3}^{2-}]}{[\mathrm{HCO_3}^{-}][\mathrm{OH^-}] Keq_a} \tag{B.12}$$

$$dev_{CO2-bicarbonate} = 1 - \frac{[\mathrm{HCO_3}^{-}]}{[\mathrm{CO_2}][\mathrm{OH^-}] Keq_b} \tag{B.13}$$

B

B.1.4. Limiting H^+ current case

In the limiting H^+ current case, a proton consumption current is added to the overall current such that only <10% of the bulk proton concentration is allowed to be present at the OHP at steady state. The H^+ at the OHP is consumed in the heterogeneous reactions:

$$2\,H^+ + 2\,e^- \rightleftharpoons H_2(g) \tag{B.14}$$

$$CO_2(aq) + 2\,H^+ + 2\,e^- \rightleftharpoons CO(g) + H_2O \tag{B.15}$$

The OH^- and H^+ flux at the OHP (x=0) then becomes:

$$\vec{J}_{OH^-}|_{x=0,t} = -\frac{j_{tot}}{F} \times (1 - j_{H^+frac}) \tag{B.16}$$

$$\vec{J}_{H^+}|_{x=0,t} = \frac{j_{tot}}{F} \times j_{H^+frac} \tag{B.17}$$

where j_{H^+frac} is the fraction of the total current density due to H^+ consumption. The CO_2 flux remains the same as in equation (5.4) in chapter 5.

B.1.5. Scaling the 1D GMPNP equations

We scale the GMPNP equations (5.9), (5.10) and (5.11) in chapter 5 and write them using dimensionless variables as follows:

$$\frac{1}{\Lambda_D}\frac{\partial \tilde{C}_i}{\partial \tau} = \nabla \cdot \left(\nabla \tilde{C}_i + \tilde{C}_i z_i \nabla \Phi + \tilde{C}_i \left(\frac{\sum_{i=1}^{n} \upsilon_i \nabla \tilde{C}_i}{1 - \sum_{i=1}^{n-1} \upsilon_i \tilde{C}_i} \right) \right) + \sum_p \vartheta_{ip} R_i \tag{B.18}$$

$$\nabla \cdot (\varepsilon_r \nabla \Phi) = -q \sum_{i=1}^{n} z_i \tilde{C}_i \tag{B.19}$$

$$L_{debye} = \sqrt{\frac{\varepsilon_0 \varepsilon_r^0 k_B T}{2 e_0^2 C_{elec} N_A}} \tag{B.20}$$

$$\nabla = \frac{\partial}{\partial \tilde{x}}, \Lambda_D = \frac{L_{debye}}{L_n}, \tilde{x} = \frac{x}{L_n}, \tau = \frac{t D_i}{L_{debye} L_n}, \tilde{C}_i = \frac{C_i}{C_i^0},$$

$$\Phi = \frac{\phi F}{RT}, \vartheta_{ip} = \frac{L_n^2}{D_i C_i^0}, \upsilon_i = a_i^3 N_A C_i^0, q = \frac{(FL_n)^2 C_i^0}{\varepsilon_0 RT}$$

where L_n is the system length which is assumed to be 50 μm, L_{debye} is the Debye length as defined by equation (B.20), C_{elec} is the bulk concentration of the electrolyte, e_0 is the fundamental charge of electron and C_i^0 is the bulk concentration of species i. The equations (B.18) and (B.19) are solved simultaneously with the appropriate initial and boundary conditions to obtain the species concentration and potential profiles at steady state.

B.1.6. Scaling the 3D GMPNP equations

Below are the scaled MPNP and Poisson equations corresponding to equations (6.17), (6.18) and (6.20) in chapter 6.

$$\frac{\partial \tilde{C}_i}{\partial \Gamma} = \tilde{\nabla} \cdot \left(\tilde{\nabla} \tilde{C}_i + \tilde{C}_i z_i \tilde{\nabla} \Phi + \tilde{C}_i \left(\frac{\sum_{i=1}^n \upsilon_i \tilde{\nabla} \tilde{C}_i}{1 - \sum_{i=1}^n \upsilon_i \tilde{C}_i} \right) \right) + \sum_j \vartheta_i R_{ij} \quad \text{(B.21)}$$

$$\tilde{\nabla} \cdot \left(\varepsilon_r \tilde{\nabla} \Phi \right) = - \sum_{i=1}^n q_i z_i \tilde{C}_i \quad \text{(B.22)}$$

$$\Lambda = \frac{R}{L}, \tilde{x} = \frac{x}{L}, \tilde{y} = \frac{y}{L}, \tilde{z} = \frac{z}{L}, \Gamma = \frac{t D_i^{eff}}{L^2}, \tilde{C}_i = \frac{C_i}{C_i^0},$$

$$\Phi = \frac{\phi F}{R_G T}, \vartheta_i = \frac{L^2}{D_i^{eff} C_i^0}, \upsilon_i = a_i^3 N_A C_i^0, q_i = \frac{(FL)^2 C_i^0}{\varepsilon_0 R_G T}$$

$$\tilde{\nabla} u = \frac{\partial u}{\partial \tilde{x}} \vec{e_x} + \frac{\partial u}{\partial \tilde{y}} \vec{e_y} + \frac{\partial u}{\partial \tilde{z}} \vec{e_z} \quad \text{(B.23)}$$

$$\tilde{\nabla}^2 u = \frac{\partial^2 u}{\partial \tilde{x}^2} \vec{e_x} + \frac{\partial^2 u}{\partial \tilde{y}^2} \vec{e_y} + \frac{\partial^2 u}{\partial \tilde{z}^2} \vec{e_z} \quad \text{(B.24)}$$

where L is the length and R is the radius of the cylindrical pore with OHP as the outer cylindrical boundary and C_i^0 is the bulk concentration of species i. Scaling all length dimensions with the same constant (L) leads to a simpler computational implementation of the weak form in FEniCS.

Consequently, the equations (B.21) and (B.22) need to be solved simultaneously with the appropriate initial and boundary conditions to obtain the species concentration and potential profiles at steady state.

B

Galerkin form in 3D

In order to solve the GMPNP equations using FEniCS, we need to derive the Galerkin (or the weak form) of the non-linear partial differential equations (B.21) and (B.22). We use an implicit Euler time discretization with the volume element dV defined as $d\tilde{x}d\tilde{y}d\tilde{z}$ and gradient defined for the scaled cartesian coordinates as given in equation (B.23). p_i and s are the the test functions for $\tilde{C}_i$ and Φ in the Galerkin form, respectively. The surface integral term becomes zero in case of a Dirichlet boundary condition or is defined using the surface fluxes as a Neumann boundary condition. In equation (B.26), $\mathbf{n}$ is the outward normal direction to the respective surface.

$$\int_V \left(\frac{\tilde{C}_i^{n+1} - \tilde{C}_i^n}{\Delta\Gamma} \right) p_i dV$$

$$+ \int_V \left[\tilde{\nabla}\tilde{C}_i\tilde{\nabla}p_i + z_i\tilde{C}_i\tilde{\nabla}\Phi\tilde{\nabla}p_i + \tilde{C}_i \left(\frac{\sum_{i=1}^n \upsilon_i \tilde{\nabla}\tilde{C}_i}{1 - \sum_{i=1}^n \upsilon_i \tilde{C}_i} \right) \tilde{\nabla}p_i - p_i\vartheta_i \sum_j R_{ij} \right] dV$$

$$+ \int_{S_1} \mathbf{J}_i^{S_1} p_i dS_1 + \int_{S_2} \mathbf{J}_i^{S_2} p_i dS_2 + \int_{S_3} \mathbf{J}_i^{S_3} p_i dS_3 = 0 \tag{B.25}$$

$$\int_V \left[s \sum_{i=1}^n q_i z_i \tilde{C}_i - \varepsilon_r \tilde{\nabla}\Phi\tilde{\nabla}s \right] dV$$

$$+ \int_{S_1} \frac{\partial\Phi}{\partial n}\varepsilon_r s dS_1 + \int_{S_2} \frac{\partial\Phi}{\partial n}\varepsilon_r s dS_2 + \int_{S_3} \frac{\partial\Phi}{\partial n}\varepsilon_r s dS_3 = 0 \tag{B.26}$$

B.1.7. Reaction-Diffusion and PNP system of equations

Reaction-diffusion model

In the reaction-diffusion model, the flux term in the mass balance equation only contains the diffusion mass transport term and excludes the migration and volume correction terms as given below.

$$\frac{\partial C_i}{\partial t} = -\nabla \cdot \vec{J}_i + \sum_p R_i \tag{B.27}$$

$$\vec{J_i} = -D_i \nabla C_i \tag{B.28}$$

PNP equations

The Poisson-Nernst-Planck (PNP) equations solve the dynamics of the mass transport of solution species including the effects of diffusion, reaction as well as migration such that equations (B.29) and (B.31) are solved simultaneously. However, dilute solution theory is used and the equations are valid for point species.

$$\frac{\partial C_i}{\partial t} = -\nabla \cdot \vec{J_i} + \sum_p R_i \tag{B.29}$$

$$\vec{J_i} = -D_i \nabla C_i - \frac{D_i C_i z_i F}{RT} \nabla \phi \tag{B.30}$$

$$\nabla \cdot (\varepsilon_0 \varepsilon_r \nabla \phi) = -F \sum_{i=1}^{n} z_i C_i \tag{B.31}$$

Equation (5.12) in the chapter 5 is assumed to hold for the relative permittivity (ε_r). For both the reaction-diffusion and PNP systems, R_i are as given in equations (B.6) to (B.10) and the boundary conditions used for the species concentrations are the same as that for the GMPNP system of equations.

B.1.8. SUPG Stabilization of the PNP system

A Streamlined Upwind Petrov-Galerkin (SUPG) stabilization was used for the PNP equations to be able to resolve the steady-state concentration and potential profiles at practically relevant applied voltages for a system of size 50 μm [4–7].

$$\vec{b_i} = -z_i \nabla \Phi \tag{B.32}$$

$$\sigma_{i\iota} = \sigma_{i\iota}^0 \times Pe_{i\iota} \tag{B.33}$$

where

$$\sigma_{i\iota}^0 = \frac{h_\iota}{2|z_i|\|\nabla \Phi\|_2} \tag{B.34}$$

and

$$Pe_{i\iota} = \begin{cases} \frac{h_\iota |z_i| \|\nabla\Phi\|_2}{2} & \text{if } Pe_{i\iota} \leq 1 \\ 1 & \text{if } Pe_{i\iota} > 1 \end{cases} \tag{B.35}$$

$\vec{b_i}$ is the flow field due to migration which is the equivalent dimensionless velocity term in equation (B.29) and (B.30). $\sigma_{i\iota}$ and $Pe_{i\iota}$ are the stability parameter for the SUPG term and the Péclet number for species i for element ι of the mesh, respectively.

The test function of the SUPG stabilization term in the Galerkin form is then given by:

$$\nu_{i\iota}^{SUPG} = \sigma_{i\iota}\vec{b_i}\cdot\nabla v_i = \begin{cases} -\frac{h_\iota^2 z_i}{4}\nabla\Phi\cdot\nabla v_i & \text{if } Pe_{i\iota} \leq 1 \\ -\frac{h_\iota z_i}{2|z_i|\|\nabla\Phi\|_2}\nabla\Phi\cdot\nabla v_i & \text{if } Pe_{i\iota} > 1 \end{cases} \tag{B.36}$$

The SUPG stabilization term in its weak-form for the Nernst Planck equations (NP) is given by multiplying the test function as given by equation (B.36) to the residual of the NP. The overall stabilized NP equation is then given by equation (B.37).

$$\int_\Omega \left(\left(\frac{\tilde{C_i}^{n+1} - \tilde{C_i}^{n}}{\Delta\tau \times \Lambda_D} \right) - \nabla\cdot\left(\nabla\tilde{C_i} + \tilde{C_i} z_i \nabla\Phi\right) - \sum_p \vartheta_{ip} R_i \right) v_i \partial x +$$

$$\sum_{\iota\epsilon I} \int_\iota \left(\left(\frac{\tilde{C_i}^{n+1} - \tilde{C_i}^{n}}{\Delta\tau \times \Lambda_D} \right) - \nabla\cdot\left(\nabla\tilde{C_i} + \tilde{C_i} z_i \nabla\Phi\right) - \sum_p \vartheta_{ip} R_i \right) \nu_{i\iota}^{SUPG} \partial x \tag{B.37}$$

where the first integral term in equation (B.37) is nothing but the residual of the scaled PNP equation multiplied by the test function v_i and integrated over the entire finite element domain Ω. The second term in equation (B.37) is the stabilization term which is a summation of the residual multiplied by the test function for SUPG (equation (B.36)) integrated over each element in the mesh.

The first term in equation (B.37) is integrated by parts to derive the weak form as is common in finite element methods. We drop the higher

order differential terms in the SUPG stabilization (second term in equation (B.37)) since the basis functions used for the finite element solver as piecewise linear. The final form of the stabilized scaled NP equation is given by (B.38).

$$\int_{\Omega}\left(\left(\frac{\tilde{C_i}^{n+1}-\tilde{C_i}^{n}}{\Delta\tau\times\Lambda_D}\right)-\nabla\cdot\left(\nabla\tilde{C_i}+\tilde{C_i}z_i\nabla\Phi\right)-\sum_{p}\vartheta_{ip}R_i\right)v_i\partial x+$$

$$\sum_{\iota\epsilon I}\int_{\iota}\left(\left(\frac{\tilde{C_i}^{n+1}-\tilde{C_i}^{n}}{\Delta\tau\times\Lambda_D}\right)-z_i\nabla\tilde{C_i}\cdot\nabla\Phi-\sum_{p}\vartheta_{ip}R_i\right)\nu_{i\iota}^{SUPG}\partial x \qquad \text{(B.38)}$$

Note that although the Poisson equation is solved simultaneously with the NP equation, it does not feature in the stabilization implemented. Equation (B.38) is simultaneously solved with the Poisson equation with the initial and boundary conditions mentioned in chapter 5.

B.2. Parameters

Potential at the point of zero charge in V vs SHE at pH=7 [8]:

Surface	Value
Ag-pc	-0.70
Ag(111)	-0.450
Ag(110)	-0.735
Ag(100)	-0.616

Rate-constants:

Constant	Value	Units	Reference
kw1	2.4e-2	mol·m-3·s-1	[9–11]
kw2	2.4e+6	mol-1·m3·s-1	[9–11]
ka1	6.0e+6	mol-1·m3·s-1	[12]
ka2	1.07e+6	s-1	[12]
kb1	2.23	mol-1·m3·s-1	[12]
kb2	5.23e-5	s-1	[12]

Diffusion-coefficients in $m^2 \cdot s^{-1}$:

Constant	Value	Reference
D_{H+}	9.311e-9	[9, 10]
D_{OH-}	5.273e-9	[9, 10]
D_{CO2}	1.91e-9	[9, 10]
D_{CO}	2.03e-9	[13]
D_{H2}	4.5e-9	[13]
D_{HCO3-}	1.185e-9	[9, 10]
D_{CO32-}	0.923e-9	[9, 10]
D_{K+}	1.957e-9	[14]
D_{Na+}	1.334e-9	[14]
D_{Li+}	1.029e-9	[14]
D_{Cs+}	2.06e-9	[14]

Solvation sizes in m [15]:

Constant	Value
a_{H+}	0.56e-9
a_{OH-}	0.6e-9
a^{**}_{CO2}	0.23e-9
a^{**}_{CO}	0.113e-9
a^{**}_{H2}	0.074e-9
a^{*}_{HCO3-}	0.8e-9
a_{CO32-}	0.788e-9
a_{K+}	0.662e-9
a_{Na+}	0.716e-9
a_{Li+}	0.764e-9
a_{Cs+}	0.658e-9

* The solvated size of HCO_3^- is assumed to be similar to CO_3^{2-} due to unavailability of a reliable value in literature. ** The solvated size of CO_2, CO and H_2 are assumed based on bond distances without solvation.

Parameters used to estimate Sechenov's constant in $m^3 \cdot kmol^{-1}$ [3]:

Constant	Value
h_{K+}	0.0922
h_{OH-}	0.0839
h_{HCO3-}	0.0967
h_{CO32-}	0.1423
h^0_{CO2}	-0.0172
h^T_{CO2}	-0.000338

Hydration numbers for cations [16, 17]:

Constant	Value
w_{K+}	4
w_{Li+}	5
w_{Na+}	5
w_{Cs+}	3
w_{H+}	10

Henry's constants for gases in water in $mol \cdot kg^{-1} \cdot bar^{-1}$ [18]:

Constant	Value
H_{CO2}	0.034
H_{CO}	0.00095
H_{H2}	0.00078

Other constants

Constant	Value	Units
ρ_e	997	kg·m-3
μ_e	0.89e-3	kg·m-1·s-1
L_c	1.5e-2	m
$\mathbf{v}_e$	0.25e-6	m3·s-1
A_{cross}	1.5e-4	m2
L_{cross}	1.0e-2	m

B

B.3. Supplementary Results: 1D GMPNP model

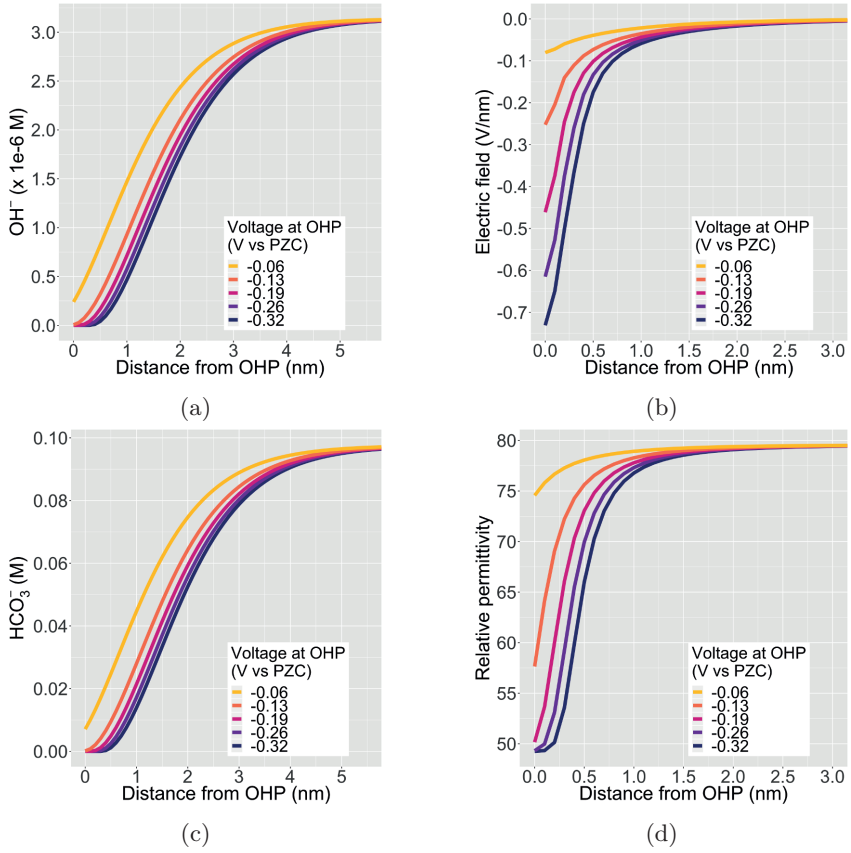

Figure B.2: The electrical double layer (EDL) facing a planar CO_2ER catalyst for a 0.1 M $KHCO_3$ electrolyte solution saturated with CO_2. The above results are derived for a total current density of 1 mA/cm^2 and a CO Faradaic efficiency of 0.8. PZC stands for the potential of point of zero charge of the planar catalyst surface and x=0 is the OHP.

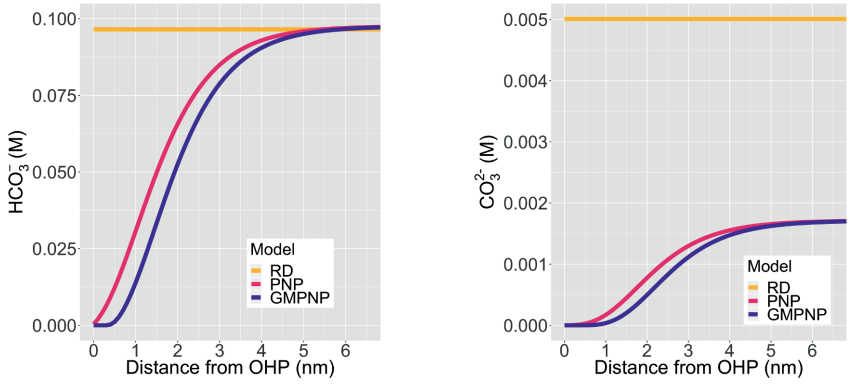

(a) (b)

Figure B.3: Comparison between results obtained from reaction-diffusion (RD) model, a Poisson-Nernst-Planck (PNP) model and a generalized modified PNP (GMPNP) model for the EDL region. x=0 is located at the OHP. All results have been derived for a total current density of 1 mA/cm^2 and a CO Faradaic efficiency of 0.8. The PNP and GMPNP results are for a voltage of -0.32 V vs PZC at the OHP.

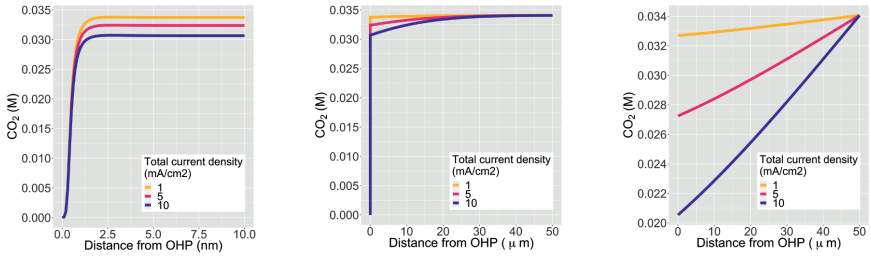

(a) GMPNP: EDL (b) GMPNP: Full domain (c) RD: Full domain

Figure B.4: Influence of total current density on CO_2 concentration derived using the GMPNP model. Figure (a) shows the profiles for a region of 10 nm from the OHP whereas Figure (b) shows the profiles for the entire Nernst layer extending to 50 μm. Figure (c) shows results obtained using reaction-diffusion (RD) model for the purpose of comparison. All results are calculated for a CO Faradaic efficiency of 0.8 and the GMPNP results are for a potential of -0.32 V vs PZC at the OHP.

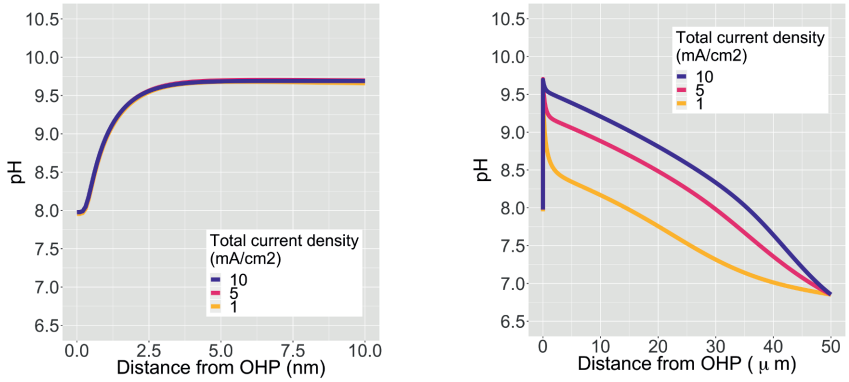

(a) (b)

Figure B.5: Influence of total current density on pH derived using the GMPNP model for the limiting H^+ current case where no more than 10% of the bulk proton concentration is allowed to be present at the OHP (x=0). Figure (a) shows the profiles for a region of 10 nm from the OHP whereas Figure (b) shows the profiles for the entire Nernst layer extending to 50 μm. All results are calculated for a CO Faradaic efficiency of 0.8 and for a potential of -0.32 V vs PZC at the OHP.

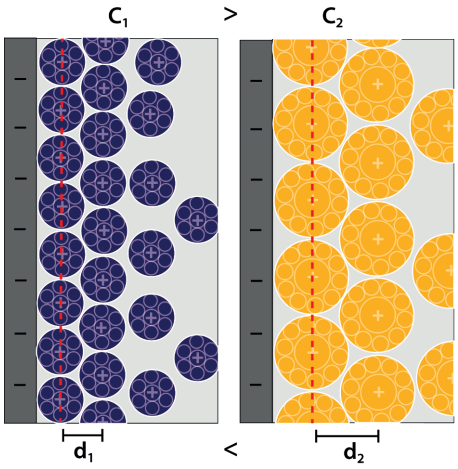

Figure B.6: Illustration of the qualitative difference in the concentrations and potential screening lengths of a small solvated cation vs. a large solvated cation acting as counter-ions in the EDL. The red dashed line represents the OHP. C_i and d_i are concentration at the OHP at the steric limit and the width of the condensed region of the EDL, respectively for cation i.

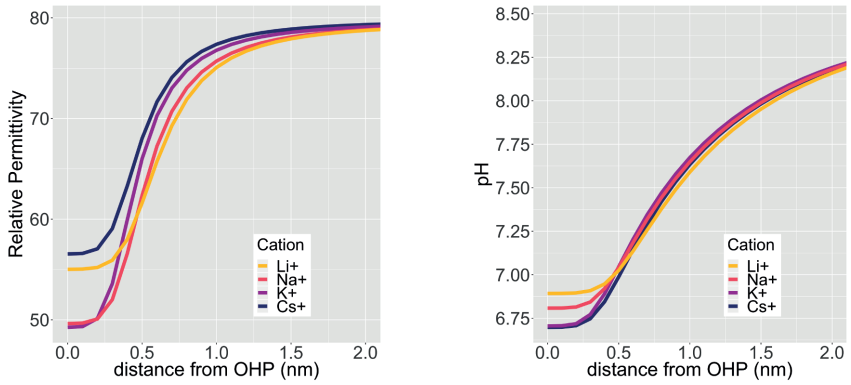

(a) (b)

Figure B.7: Effect of cation size on the relative permittivity and pH of the EDL. Calculations are performed for a potential of -0.32 V vs PZC at the OHP for a total current density of 1 mA/cm^2 and a CO Faradaic efficiency of 0.8.

B.4. Supplementary Results: 3D GMPNP model

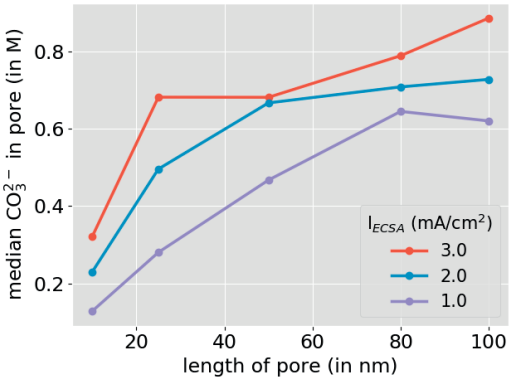

Figure B.8: Influence of changing length (L) of effective catalyst pore on median carbonate ion concentration within the pore. The radius (R) of all pores is 5 nm.

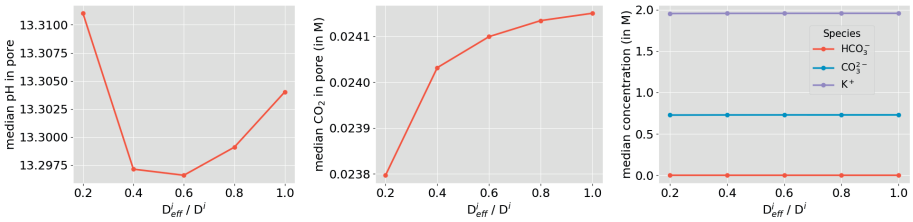

(a) (b) (c)

Figure B.9: Influence of changing the ratio of effective to bulk diffusion coefficient of electrolyte species on their median concentration in pore. A pore of 5 nm x 100 nm (R x L) and I_{ECSA}=2 mA/cm^2 is used for all data points.

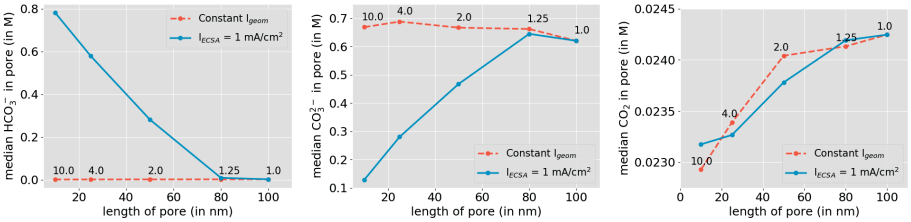

(a) (b) (c)

Figure B.10: A comparison between median species concentrations within pore derived for constant I_{geom} *vs.* constant I_{ECSA}. The annotations on the red dotted curve signify the value of I_{ECSA} corresponding to the respective pore size for the constant I_{geom}. The radius (R) of all pores is 5 nm.

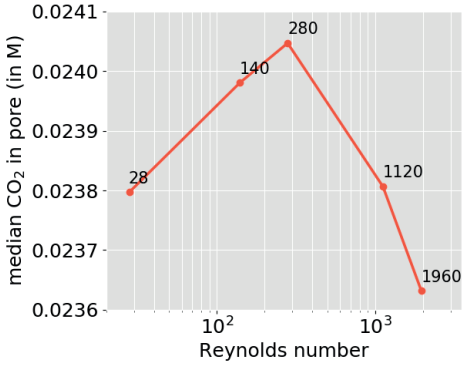

Figure B.11: Effect of changing Reynolds number on CO_2 concentration in the catalyst pore. A pore of 5 nm x 100 nm (R x L) and I_{ECSA}=2 mA/cm^2 is used for all data points.

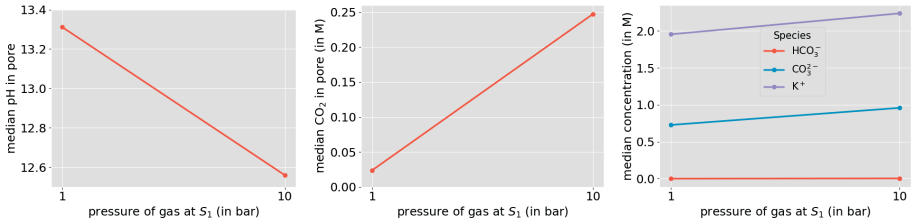

(a) (b) (c)

Figure B.12: Influence of changing the total gas pressure at the gas-electrolyte interface on the median concentration of electrolyte species in the pore. A pore of 5 nm x 100 nm (R x L) and I_{ECSA}=2 mA/cm^2 is used for all data points.

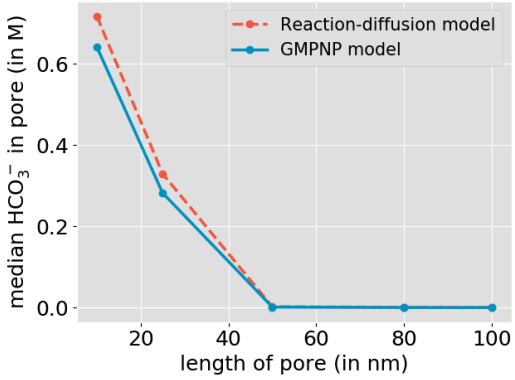

Figure B.13: Comparing the median concentration of HCO_3^- in the catalyst pore with changing pore length (L) derived using a reaction-diffusion model and a GMPNP model. A pore of 5 nm x 100 nm (R x L) and I_{ECSA}=2 mA/cm^2 is used for all data points.

(a) Common scale

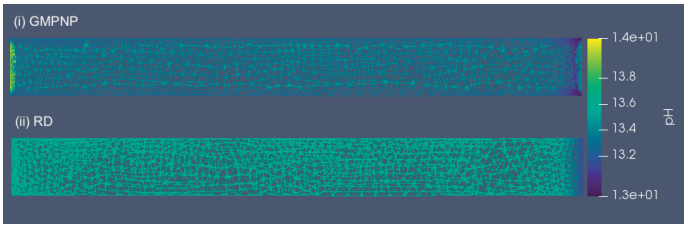

(b) GMPNP

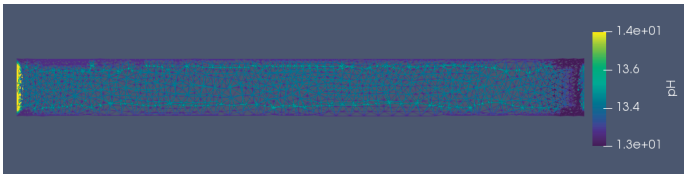

(c) RD

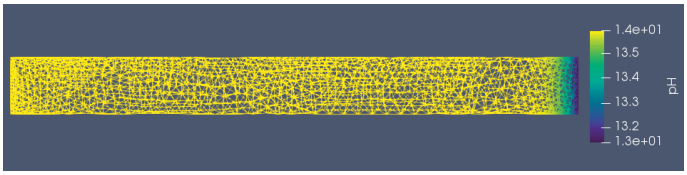

Figure B.14: A comparison of pH along a longitudinal cross-section of a pore with R x L of 5 nm x 100 nm and I_{ECSA}=2 mA/cm^2 for the GMPNP and reaction-diffusion (RD) model. An applied potential of -25 mV vs PZC for the catalyst surface is used for the GMPNP model. The gas-liquid interface is the left edge whereas the electrolyte-electrolyte interface is the right edge with the top and bottom edges being part of the catalyst surface. (a) shows the output of the GMPNP and RD model on the same scale for comparison. (b) and (c) show the distribution on separate scales for clarity.

B

(a) Common scale

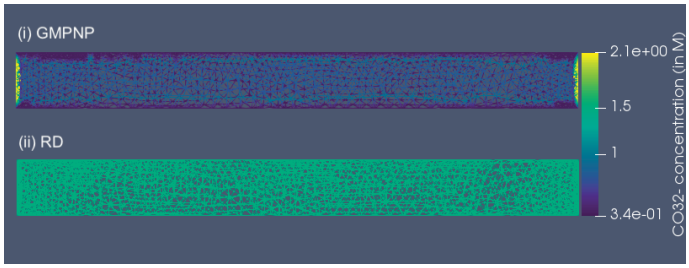

(b) GMPNP

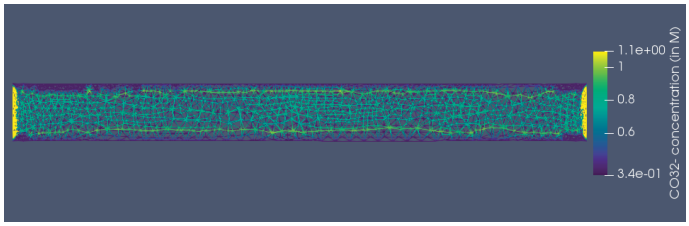

(c) RD

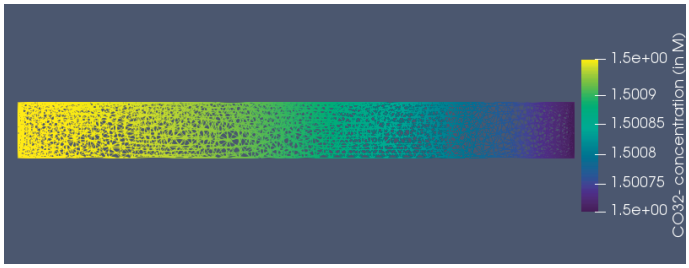

Figure B.15: A comparison of CO_3^{2-} concentration along a longitudinal cross-section of a pore with R x L of 5 nm x 100 nm and I_{ECSA}=2 mA/cm^2 for the GMPNP and reaction-diffusion (RD) model. An applied potential of -25 mV vs PZC for the catalyst surface is used for the GMPNP model. The gas-liquid interface is the left edge whereas the electrolyte-electrolyte interface is the right edge with the top and bottom edges being part of the catalyst surface. (a) shows the output of the GMPNP and RD model on the same scale for comparison. (b) and (c) show the distribution on separate scales for clarity.

(a) Common scale

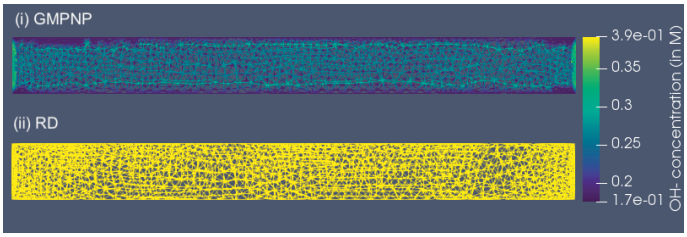

(b) RD

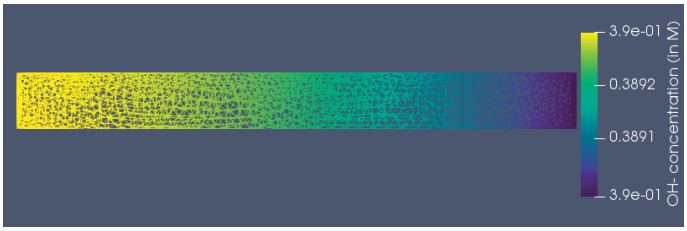

Figure B.16: A comparison of OH^- concentration along a longitudinal cross-section of a pore with R x L of 5 nm x 100 nm and I_{ECSA}=2 mA/cm^2 for the GMPNP and reaction-diffusion (RD) model. An applied potential of -25 mV vs PZC for the catalyst surface is used for the GMPNP model. The gas-liquid interface is the left edge whereas the electrolyte-electrolyte interface is the right edge with the top and bottom edges being part of the catalyst surface. (a) shows the output of the GMPNP and RD model on the same scale for comparison. (b) shows the distribution on a separate scales for the RD model for clarity.

B

(a) CO (aq)

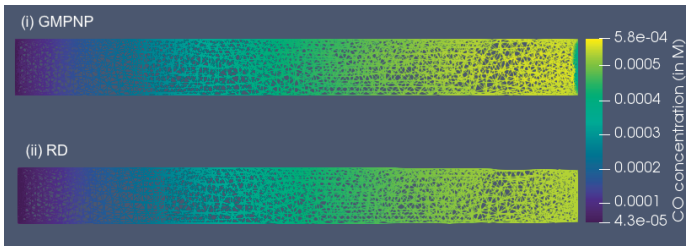

(b) H_2 (aq)

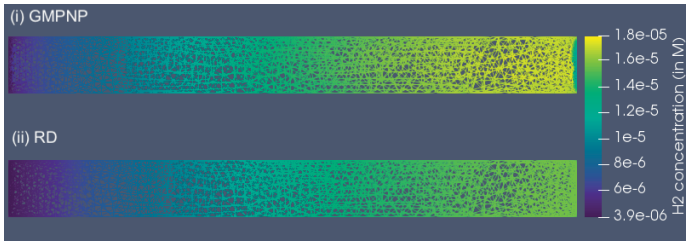

Figure B.17: A comparison of dissolved CO (a) and H_2 (b) concentrations along a longitudinal cross-section of a pore with R x L of 5 nm x 100 nm and I_{ECSA}=2 mA/cm^2 for the GMPNP and reaction-diffusion (RD) model. An applied potential of -25 mV vs PZC for the catalyst surface is used for the GMPNP model. The gas-liquid interface is the left edge whereas the electrolyte-electrolyte interface is the right edge with the top and bottom edges being part of the catalyst surface.

References

[1] D. Bohra, J. H. Chaudhry, T. Burdyny, E. A. Pidko, and W. A. Smith, *Modeling the electrical double layer to understand the reaction environment in a CO_2 electrocatalytic system,* Energy Environ. Sci. **12**, 3380 (2019).

[2] L. Hansson, V. J. Fabry, J.-P. Gattuso, and U. Riebesell, *Guide to best practices for ocean acidification research and data reporting*, Tech. Rep. (Directorate-General for Research and Innovation (European Commission), 2010).

[3] S. Weisenberger and A. Schumpe, *Estimation of gas solubilities in salt solutions at temperatures from 273 K to 363 K,* AIChE Journal **42**, 298 (1996).

[4] J. H. Chaudhry, J. Comer, A. Aksimentiev, and L. N. Olson, *A stabilized finite element method for modified Poisson-Nernst-Planck equations to determine ion flow through a nanopore,* Communications in Computational Physics **15**, 93 (2014).

[5] P. B. Bochev, M. D. Gunzburger, and J. N. Shadid, *Stability of the SUPG finite element method for transient advection-diffusion problems,* Computer Methods in Applied Mechanics and Engineering **193**, 2301 (2004).

[6] T. J. Hughes, L. P. Franca, and G. M. Hulbert, *A new finite element formulation for computational fluid dynamics: VIII. The galerkin/least-squares method for advective-diffusive equations,* Computer Methods in Applied Mechanics and Engineering **73**, 173 (1989).

[7] L. P. Franca, S. L. Frey, and T. J. Hughes, *Stabilized finite element methods: I. Application to the advective-diffusive model,* Computer Methods in Applied Mechanics and Engineering **95**, 253 (1992).

[8] S. Trasatti and E. Lust, *The potential of zero charge,* in *Modern Aspects of Electrochemistry*, edited by R. E. White, J. O. Bockris, and B. E. Conway (Springer US, Boston, MA, 1999) pp. 1–215.

[9] M. R. Singh, J. D. Goodpaster, A. Z. Weber, M. Head-Gordon, and A. T. Bell, *Mechanistic insights into electrochemical reduction of CO_2*

over Ag using density functional theory and transport models, Proceedings of the National Academy of Sciences **114**, E8812 (2017).

[10] M. R. Singh, E. L. Clark, and A. T. Bell, *Effects of electrolyte, catalyst, and membrane composition and operating conditions on the performance of solar-driven electrochemical reduction of carbon dioxide,* Phys. Chem. Chem. Phys. **17**, 18924 (2015).

[11] P. Atkins, J. de Paula, and J. Keeler, *Atkins' Physical Chemistry*, 11th ed. (Oxford University Press, 2017).

[12] T. Burdyny, P. J. Graham, Y. Pang, C.-T. Dinh, M. Liu, E. H. Sargent, and D. Sinton, *Nanomorphology-enhanced gas-evolution intensifies CO_2 reduction electrochemistry,* ACS Sustainable Chemistry & Engineering **5**, 4031 (2017).

[13] E. L. Cussler, in *Diffusion: Mass Transfer in Fluid Systems (2nd ed.)* (New York: Cambridge University Press., 1997).

[14] J. Rumble, ed., *CRC Handbook of Chemistry and Physics*, 100th ed. (CRC Press, 2019).

[15] E. R. Nightingale, *Phenomenological theory of ion solvation. Effective radii of hydrated ions,* The Journal of Physical Chemistry **63**, 1381 (1959).

[16] J. O. Bockris and A. K. Reddy, *Volume 1: Modern Electrochemistry*, 2nd ed. (Springer US, 1998).

[17] J. O. Bockris and P. P. S. Saluja, *Ionic solvation numbers from compressibilities and ionic vibration potentials measurements,* The Journal of Physical Chemistry **76**, 2140 (1972).

[18] R. Sander, *Compilation of henry's law constants (version 4.0) for water as solvent,* Atmospheric Chemistry and Physics **15**, 4399 (2015).

Acknowledgements

Thanks, Wilson, for giving me the opportunity to do this PhD, and for your relentless trust and support. You were not simply a supervisor, but also a role model, an ally and a friend. I could not ask for a more empowering, inclusive and exciting environment to do science. I will miss every bit of the fun we have had over the years. Thanks, Evgeny, for always being so open to discuss science (and everything else) and including me as a part of your group. Your kind support made my PhD journey richer. Thanks, Zeb for being so open to collaborating with someone so far away (geographically and scientifically). Thanks for patiently teaching me so many concepts in numerical analysis and for your enthusiasm to learn about the hairy concepts in CO_2 electrocatalysis. I am really glad I cold-emailed you and the experience has encouraged me to always reach out to people and be a curious scientist. Thanks, Tom, for always being there to discuss science, life, and for sincerely helping out each time I needed it. You are the most reliable person I have ever known professionally.

Thanks, Paulien, for your mentorship, support, and for being so approachable. I learned a lot from our chats, and you helped me tremendously in connecting with people and building my confidence. Thanks, Hans, Bernard and Andreas for your guidance. Thanks, Guanna and Isis, for being my very first scientific collaborators, for guiding me, and for your company. Thanks, Jan Rossmeisel and Alexander Bagger at the University of Copenhagen, for your warm welcome and for getting me started with computational electrocatalysis. Thanks, Bartek, Digda and Ming, for all the great time. A part of me came back to MECS just to have fun with you guys. Thanks, Steffen, for being such a great office-mate and friend. I still miss our chitter-chatter about how the world is falling apart. Thanks, Nate, for making Rotterdam so much more fun. I am still counting on you to move back. Thanks, Sanjana and Elena, for getting on-board the double-layer train and taking the research forward with so much enthusiasm. Thanks, Marijn, for translating the summary of this thesis to Dutch. Thanks, Sanjana, Kai, Kailun, Recep, Mark, Marijn, Nienke, Anirudh, Ali, Elena, Bob, Robert, Annika, Chuncheng, Evgeny

Jr. and Dapeng for being such fantastic team-mates. I thoroughly enjoyed all our meetings, conference trips, coffee chats, lunches and parties (yes, I just said meetings in the same breath as parties). Thanks, Fahimeh, for your kindness, warmth, and for comforting me in moments of chaos. Thanks, Robin, Audrey and Diana, for sharing the office and hearing out so many whines and protests. Thanks, Georgy, for the countless 7 pm heart-to-hearts. I will always be proud to have breached the 30% air time with you. Thanks, Divya Tak, for making the most stunning and adorable cover art for my first publication and helping me troubleshoot the thesis cover. Thanks, all of ISE and MECS group members, for being so welcoming and warm. Thanks to NWO and SURFsara for providing the resources for this research work.

Thanks, Mumma, Papa and Tanmay, for your unconditional love, support and encouragement. You taught me courage and empathy, and they carry me through everything. Thanks, Mandar, for pushing me to pursue things that make me smile more, and for being there every step of the way.

Curriculum Vitæ

Divya Bohra was born on the 4^{th} of January 1990 in Ratlam, India. She completed her bachelors degree with honours in chemical engineering at the Indian Institute of Technology, Kharagpur in 2011. She then moved to the Netherlands to pursue a masters degree in chemical engineering at the Delft University of Technology. Her masters thesis was on the topic of photoelectrochemical water splitting and she completed her MSc in 2013 with a cum laude. Divya worked as a process technologist for Shell Chemicals in the Netherlands before starting her PhD project in the Materials for Energy Conversion and Storage group at Delft University of Technology in 2016. The results of her doctoral research are presented in this thesis.

List of Publications

8. N. T. Nesbitt, T. Burdyny, H. Simonson, D. Salvatore, **D. Bohra**, R. Kas, W. A. Smith, *Liquid-Solid Boundaries Dominate Activity of CO_2 Reduction on Gas-Diffusion Electrodes*, ACS Catalysis **10**, XXX, (2020).

7. **D. Bohra**, J. H. Chaudhry, T. Burdyny, E. A. Pidko, W. A. Smith, *Mass Transport in Catalytic Pores of GDE-Based CO_2 Electroreduction Systems*, ChemRxiv, (2020), In peer review.

6. R. Kas, K. Yang, **D. Bohra**, R. Kortlever, T. Burdyny, W. A. Smith, *Electrochemical CO_2 reduction on nanostructured metal electrodes: fact or defect?*, Chemical Science **11**, 17 (2020).

5. **D. Bohra**, J. H. Chaudhry, T. Burdyny, E. A. Pidko, W. A. Smith, *Modeling the electrical double layer to understand the reaction environment in a CO_2 electrocatalytic system*, Energy & Environmental Science **12**, 11 (2019).

4. M. Valenti, N. P. Prasad, R. Kas, **D. Bohra**, M. Ma, V. Balasubramanian, L. Chu, S. Gimenez, J. Bisquert, B. Dam, W. A. Smith, *Suppressing H_2 Evolution and Promoting Selective CO_2 Electroreduction to CO at Low Overpotentials by Alloying Au with Pd*, ACS Catalysis **9**, 4 (2019).

3. **D. Bohra**, I. Ledezma-Yanez, G. Li, W. de Jong, E. A. Pidko, W. A. Smith, *Lateral Adsorbate Interactions Inhibit $HCOO^-$ while Promoting CO Selectivity for CO_2 Electrocatalysis on Silver*, Angewandte Chemie **131**, 5 (2019).

2. N. J. Firet, M. A. Blommaert, T. Burdyny, A. Venugopal, **D. Bohra**, A. Longo, W. A. Smith, *Operando EXAFS study reveals presence of oxygen in oxide-derived silver catalysts for electrochemical CO_2 reduction*, Journal of Materials Chemistry A **7**, 6 (2019).

1. **D. Bohra**, W. A. Smith, *Improved charge separation via Fe-doping of copper tungstate photoanodes*, Physical Chemistry Chemical Physics **17**, 15 (2015).